QUARTERLY REPORT of RTRI

Nov. 2022 Vol. 63 No. 4

CONTENTS

RAILWAY TECHNICAL RESEARCH INSTITUTE

CONTENTS

Recent Activities in Railway Vehicle Technology Research and Development

Takamitsu YAMAMOTO

Vehicle Technology Division

Spurred by fall in passenger numbers following the COVID-19 pandemic, railways today have made rapid progress in improving operational efficiency and labor saving measures. DX (digital transformation) technology, which has been applied to automatic train operation, inter alia, is therefore attracting attention. Another focal point for railways is the realization of global decarbonization, illustrated by "2050 Carbon Neutral" goal declared by the Suga Cabinet and "COP26." This paper introduces the outlines of three technologies related to these topics, namely, a "Method for evaluating wheel slide protection (WSP) performance by hybrid simulator," a "Method applying neural networks to detect abnormal noise during train operation," and "High efficiency of diesel electric railcars."

1. Introduction

Since FY2020, the Railway Technical Research Institute (RTRI) has been working on the 'Research and Development for Creating the Future of Railways: RESEARCH 2025,' which is a medium-term management plan that serves as a 5-year basic roadmap setting out the policies for research and development as follows: (1) improvement of safety, especially resilience to natural disasters; (2) innovation of railway systems applying digital technology; and (3) creation of high-quality results that demonstrate comprehensive strength. Furthermore, the goals of the research and development are to improve safety, reduce costs, be in harmony with the environment, and improve convenience.

Decreasing passenger numbers due to COVID-19 has resulted in rapid progress in the railways in improving the efficiency of operations and labor saving measures, and the automatic operation of trains has become very topical. As such, there is increased focus on technologies which drive the digital transformation (DX) of railways. Another topical issue is achieving global decarbonization, in response to the "2050 Carbon Neutrality" goal announced by the Suga Cabinet and "COP26" which require the reduction of greenhouse gas emissions.

This report offers an overview of three technologies related to these topics, namely, a "Method for evaluating wheel slide protection performance by hybrid simulator," a "Method applying neural networks to detect abnormal noise during train operation," and "High efficiency of electric diesel vehicles."

2. Method for evaluating wheel slide protection performance by hybrid simulator

2.1 Issues in evaluation of wheel slide protection performance

In current railway vehicle tests, wheel slide protection (WSP) performance is generally evaluated by sprinkling water from the vehicle toward the contact surface between the wheels and rails in order to intentionally create low-adhesion conditions and cause wheels to slide. However, there are many influencing factors relating to the extent of sliding (e.g., sprinkled water amount, position, temperature, wheel / rail surface conditions), and it is extremely difficult to reproduce test conditions exactly. Furthermore, although evaluating the performance of actual railway vehicles in tests is essential for ensuring safety, it is time and labor intensive, creating a need for a method which allows performance to be checked with a limited number of tests.

2.2 Overview of hybrid simulator for wheel slide protection

We therefore developed a hybrid simulator for evaluating WSP (Fig. 1) as a bench test environment that efficiently reproduces the responsiveness of the air brake on the actual machine by simulating the parts related to these influencing factors with a computer [1]. Figure 2 shows the function of the actual machine and computer. The actual machine is a part that reproduces the flow of compressed air of a current railway vehicle; and it is composed of the same air-controlled brake equipment as an actual railway vehicle, from the air tank to the constant-volume container that simulates the brake cylinder (BC). Responsiveness can be changed by setting a variable length of the air pipe that connects the devices. The air brake equipment was equipped with four independent axles (i.e., one railway vehicle). The computer then simulates elements other than the actual machine. It comprises a real-time computer, operating PC, and BC pressure sensor. The tester can arbitrarily set the railway vehicle model, WSP algorithm, and adhesion conditions (slipperiness) between the wheels and rails inside the real-time computer. The braking force that considers the specifications of the basic braking device is calculated based on the measured BC pressure sensor value, and this value is input into the railway vehicle model. In the railway vehicle model, the deceleration motion is calculated based on the input braking force and the assumed railway vehicle specifications. The calculation of the deceleration motion reflects the preset adhesion conditions and WSP algorithm. For example, when the axis that is decelerating inside the computer satisfies the WSP detection conditions that are set by the WSP algorithm, then an operation command is immediately output WSP to the sliding control valve of the actual machine corresponding to that axis, and the BC pressure is exhausted. The change in BC pressure is reflected in the next calculation step, and the deceleration motion is calculated again. This process is repeated until the railway vehicle stops. The developed simulator is characteristic in that the tester can arbitrarily set low-adhesion conditions and easily conduct a large number of tests. This enables evaluations using statistical analysis, due to the ease of obtaining large numbers of test results, and thus makes it
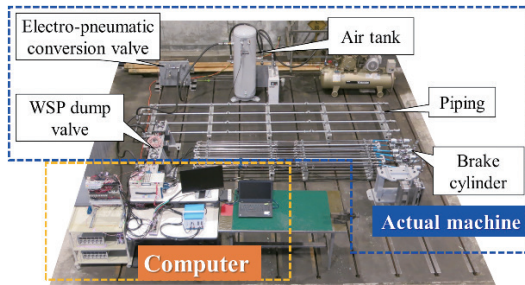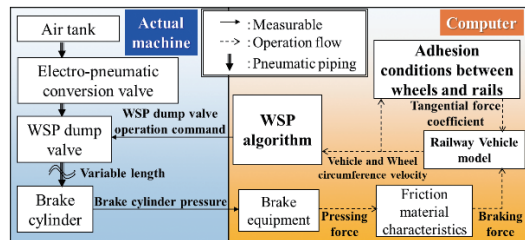
Fig. 1   Hybrid simulator for WSP

Fig. 2   Functions of actual machine and computer

possible to evaluate the influence of individual specific test elements by fixing the conditions. This is expected to be used as a tool for developing a new WSP algorithm as well as a method for reducing the number of vehicles used in current railway vehicle testing, by comparing and verifying the WSP algorithm before actual railway vehicle test.

3. Method applying neural networks to detect abnormal noise during train operation

3.1 Overview of abnormal noise detection method

Trains are not equipped with sensors for the purpose of detecting abnormal noise while in operation, and the current situation is such that abnormal noise detection relies on the ears of train crews. However, if unmanned operations become widespread in the future, it will be necessary to detect abnormal noise with a microphone as an alternative to human detection of such sounds. Various possible approaches can be considered for methods to detect abnormal noise from the results of noise collection inside and outside the train, and the appropriateness of the method should be investigated based on the definition of abnormal noise to be perceived. If the abnormal noise that is assumed as the perceived object is clearly different from normal operating noises, then it may be possible to distinguish between normal and abnormal situations by advanced analysis of only the noise information. However, cases where it is difficult to distinguish the target noise from the running noise when passing through a rail joint or a turnout just by listening to this noise, can only be judged normal or not by knowing whether it is caused by the passage over this type of section or a noise of interest due to another cause. In such cases, the analysis requires at least the running position information in addition to the noise. Similarly, there is a possibility that the judgment of normal / abnormal noise collection results depends not only on the running position of the train but also the speed, notch, and other equipment operating conditions (henceforth, collectively referred to as "railway vehicle state quantity"), and there is a need for an analysis that takes this information into ac-

count. When constructing an abnormal noise detection method that takes the railway vehicle state quantity into account, it is effective to construct a method for predicting what kind of noise is produced in normal circumstances according to the railway vehicle state quantity (i.e., normal noise). Therefore, in this research, we proposed a method for predicting running noise according to the railway vehicle state quantity based on a neural network, with the objective of contributing to future abnormal train noise detection methods [2].

3.2 Prediction method using neural network

Figure 3 shows the structure of the neural network that was used in this method. The structure of the network is such that the inputs are running position $x(t)$, velocity $v(t)$, powering notch $P\_n(t)$, brake notch $N\_n(t)$, and compressor ON-OFF information $CP(t)$ at an arbitrary time; and the noise pressure component $P\_(f\_c)$ (t) of each frequency is predicted. There are two hidden layers between the input layer and output layer, each with 20,200 nodes. The neural network has a structure such that the information in the previous layer is multiplied by a weight and aggregated, which is then given as an input to some activation function that is determined by the user, and this output result is passed on to the next layer. Figure 4 shows how each node in hidden layer 1 outputs an activation function. In this figure, X^1_i and Y^1_i are the input and output values of node i in hidden layer 1, and $h(\ )$ is the activation function. For $h(\ )$, we used the sigmoid function (Eq. (1)), which is often used in neural networks. In this paper, the output at node i of the hidden layer 2 is defined by (2). Figure 5 shows the activation function of the hidden layer 2 according to (2).

$$h(X^1_i) = \frac{1}{1 + e^{-X^1_i}} \tag{1}$$

$$Y^2_i = \begin{cases} X^2_i \sin\left\{\left(\dfrac{i-1}{2}\right)\dfrac{\pi}{L}x(t)\right\} & i \text{ is odd} \\[3mm] X^2_i \cos\left\{\left(\dfrac{i-2}{2}\right)\dfrac{\pi}{L}x(t)\right\} & i \text{ is even} \end{cases} \tag{2}$$
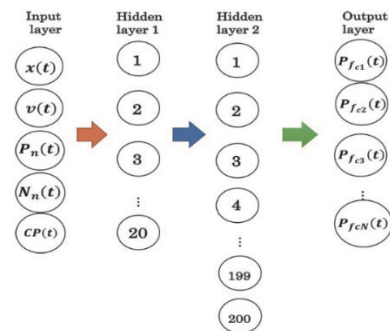

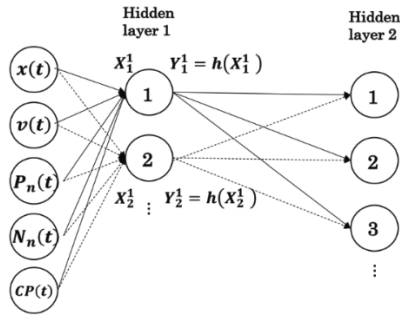**Fig. 3   Structure of neural network**

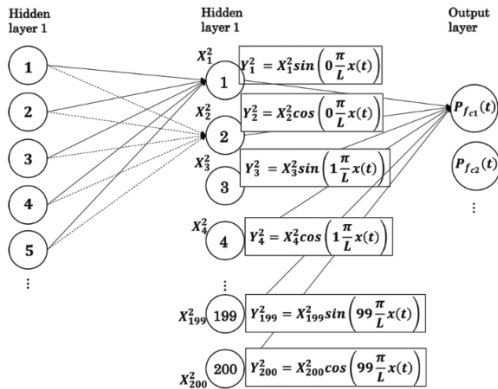**Fig. 4 Activation function of hidden layer 1**

Fig. 5 Activation function of hidden layer 2

3.3 Example of running noise learning results

After acquiring the training data, the input / output relationship was trained using the neural network that was described in the previous section. This neural network was given the inputs of running notch, velocity, running position, and compressor operating status. The predicted values of each frequency component were obtained as outputs. Figure 6 shows the example of comparison result between the predicted value and measured value. The predicted waveform is a good representation of the tendency of the measured waveform. However, there are some places where the error is relatively large. In this research, we used a method that can predict normal running noise, and we assume a system that defines cases where this prediction result deviates significantly from the measurement result as an abnormal noise. As basic research toward this end, we devised a neural network that can predict the normal running noise according to the notch, velocity, running position, and other necessary equipment operating conditions of the railway vehicle.
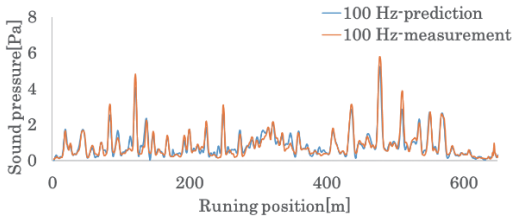
Fig. 6 Example of comparison predicted and measured values

4. High efficiency of electric diesel vehicles

4.1 Current status of power generation system for electric diesel vehicles

Diesel railcars traveling in non-electrified sections have often used hydraulic railcars using a hydraulic transmission. However, in recent years, similar to electric diesel locomotives, there has been an increase in the number of electric trains adopted that run on power generated by the main generator as well as hybrid vehicles that can regenerate electric power by having a battery installed. One factor behind such trends is that electric type vehicles have fewer mechanical parts (e.g., propulsion shafts, transmission) than hydraulic types and thus have the following advantages:

· Few rotating parts and high level of safety
· Reduced maintenance and many common maintenance methods between trains
· Hybridization enabling power regeneration

Meanwhile, electric type vehicles have a system in which electric devices are connected in series, so the following issues arise:

· Low power transmission efficiency
· High initial cost
· Heavy weight

The reduction of energy consumption has become more important in recent years, and it has become more important than ever before to improve power transmission efficiency and reduce fuel consumption, so improving the above issues is important.

The current power generation system includes the following two system types: (a) system that combines a brushless synchronous generator and a full-wave rectifier, and (b) system that combines an alternating current generator (induction generator (IG) or permanent magnet synchronous generator (PMSG) and PWM converter) (Fig. 7). Each of these systems consists of a combination of a generator and rectifier.
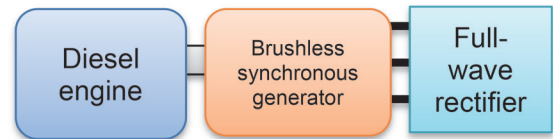
(a) Brushless synchronous generator
  + Full-wave rectifier
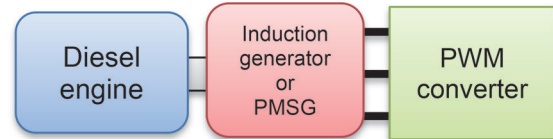
(b) AC generator (IG or PMSG)
  +PWM converter

Fig. 7 Current power generation system for electric diesel vehicles

4.2 Power generation system using PMSG and full-wave rectifier

Of the generators used in these systems, PMSG has a relatively high efficiency and simple structure because the rotor has no energized part, and there is no need for external excitation since power can be generated by the magnetic flux of a permanent magnet. Fur-

thermore, unlike the PWM converter, the full-wave rectifier does not require a switchable power device or control device, so it is low-cost, compact, and lightweight. Therefore, combining the PMSG and full-wave rectifier enables the realization of a high-efficiency, low-cost, compact, and lightweight power generation system. However, even if simply combining PMSG and a full-wave rectifier, operating this with a sufficient voltage and current is difficult with the magnetic flux that is generated by a permanent magnet, and it is difficult to construct a small high-power generation system such as that used in railway vehicles. Therefore, we devised a system with improved output characteristics by adding a capacitor to the circuit, and we evaluated the characteristics using a simulation. Methods for inserting the capacitor that can be considered are the method of connecting in parallel as shown in Fig. 8(a), and the method of connecting in series as shown in Fig. 8(b).

(a) Parallel connection capacitor

(b) Series connection capacitor
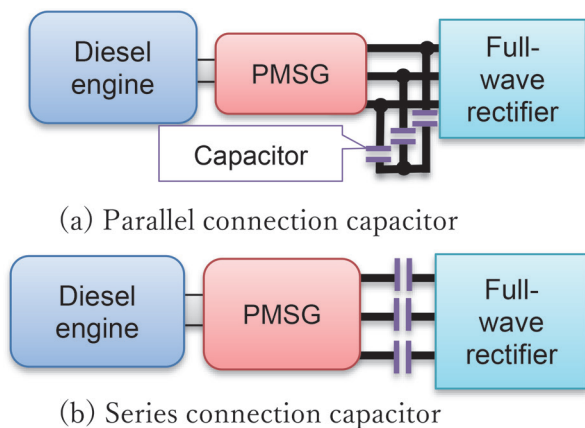
Fig. 8 Power generation system using PMSG and full-wave rectifier

4.2.1 Power generation system using parallel connection capacitor [3]

When the capacitor is designed so that the PMSG inductance and the capacitor resonate at the operating rotation speed connected in parallel, then the power generation system operates as a direct current source that supplies a constant current regardless of the voltage on the direct current side. Furthermore, this operates at a voltage that greatly exceeds the voltage that is generated by a permanent magnet, which enables higher output. This system is suitable for use in a hybrid system that can absorb the difference between the generated power and load power because the power generation output is fixed when combined with a DC power supply with constant voltage.

4.2.2 Power generation system using series connected capacitor [4]

By designing the capacitor so that resonance occurs when con-nected in series, then the power generation system operates as a DC voltage source that maintains constant current regardless of the load current on the DC side. Even in this circuit, this operates at a voltage that greatly exceeds the voltage of a permanent magnet, which enables higher output.

This system can be used as a power generation system for electric diesel vehicles since this system operates as a DC voltage source that is similar to an overhead wire system. Hybridization cases require the prevention of the voltage sources from being directly connected to each other (e.g., by arranging a power converter between the battery and power generation system).

The basic operation of these power generation systems has been verified by simulation, and all these systems are thought to be promising for railway vehicles. In the future, we would like to conduct prototype tests and move toward practical use.

5. Conclusion

In this report, we introduced an overview on the following three topics from recent research and development relating to railway vehicle technology: Evaluation method of slide protection performance by hybrid simulator as a technology related to reducing labor by applying DX, Method applying neural networks to detect abnormal noise during train operation, and High efficiency of electric diesel vehicles as a technology related to decarbonization. These technologies are essential for the sustainable development of railways in the future, and thus this research is considered to be of the highest priority.

References

[1] Daisuke Hijikata: "A Hybrid Simulator for Wheel Slide Protection Combining Pneumatic Brake Hardware and a Real-time Computer," *J-rail*, 2021 (in Japanese).
[2] Gaku Yoshikawa: "A study of the prediction method of train traveling tone based on neural network," Institute of Electrical Engineers of Japan Study Group, TER-21-049, pp. 33-38, 2021 (in Japanese).
[3] Minoru Kondo: "Comparison of Two Types of DC Power Generation System with Permanent Magnet Synchronous Machines and Full-Bridge Rectifiers Using Resonant Circuits," *IEEJ Journal of Industry Applications*, Vol. 141, No. 5, pp. 416-422, 2021.
[4] Minoru Kondo: "DC Power Generation Systems with Permanent Magnet Synchronous Machines and Full-Bridge Rectifiers Using Resonant Circuits," Institute of Electrical Engineers of Japan Study Group, RM-21-045, 2021 (in Japanese).

Author

Takamitsu YAMAMOTO
Deputy Director, Vehicle Technology Division
Research Areas: Main Circuit, Hybrid Railway Vehicle, Fuel Cells, and Secondary Batteries

Track Technology for Reducing Maintenance Cost and Labor

Yoshitsugu MOMOYA
Track Technology Division

From the viewpoint of safe train operation, railway tracks must be kept in a satisfactory condition by appropriate track inspection and maintenance activities. On the other hand, from the viewpoint of good management, it is necessary to develop track technologies for cost reduction of both track inspection and maintenance. In the development of these technologies, research needs to focus on automation and labor-saving advances by applying ICT and AI techniques, which have progressed significantly in recent years. This paper describes RTRI's recent R&D for these track technologies.

Key words: track structure, maintenance, track improvement, image processing, machine learning

1. Introduction

Tracks, which are railway facilities which extend over large distances, deteriorate due to the repeated passage of trains, while their maintenance and management are cost and labor intensive. At the same time, it is becoming increasingly difficult to recruit railway workers due to the declining birthrate and aging population in Japan which is shrinking the working population. Therefore, there is an extremely high demand for methods which can save labor, personnel, and maintenance costs in track inspection and maintenance work.

These demands are not particularly new, and work has already been done to reduce inspection and maintenance costs by strengthening track structures and developing and introducing slab track and other types of ballastless track. However, an issue with such measures is large initial cost. As such, there is ongoing development of new structures and construction methods that can suppress the introduction cost of these tangible measures.

Meanwhile, there is ongoing research and development with the aim of saving on labor through intangible measures, such as utilizing existing data or developing and introducing systems which can acquire and analyze new data. The recent development of information processing technology based on concepts such as ICT or AI has enabled the processing of large amounts of information in a short period of time, resulting in progress in automation such as equipment status diagnosis and maintenance plan formulation. Increased accuracy of diagnosis by scientific analysis of such data enables the optimization of the frequency and quantity of inspections and maintenance as well as the reductions in maintenance costs by reviewing the control values of deterioration indicators in addition to the frequency and cycle of inspections.

Furthermore, labor can be reduced by cutting down on equipment and machine inventories in addition to the tangible and intangible measures described above. This is because labor and maintenance costs are generally incurred for inspection, maintenance, and management of equipment and machines, and these costs will depend on the number of pieces of equipment or machines a company owns. Therefore, costs may be effectively reduced if this inventory of hardware is optimized in the light of what is needed to satisfy operating conditions such as vehicle and operating conditions. However, to streamline the amount of equipment and number of machines owned by a company, it is important to take into account track design and analysis of data on accumulated track conditions and maintenance results, and specific measures need to be investigated while considering the various issues that accompany the slimming down of equipment and machines.

Below, we introduce recent research trends and examples of RTRI work on track technologies that are related to streamlining maintenance costs and labor.

2. Maintenance costs / labor reduction of track structure

2.1 Optimizing scale of equipment / machines

2.1.1 Expansion of sleeper spacing [1]

Ballasted tracks on local lines that are mainly composed of wooden sleepers may have rails that are insufficiently fastened due to the decay of the wooden sleepers, resulting in derailment caused by gauge widening. Therefore, railway operators managing the number of defective wooden sleepers as well as individual status, with a focus on curved sections, but the labor requirements of visually inspecting a large number of sleepers is a heavy burden on railway operators.

Meanwhile, measures are being taken in order to prevent derailment caused by gauge widening by replacing wooden sleepers with PC sleepers. With the reduction of the weight of vehicles and the reduction of running sections of freight trains in recent years, the operating conditions of tracks have been changed. As a result, the train load acting on tracks is often smaller than before. Therefore, expanding the sleeper spacing alongside replacing wooden sleepers with PC sleepers can be implemented to reduce the number of sleepers subject to management. Therefore, we developed the following method for expanding spacings that considers service conditions.

We conducted a full-scale loading test in order to evaluate the effects of sleeper spacings and trackbed conditions on track settlement, and we proposed the limits of ballast track applications and coefficients used in the track settlement equation. We also proposed an equation to estimate lateral resistance of the trackbed that considers the group pile effect at arbitrary sleeper spacings, and we confirmed its validity through a verification test (Fig. 1). Furthermore, we proposed a calculation method that corresponds to the service conditions and applicable values for the coefficient of variation used for performance verification of the rail fastening systems. A limit sleeper interval that can ensure running safety was then shown for each curve radius.

Regarding the expansion of sleeper spacings based on the above idea, test laying has started on commercial lines, and in the future, we plan to expand the scope of application while monitoring
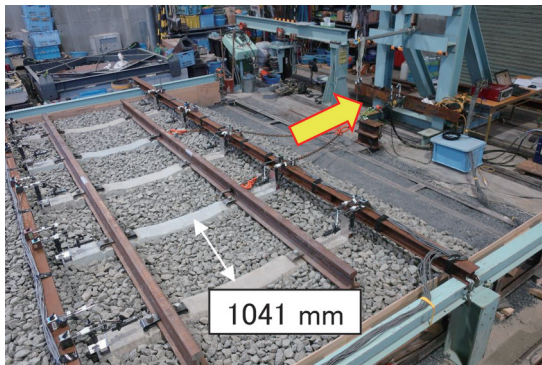
Fig. 1 Accuracy verification test of trackbed lateral resistance estimation equation using full-scale track

Fig. 2 Example of investigation on the number of owned MTTs

track conditions after laying.

2.1.2 Optimization of the number of maintenance machines owned [2]

Multiple tie tampers (MTTs), rail grinding machines, and ballast renewal machines that are used for track maintenance are generally expensive, so it is difficult to install large number of those machines. Meanwhile, maintenance costs such as inspection and replacement of consumables are needed in addition to renewal costs for many maintenance machines, so it is not economical to hold more pieces of equipment or machines than necessary. Therefore, we have developed a tamping schedule planning system (mMTS: Multiple unit MTTs Scheduler), rail grinding planning system (mRGS: Multiple unit Rail grinding Scheduler), and ballast renewal planning system (NDS: New ballast scraper, Dynamischer gleis stabilisator (German) & dump truck operation Scheduler) as tools that can investigate the number of machines owned for each type of maintenance.

These systems use track irregularity, rail condition, and ballast renewal locations as input data in the area where the maintenance machines operate. Then, the systems create an operation plan for multiple maintenance machines with the constraints of maintaining a certain level of track condition and performing maintenance in locations where maintenance is required.

Figure 2 shows an example of trial calculations for a section of track approximately 500 km long and managed by four track maintenance districts. The results of the calculated track condition (i.e., standard deviation of longitudinal level irregularity) when the number of MTTs in that section was varied from 1 to 4 are shown in the figure. When the track condition that can be maintained with four MTTs is set to 1, the track condition that can be maintained with three MTTs remains almost same. On the other hand, if the number of MTTs is further reduced, the track condition will deteriorate. These results can be used to determine the appropriate number of maintenance machines that each railway operator needs to have available.

2.2 Structural improvements in order to reduce track maintenance costs

2.2.1 Roadbed improvement method for ballast-less tracks for existing line [3]

Improvements to the roadbed need to be considered when constructing a ballast-less track in existing line on a soft roadbed, but to date, there has been no roadbed improvement method that can be constructed at the same time as a ballastless track in the short period of time available for night work. Therefore, we have developed a roadbed improvement method that can be constructed in a short period of time, as shown in Fig. 3.

In this method, the roadbed improvement layer is laid on a soft bed at the same time as the ballastless track by temporarily replacing the improved part with new ballast and filling it with grout at a later date in order to form a strong improvement layer. This enables the laying of a trackbed reinforcement layer which meets strength requirements, even in a short period of time.

Fig. 3 Post-filling roadbed improvement method that can be constructed at the same time as existing ballast-less track

Furthermore, a full-scale model test and bending fatigue test of the filled trackbed were carried out to evaluate the settlement characteristics of the ballastless track 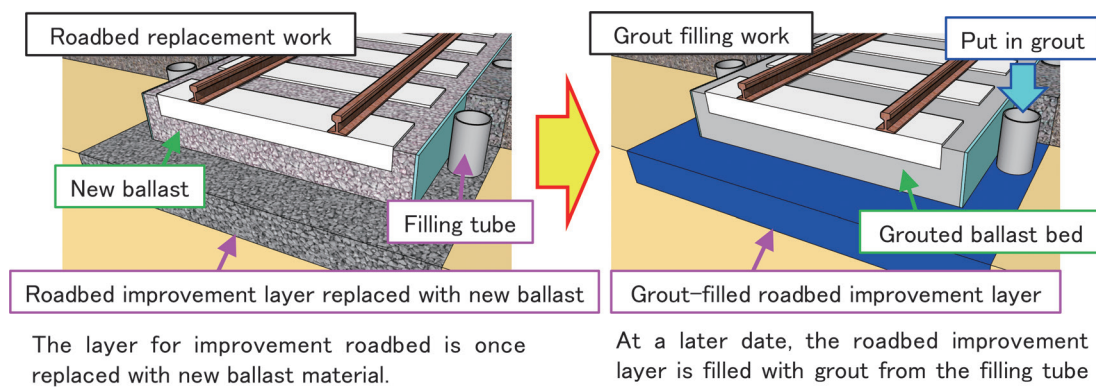and fatigue fracture characteristics of the filled trackbed, and we proposed a design method that takes into account roadbed settlement and fatigue fracture of the filled trackbed.

The effectiveness of these construction methods and design methods was confirmed by conducting on-site test construction.

2.2.2 SFC-filled trackbed track [4]

In order to improve the workability and cost effectiveness of filled trackbed tracks, which is a kind of ballastless track for existing lines, we developed a low-cost filled trackbed track (SFC-filled trackbed track) as shown in Fig. 4, which solidifies the existing trackbed using superfine cement (SFC) milk for grout material.

This track can be applied to a wide range of target areas by constructing an SFC improvement layer on the trackbed considering the presence or absence of mud pumping if the roadbed strength can be secured above a certain level. Results of repeated load tests by constructing a full-scale track for the developed construction method confirmed that the number of sleepers and roadbed settlement after assuming cases where the train passed for long periods of time was sufficiently small, and that it had sufficient performance as an existing ballastless track. Results of on-site test construction also showed that construction of approximately 10 m was possible in one night work shift, the longitudinal irregularity after construction was stable even after over a year, and favorable conditions could be maintained.
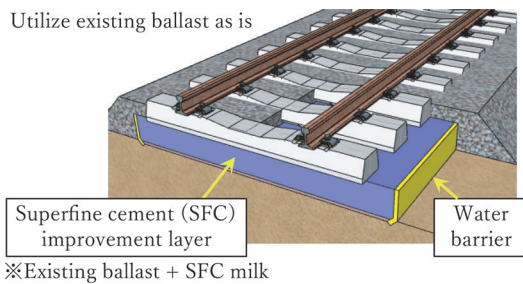
Fig. 4   Low-cost filling trackbed track (locations with no mud pumping)

3.   Maintenance cost / labor reduction of track inspection

3.1   Wooden sleeper inspection system [5]

As mentioned in Section 2.1.1, walking along a track and visually inspecting a huge number of sleepers in sections that are mainly composed of wooden sleepers is labor intensive and thus a heavy burden on railway operators.

Therefore, as shown in Fig. 5, we used a commercially-available video camera to take images of a track from the front of a commercial train. This was used to create a pseudo-trackbed image through projective conversion, to which deep learning and image processing were applied. As a result, we developed a system that identifies the positions of rail joints, extracts wooden sleepers, and determines the extent of deterioration. Of these, regarding the wooden sleeper deterioration judgment, we compared the diagnostic results that were determined by a track maintenance engineer from the images with the diagnostic results that were obtained by the present method. Results confirmed that the extent of sleeper deterioration (four levels) could be evaluated with an accuracy of 90% or more. It was also possible with this method to calculate the train speed and mileage using the acquired images.

We are currently developing a GUI for the system to facilitate practical use.

3.2   Image analysis engine for supporting onboard track patrol [6]

Onboard track patrols are performed by track maintenance staff aboard commercial trains, whereby they visually check for any abnormalities in the environment along the track. However, there is a need for automation due to the decreasing number of track maintenance staff in the future. Therefore, we developed an image analysis engine that applies image processing and machine learning techniques in order to automatically extract obstacles fouling the track clearance envelope from images taken along the railway lines by a stereo camera installed at the front of a commercial train (Fig. 6).

First, we developed a self-positioning estimation technique that complements the GNSS position information by estimating three-dimensional changes in the camera position and orientation using stereo images. We then developed an automatic detection technique for obstacles fouling the track clearance envelope, that utilize the 3D point cloud data constructed from the above estimation technique. This technique involves detecting rails from images, which makes it possible to set a track clearance envelope frame considering the alignment that was estimated.

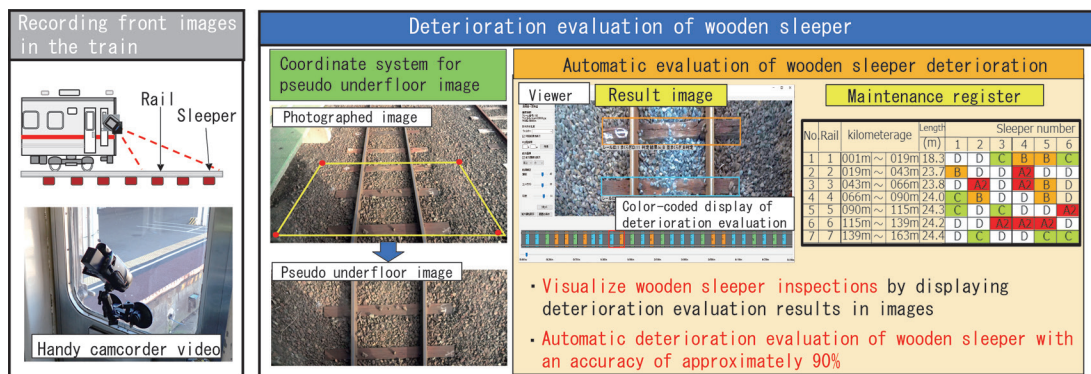We also developed a difference detection technique that auto-

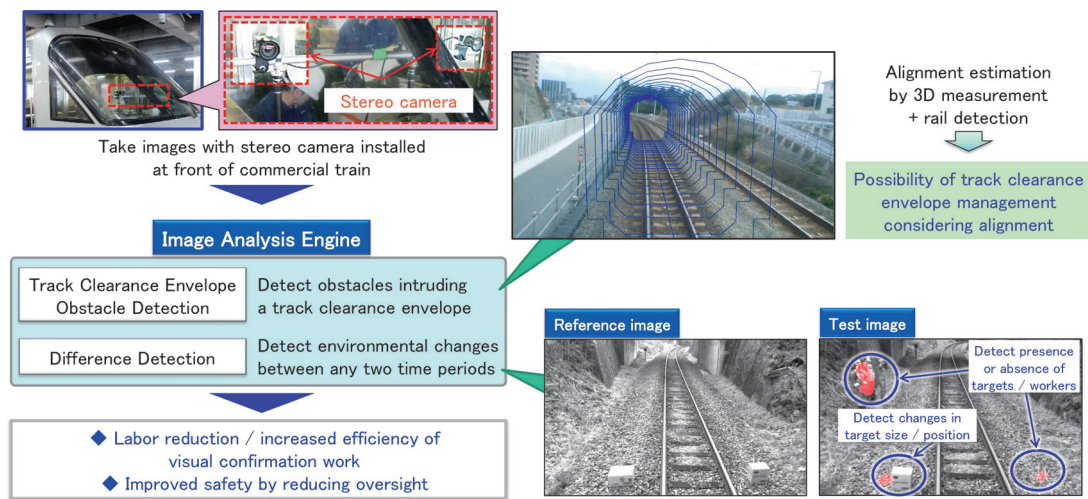**Fig. 5   Wooden sleeper inspection system**

Fig. 6 Track periphery image analysis engine

matically detects environmental changes along the railway line from images taken at different times. This technique automatically associates the frames that were taken at the same position in the video taken at different times. Then, in order to increase the practicality, we developed a technique for suppressing over-detection by classifying the type of subject (e.g., weeds) from the image and detecting areas such as blind spots to exclude them from the output. Part of this research was conducted with a grant for railway technology development from the Ministry of Land, Infrastructure, Transport and Tourism.

3.3 VR track inspection, construction, and work planning support system [7]

Track maintenance work involves many inspection items that require on-site surveys and measurements. Thus, there is a need to go on-site for each inspection, which is labor and time intensive. Similarly, there is a need to go on-site before formulating the construction / work plan in order to calculate the area of the target range and the amount of required materials as well as to confirm the presence of obstacles, which raises the same problems as mentioned above.

Therefore, we are developing a system that constructs a VR track space on a PC using image data of railroad tracks and equipment taken from the railway vehicle or on the ground, which is then used to conduct field surveys for inspections and construction / work planning in the VR space.

Figure 7 is an example of a rail extracted from an image taken at the front of the train and calculating the track irregularity. There is a deviation from the measured value in some parts, but the results are fairly consistent, which means that the track irregularity can be measured without using an inspection device. Furthermore, the track displacement can be projected in the constructed 3D space, which enables confirmation of situations where track displacement is large (e.g., intervention of ground equipment), thereby allowing for the track irregularity maintenance methods and investigation of the scope of maintenance without on-site visits.

Figure 8 is an example of measuring and determining platform inspections (gap, height) and trackbed shape using images taken from the railway vehicle. The distance from the platform had an average difference from the on-site measured value (i.e., error) of approximately 1%, and we are currently working to further improve its accuracy. We can also determine the location where the ballast shoulder is insufficient for the trackbed, so the location and the amount of dispersion in the trackbed can be investigated without on-site visits.

Systematizing these techniques should reduce the number of round trips / site visits as well as night shifts for track maintenance staff, improve safety, and reduce personnel and expenses, such as for train guards.
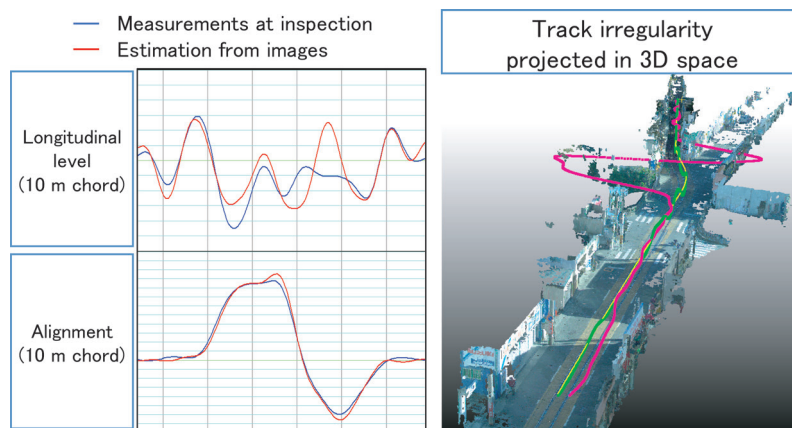

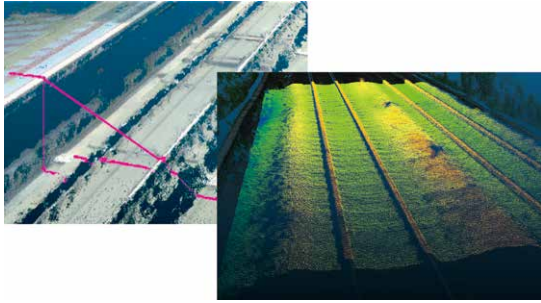**Fig. 7 Image-based track inspection results and display**

Fig. 8 **Image-based platform inspection and trackbed dispersion investigation**

4. Conclusion

Currently, RTRI is developing various technologies and solutions to optimize maintenance cost and save labor, in addition to the technologies and deliverables that are introduced in this paper.

We look forward to continued support and cooperation within the railway community to pursue track technology development at RTRI in the future.

References

[1] Deshimaru, T., Yamaoka, D., Ito, K., Shimizu, S., "Design Method for Ballasted Track Applicable to Widening of Sleeper Spacing," *RTRI Report*, Vol. 36, No. 3, pp. 23-28, 2022 (in Japanese).

[2] Nishijima, Y., Miwa, M., "Optimization of the number of MTTs owned and track maintenance planning considering MTT performance," *Journal of Japan Railway Civil Engineering Association*, Vol. 58, No. 5, pp. 347-350, 2020 (in Japanese).

[3] Ito, K., Momoya, Y., Kageyama, T., "Design Method for Roadbed Improvement for Existing Ballastless Track," *RTRI Report*, Vol. 36, No. 3, pp. 35-40, 2022 (in Japanese).

[4] Fuchigami, S., Nakamura, T., Takahashi, T., Momoya, Y., "Evaluation of Settlement Characteristics for Grouted Ballasted Track Applied to Ballasted Track with Mud Pumping," *RTRI Report*, Vol. 36, No. 3, pp. 41-46, 2022 (in Japanese).

[5] Konno, S., Kawasaki, K., Mishima., K., Miwa, M., Shimizu, A., Nakajima, N., "Image Analysis Engine for Supporting Onboard Track Patrol," *RTRI Report*, Vol. 36, No. 3, pp. 5-10, 2022 (in Japanese).

[6] Itoi, K., Nagamine, N., Goda, W., Tsubokawa, Y., Kato, S., "Improving Inspection Accuracy of Wooden Sleeper Deterioration Analyzing Forward View Image from Train Cab," *J-RAIL 2021*, SS2-4-5, 2021 (in Japanese).

[7] Mishima, K., Kawasaki, K., Konno, S., Saito, D., Miwa, M., "Track Condition Monitoring by Using Forward View Image for Work Saving of Track Maintenance," *Journal of railway engineering,* No. 25, 2021 (in Japanese).

Author

Yoshitsugu Momoya, Dr. Eng.
Director, Track Technology Division
Research Areas: Track Technology, Geotechnical Engineering

Recent Topics on Human Science for Railways

Naoki MIZUKAMI
Human Science Division

The Human Science Division of the Railway Technical Research Institute in Japan, has been conducting research on prevention of human error and safety management as well as measures against transport disruptions and to improve user environments in order to ensure better railway safety, convenience and comfort. This paper outlines recent outcomes from representative research on prevention of human error accidents and improvement of user environments.

Key words: *human science, human error, safety management, improvement of user environment, comfort*

1. Introduction

The Railway Technical Research Institute (RTRI) is engaged in research and development aimed at solving problems and proposing countermeasures for improving railway safety, convenience, and comfort for railway workers, users, and related systems. Efforts for improving safety include research and development on the prevention of human error accidents, industrial accidents, and railway crossing accidents, as well as the safety management support related to these issues. Efforts for improving convenience and comfort include research and development relating to accessibility measures for users and improvement of the user environment, such as the sanitary environment.

In this paper, we focus on driver support related to human error accident prevention, safety management support, and the improvement of hygiene and comfort as an improvement to user environments. In addition, we introduce measures designed to tackle railway crossing accidents which involve factors outside the railway system and outside railway operator control, and trends in research and development, the latest findings, and outlook for each of these areas of work.

2. Research and development related to humanerror accident prevention

We are engaged in the development of individual education and training methods, development of driver support systems, and management support such as accident recurrence / prevention and disaster response in order to prevent human error accidents caused by railway workers. Here, we introduce research and development of the estimation of the physical and mental condition of drivers who use digital technologies as well as management support when responding to natural disasters, as representative forms of recent research and development.

2.1 Technological development of estimation of mental and physical condition of drivers

We are engaged in research and development for monitoring and supporting drivers in order to prevent human error and accidents caused by low attention (i.e., drowsiness) while operating, or psychological agitation when encountering an abnormal event. For example, it is assumed that drowsiness is detected and an alarm is sounded, or a command is sent and support given to drivers in a state of psychological agitation. There are two types of driver monitoring technology: one involving no contact with the driver, and the other where the driver is equipped with sensors. There are differences in the range of

movement of the driver that can be monitored and the feeling of contact and restraint with the body: RTRI is conducting research and development on both types. Research into 'no-contact' approaches includes photographing drivers with a camera, to which image analysis technology is applied to detect drowsiness or sleeping [1, 2]. Another system is being developed which sounds a voice alarm before a driver transitions to heavy drowsiness. This paper introduces a sensor-based approach, which involves research and development on a method for estimating the mental and physical states of hypertonia and decreased arousal by utilizing physiological indicators [3].

Thus far, we have conducted experiments that used simple railway driving simulators in order to investigate brain activity and autonomous nervous indicators during psychological agitation by simultaneously measuring multi-channel high-density electroencephalographs, electrocardiograms, and operating behavior. We also investigated the relationship between physiological indicators and operating behaviors when a sudden noise stimulus was given in order to induce psychological agitation during the performance of a cognitive task that abstracted operating work. As a result, we were able to capture changes in prefrontal cortex brain activity, heart rate, respiration, pupil diameter, etc., that correspond to the behavior of the experimental participants when an abnormal event occurred.

These have revealed characteristic changes in brain activity and autonomous nervous indicators during psychological agitation. However, it is unrealistic to utilize brain waves as an indicator when estimating the mental and physical condition of drivers in the future due to the electromagnetic noise environment in the driver's seat and the complexity of measurements. These also need to detect a wide range of mental and physical states, from low arousal levels to very tense states. Therefore, we focused on autonomous nervous indicators, which have been studied in many previous studies on tension and stress evaluation, and we sought to deepen estimation methods using the heartbeat and respiration from a practical standpoint, such as stability and ease of measurement. We conducted experiments using a railway driving simulator for typical adults, where subjects were asked to conduct three types of tasks (operations): proficiency tasks to become accustomed to operation, tasks where obstacles appear on track, and time pressure tasks in which there is no spare time when operating. Of these, the time period during which a train was stopped after the driver became accustomed to it was defined as the 'non-tension' section, and the time during which the diver did not become accustomed to the driving and immediately before train stopped at stations in the time pressure task was defined as the 'tension' section. The indicators used for estimation were the heart rate interval (time interval of electrocardiogram peak), respiratory length (length of one breath), parasympathetic

nerve indicator RC (difference between maximum and minimum value of respiratory heart rate variability component per breath), heart rate regularity (regularity of heart rate interval), and respiratory regularity (regularity of respiratory cycle).

Until now, it has been said that physiological indicators had large individual differences, and that it is difficult to quantify judge them in everyday mental and physical conditions. In response to this, in the present report, we proposed a method in which we select effective indicators that are suitable for estimating the state of tension and non-tension for each individual, assume that a tension / non-tension state occurred when any of these indicators corresponded to a "change" according to the change criteria that were set in advance, and make a comprehensive judgment. According to this method, many judgments of tension appeared in the tension section, and many judgments of non-tension appeared in the non-tension section, and we were able to detect both states in 10 experimental participants with a misjudgment rate of 15% or less. This method will be verified during operation of an actual railway vehicle in the future, and we are considering its utilization in a support system.

2.2 Support for creating a resilient workplace / organization

The intensification and frequent occurrence of natural disasters in recent years have become a threat to the safety and stability of transportation. The Japanese national government has clearly included "natural disaster response" in the basic policies and guidelines for transportation safety management that transportation companies are engaged in, and the "Transportation disaster prevention management guidelines" have been formulated as a reference when constructing and implementing a disaster prevention system. There is a need under such circumstances to enhance workplace activities for minimizing damage and early recovery after a disaster, or in other words, to create a resilient organization / worksite. Resilience is defined as the ability to adapt to reactions to a disturbance, but the ideal method and preparation for resilience evaluation in the railway business was unclear.

Therefore, we reviewed the existing workplace safety climate evaluation method [e.g., 4], from the perspective of resilience; and we worked on the development of a method for evaluating workplace activities for early recovery in the event of a disaster based on survey results of response to frequent rainfall disasters [5]. We conducted interviews with site managers regarding the actual circumstances of responses to rainfall disasters, measures for safe and early recovery, and measures for preventing the spread of damage; and we created candidates for evaluation items for workplace activities. Next, we conducted a fact-finding survey of the activities of each workplace (crew, civil engineering, track maintenance, electric power, signal / communication, railway vehicle). We then defined a calculation method for the following evaluation items: 25 evaluation items (e.g., information transmission) and representative items (e.g., implementing confirmatory conversations during regular information transmission) for workplace managers for evaluating workplace activities in preparation for disasters, and 14 evaluation items (e.g., understanding of judgment criteria) and representative items (disaster response flow and ease of understanding judgment criteria) for field employees. Investigating the relationship between these evaluation values and the actual response in the event of a disaster [6] showed that workplaces that were "ultimately able to recover faster than originally expected," when compared to workplaces that did not, had high evaluation values among the evaluation items of "review after disaster response," "management of resources and information," and "safety climate in the workplace," and it was confirmed that these evaluation values were valid.

We also analyzed the relationship between the method of presenting evaluation results of workplace activities and the extent of improvement [7], and it was found that the extent of improvement was greater when comments on the low-evaluation results were added rather than simply presenting the evaluation values. Based on these results, we proposed the design proposal shown in Fig. 1 as a method of presenting the evaluation values.
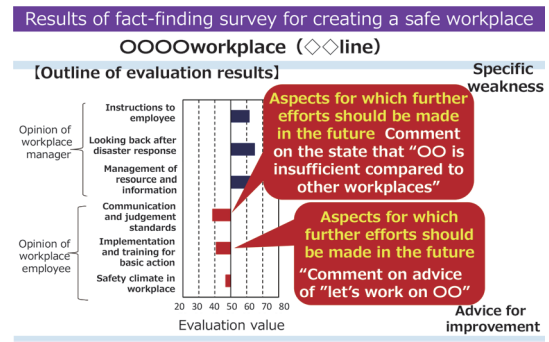

Fig. 1   Presentation design of evaluation results [5]

3. Improving user environments

In this section, as part of our work to maintain and propose effective and efficient hygienic environments, we introduce research and development on the construction of a method for visualizing microorganisms [8] and the overall evaluation method that is used when considering measures for improving comfort [9].

3.1 Efforts to improve sanitary environments

Maintaining and improving environmental hygiene in railway vehicles and train stations are important in terms of the safety, security, and comfort of users and railway workers. The transportation safety management system guidelines were revised in 2017, and a description of infectious disease response efforts was added as one of the aspects of safety management that was expected of transportation companies. In advance of these changes, RTRI had already obtained detailed information on microorganisms in the railway environment and been engaged in research that proposes more effective and efficient cleaning and disinfection methods as well as being able to provide scientific evidence that can be used as a basis for making decisions in the introduction of antibacterial and antiviral materials [e.g.,10]. With the recent novel coronavirus infection (COVID-19) pandemic, users have become more interested in the sanitary environment of public transportation.

Therefore, we have determined the overall picture of microorganisms such as bacteria and fungi that exist on-site (called a microbiome) using genetic information as part of a microbiome analysis technology and constructed a method for visualizing microorganisms in the railway environment [8]. This method was used to determine the types and proportions of microbial genes such as the surface of vehicle equipment and floating / accumulated dust and to analyze the origin of microorganisms that were present in railway vehicles. Results then showed that the handrails and straps that humans directly touch had a high proportion of human-derived bacteria (Fig. 2). The pathogens that were excreted from the infected people were usually thought to be excreted together with microorganisms that inhabit the body of individuals even when healthy, and this knowledge can be utilized for extracting the parts of interest regarding reductions in the

chance of infection by monitoring the environment using human-derived microorganisms as an indicator. We are also working on optimizing maintenance cycles by monitoring the number of microorganisms using gene quantification techniques such as digital PCR.
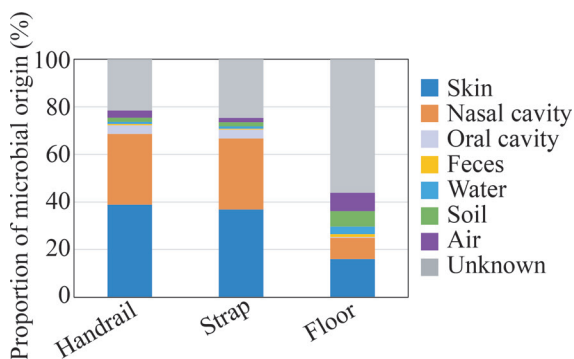

Fig. 2　Microbial origin estimation results [8]

3.2　New efforts for comfort evaluation

The main approach in conventional research on comfort was to propose a comfort evaluation indicator for the target factor and utilize it in improvement measures. Based on the recent progress of digital technology, Suzuki et al. stepped up their efforts for maintaining and improving comfort and proposed the following series of cycles: 1) digitalization of factors that influence comfort and data collection through networks; 2) utilization data analysis to reproduce comfort level with a digital model and grasp / predict the situation; 3) judgment of measures to improve comfort; and 4) accurate automatic control of the environment [11]. For example, the thermal environment inside a train station or railway vehicle sequentially changes depending on factors such as temperature, humidity, radiant heat, air flow, degree of congestion. Accurately analyzing and predicting these and achieving an optimal thermal environment results in "thermal comfort control by digitalization." The thermal environment in the railway vehicle was conventionally managed by the conductor; however, automatic control through the introduction of digital technology is indispensable when assuming more detailed service provision and future unmanned railway vehicle operation. Furthermore, to date, improved comfort was often investigated for each individual area such as stations or inside railway vehicles. However, from the user perspective, comfort and satisfaction when using the railway is impacted by various factors relating to the series of experiences involved in railway use, from planning of railway use to boarding / transfer and arrival at the destination. Therefore, effectively improving comfort by controlling and improving individual comfort factors and enhancing the superiority of railways requires clarifying the passenger evaluation structure that leads to overall comfort. To this end, we investigated the relationship between the overall comfort of passengers in their travel experience and the comfort of each phase of travel.

We set six representative passengers according to user attributes and purposes of use, identified the comfort factors that were predicted from prior knowledge, and conducted a web survey in February 2020, prior to the spread of COVID-19, on the comfort of passenger travel experiences. Based on this result, we adopted a multiple regression model as the evaluation structure model (Fig. 3) of the draft evaluation index that explains the overall comfort, and it was confirmed that approximately 70% of the comfort of the travel experience could be explained from the comfort of each travel phase. Survey results in

November, which factored in the impacts of the spread of COVID-19, also showed that the prepared draft evaluation index had a similar estimation accuracy, and that overall comfort could be estimated in a stable manner. This is thought to make it possible to efficiently take measures against comfort factors that contribute to overall comfort. We also created a conceptual diagram of overall comfort and individual comfort factors. In the future, we will promote research on the digitalization of environmental control based on the physiological and psychological characteristics of humans from a broad perspective.
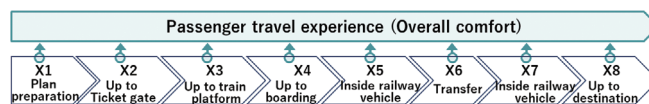

Fig. 3　Conceptual diagram of structural model (multiple regression model) of evaluation of the comfort of travel experience and comfort of each travel phase [9]

4.　Preventing pedestrians from entering crossings during alarm activation

In this section, we introduce research and development on railway crossing accident countermeasures [12]. In railway crossing accidents, the proportion of accidents caused by pedestrians (FY2015 to FY2018) was approximately 40%, and pedestrian measures are important in reducing railway crossing accidents. Given that 77% of pedestrian-caused railway crossing accidents are due to crossing immediately before the accident (entering the crossing while alarm is active), our work focused on this period of time. First, we conducted an internet survey in order to determine how railway crossing pedestrians understand the meaning of acoustic alarms. Results showed that 60% of the people who entered while the alarm was sounding, were unable to leave the railway crossing before the completion of the closing off of the space, and were left behind, recognized the alarm as a "warning" instead of the intended meaning of "no entry." Therefore, we proposed an additional measure of a voice message that states "no entry" by auditory information while the alarm is sounding, and the early descent of the barriers that communicates this message by visual information. The voice message stated "Danger. Please do not enter the railway crossing." The barriers were set to descend closer to the start of the alarm to block people from entering. However, the crossing had a slower descending speed of the barrier on the entry side and an unchanged descending speed of the barrier on the exit side, thereby making the timing of the completion of the barrier descent the same as the current setup.

We verified the effect of adding a voice message by conducting a simulated experiment that simulated railway crossing traffic. The experiment participants watched the CG image of the alarm sounding when approaching the railway crossing and selected whether to stop or enter in front of the railway crossing with the controller in their hands. Results confirmed that adding the voice warning reduced the percentage of pedestrians entering the crossing while the alarm was sounding by 25% compared to previously without the voice.

We also conducted a simulator experiment to verify the effect of blocking off access to the railway crossing earlier. The time from the start of the alarm sound to the start of the railway crossing being blocked, was set to two seconds, compared to four seconds for current crossings, which is standard when there are two crossing lines as set in this experiment. We also carried out the experiment using the current condition of four seconds and a delayed condition of six

seconds for comparison. The results in Fig. 4 show that the shorter time reduced the number of pedestrians entering while the alarm was sounding by 64% compared to current conditions.
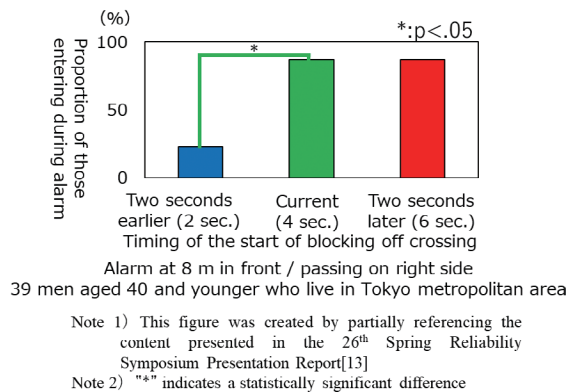

Alarm at 8 m in front / passing on right side
39 men aged 40 and younger who live in Tokyo metropolitan area

Note 1) This figure was created by partially referencing the content presented in the 26th Spring Reliability Symposium Presentation Report[13]
Note 2) "*" indicates a statistically significant difference

Fig. 4 Proportion of pedestrians entering crossing during alarm with earlier blocking of crossing [12]

5. Future outlook

This paper, introduced some of the recent human science studies that are representative of research and development related to safety improvement and user environment improvement. For the monitoring of drivers introduced first, we will build measurement technology for physiological indicators using wearable devices, verify these on drivers operating railway vehicles in actual operation, and connect this technology with system proposals. For creating resilient organizations and workplaces, we will promote the application of results and insights obtained from our research among railway operators. For measures to maintain and improve environmental hygiene with regards to microorganisms, we will pursue digitalization of the hygienic environment by quantifying the numbers of various microbes, which will lead to proposals for more effective and efficient cleaning and disinfection methods.

Regarding the prevention of pedestrians entering railway crossings when warnings are active, we changed the voice message and timing of closing barriers to block entry to the railway crossing earlier, and will continue these investigations to optimize the combination of these factors.

We will continue to pursue research on human factors that can contribute to the maintenance and improvement of railway safety and comfort, while taking into account the needs of railway operators.

References

[1] Mizukami, N., Nagamine, N., Nakasone, R., Hatakeyama, N., Hayama, K., Dongsheng, C., and Ran, D., "Drowsiness Detection Technique for the Support of the Train Operation of the Train Driver," *RTRI report*, Vol. 33, No. 1, pp. 11-16, 2019 (in Japanese).

[2] Hoshino, K., Suzuki, A., Asahina, M. and Makita, N., "Design and Evaluation of Auditory Warnings for Preventing Arousal-Level Decline during Monotonous Tasks," *Proceedings of the Human Interface Symposium*, 2021, pp. 487-494 (in Japanese).

[3] Nakagawa, C., Watanabe, T., Akiu, N., Kojima, T., Yoshie, S. and Suzuki, A., "Estimating the Physical and Mental State of Drivers Using Physiological Indicators," *Quarterly Report of RTRI*, Vol. 63, No. 4, pp. 276-282, 2022.

[4] Miyachi, Y., Murakoshi, A., Akatsuka, H. and Suzuki, A., "Development of Evaluation Method of Safety Climate in Work Site," *RTRI Report*, Vol. 23, No. 9, pp. 23-28, 2009 (in Japanese).

[5] Miyachi, Y. and Hayama, K., "Evaluation Method for Workplace Activities to Achieve Resilience," *RTRI Report*, Vol. 36, No. 1, pp. 5-10, 2022 (in Japanese).

[6] Miyachi, Y. and Hayama, K., "Supporting workplace learning of disaster response behavior on railway," *Ergonomics*, Vol. 57, Supplement, 1F1-4, 2021 (in Japanese).

[7] Miyachi, Y. and Hayama, K., "Attempt to promote workplace activities to improve disaster resilience on railways," presented at the *36th Annual Meeting of Japanese Association of Industrial/Organizational Psychology*, 2021 (in Japanese).

[8] Yoshie, S., Ikehata, M., Kawasaki, T., Kyotani, T. and Ushiogi, T., "Evaluation of Environmental Hygiene in Railway Vehicles Using Microbiome Analysis," *Quarterly Report of RTRI*, Vol. 63, No. 4, pp. 283-288, 2022.

[9] Kikuchi, F., Nakagawa, C., Saitou, A., Tatsui, D., Ishizuki, M. and Suzuki, H., "Evaluation of Overall Comfort in Railways Based on Customer Experience," *Quarterly Report of RTRI*, Vol. 63, No. 4, pp. 289-294, 2022.

[10] Kawasaki, T., Kyotani, T., Ushiogi T., Fujinami, K. and Hayakawa, T., "Assessment of the Effects of Airborne Microorganisms on Indoor Air Quality of Railway Stations," *RTRI Report*, Vol. 22, No. 5, pp. 35-40, 2008 (in Japanese).

[11] Suzuki, H., "Comfort and Digitalization," *Ascent*, No. 6, pp. 5-8, 2019.

[12] Kaburagi, T., Akiu, N., Saitou, A. and Miyachi, Y., "Measures to Prevent Pedestrians from Entering Level Crossing during Warning Alarm Based on Voice Alarm and the Start Timing of Level Crossing Rod," *RTRI Report*, Vol. 36, No. 1, pp. 35-40, 2022 (in Japanese).

[13] Kaburagi, T., Hayama, K., Hatakeyama, N., Murakoshi, A. and Miyachi, Y., "Results of the Experiment on the Effect of the Shortening of the Notice Time on the Deterrence of the Entry into the Level Crossing during the Notice Time When a Warning is being Given," *Proceedings of Spring Symposium on Reliability*, pp. 65-68, 2018 (in Japanese).

Author

Naoki Mizukami
Director, Head of Human Science Division
Research Areas: Ergonomics

Anomaly Detection for Railway Vehicle Equipment Using Condition Monitoring Data

Toshihide YOKOUCHI   **Tatsuro TAKASHIGE**   **Minoru KONDO**

Traction Systems Laboratory, Vehicle Technology Division

In recent years, some railway vehicles have been equipped with condition monitoring devices, which constantly record the operating condition of railway vehicle equipment. For more effective use of condition monitoring devices, we propose an anomaly detection method for railway vehicle equipment using Long Short-Term Memory (LSTM), which is a deep learning method suitable for learning time-series data. In this paper, we apply the proposed method to data on engines and air-conditioning units recorded on vehicles in operations. Results confirmed that the anomaly score for anomalous data increases by using the proposed method, and that anomalies are detected in railway vehicle equipment before faults appear.

Key words: *anomaly detection, machine learning, LSTM, rolling stock, smart maintenance*

1. Introduction

Recent innovations in IT devices have dramatically increased the computing power and storage capacity of computers. These improvements have made it possible to record vast amounts of data about the status of operating equipment in plants and factories in real time and with high temporal resolution. The recorded data are used to monitor condition of equipment and to investigate causes of equipment failures in detail. The former is particularly expected to contribute to a variety of areas. The use of these data enables us to constantly or more frequently to monitor equipment condition to prevent failures or mitigate their consequences.

Railway vehicles comprise a vast amount of equipment. Therefore, railway operators invest significant resources to maintain railway vehicles to prevent failures. On the other hand, it is impossible to completely prevent railway vehicle equipment failures during operation, and some failures may significantly impact operations. Therefore, railway vehicles have functions that warn crews or stop equipment when an anomaly is detected. Anomaly detection functions have been used to detect failures such as overcurrent in traction motors or earth faults in traction circuits, which cause significant disruption. In addition, some systems that constantly monitor the state of axle bearings, which may also severely impact operations if they fail, have been put to practical use [1]. These systems consist of temperature sensors or vibration acceleration sensors in axle boxes, and crews are warned when a monitored value exceeds a threshold. Some monitoring systems for bogies using air spring pressure sensors are also in practical use [2]. In other cases, there are also monitoring systems installed on the ground side that detect anomalies in axle boxes, brake discs, wheel treads, pantographs, and other components.

However, there are still some pieces of railway vehicle equipment for which anomalies are not detected by any current monitoring system. Furthermore, some equipment anomalies cannot be detected with simple thresholds. To address these issues, many attempts have been made to improve reliability of train operations as seen in "Smart Maintenance" in Europe [3] and in Japan [4]. This work aims to upgrade the condition management of vehicle equipment by exploiting condition monitoring data of vehicle equipment. One method involves the constant recording of vehicle equipment condition using data existing on-board monitoring systems, and then using this data to detect anomalies or signs of failures. The advantage of this method is that it enables anomaly detection without installing additional sensors on vehicles. Recent advances in IT

equipment have made it possible for vehicle monitoring equipment to process condition monitoring data at high speed and with large memory capacity. As a result, railway vehicles record a large amount of the data. The data items include signal line on/off, traction motor current, engine rotational speed, air-conditioning system operating status, and many others. By analyzing condition monitoring data, it is possible to improve the reliability of vehicle operations by checking the condition of vehicle equipment and detect anomalies by analyzing condition monitoring data. However, it is not practical for on-site workers to look for signs of failures from the huge amount of recorded data in addition to their existing workload. Therefore, it is essential to detect vehicle equipment anomalies using the recorded data automatically.

Data analysis methods using machine learning have been developed recently, and it has enabled us to learn features in the complex data. In this report, we propose a method to automatically detect anomalies in vehicle equipment from condition monitoring data by utilizing Long Short-Term Memory (LSTM), which is a deep learning method. We also apply the proposed method to condition monitoring data collected from vehicles in service to evaluate effectiveness of the method.

2. Neural network

2.1 RNNs

Neural networks learn and reproduce relationships between inputs and outputs by combining nodes and edges. Neural networks are being used in various fields because of their flexibility in learning complex relationships. Recurrent Neural Networks (RNNs) are neural networks to model time series trends efficiently, where the outputs of a hidden layer at one time are input into the hidden layer the next time [5]. When RNN is trained with training data at time step t, the output of the node at time step t-1 in addition to the data at time step t are input to the nodes of the hidden layer at time step t. By including data from previous time steps, the history of the time series data is reflected in the training.

2.2 LSTM

The problem of RNNs is that it is difficult to reflect long-term histories of time-series data in the training process. LSTM addresses this problem by improving the ability to control the input/output
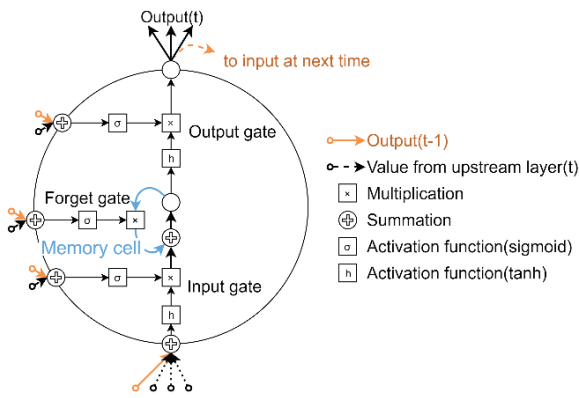
Fig. 1 LSTM block [10]

values of nodes. The LSTM block consists of input, output, and forget gates and memory cells, so to enable learning of long-term time series data [6]. An overview of the LSTM block is shown in Fig. 1. First, each gate controls the value passing through the gate based on the input at time step t and the output of the node at time step t-1. Next, the memory cell retains the internal state of time step t-1 until time step t. When the situation changes or an outlier is input, i.e., data with a different trend than before is input, the contents of the memory cell must be reset. Therefore, a forget gate is proposed as a mechanism to automatically reset the contents of the memory cells in response to changes in the data trends [7]. These functions make it possible to learn the history of long-term time-series data for 1000 steps (about 10 steps for RNN [5]).

2.3 Hyper parameters

In order to improve the learning accuracy of neural networks and the convergence of weight updates, the values of hyperparameters must be set appropriately. In this report, we describe Batch size, Lookback, and Dropout rate among the parameters related to learning. The batch size is the number of samples used to calculate the estimation error required to update the weights; the smaller the batch size, the more frequent the weight updates and the more detailed the features learned: however, computation time also becomes

longer. The lookback is the number of time steps to be read at one time in the input of the neural network; the larger the lookback, the longer the past data input is and the more estimations are made referring to past features, but again, computation time also becomes longer. Dropout is a method of learning which randomly disables nodes in the input or hidden layers at a fixed rate. The dropout rate is the rate at which the network is disabled and is expected to suppress overlearning because it changes the location where the network is trained.

3. Anomaly detection method for vehicle equipment

Condition monitoring data is time series data in which the operating condition of vehicle equipment is recorded. For anomaly detection based on time series data, it is effective to refer to temporal characteristics (i.e. waveforms and history) in addition to instantaneous values. In this report, we propose a method for training the data with a neural network incorporating LSTM as an effective method for learning time-series data. The method is divided into the following three steps [8][9][10] shown in Fig. 2.

3.1 Training

The neural network is trained with input and output items divided from the data under a normal condition. The input items should correlate to the output item. The neural network that has been trained becomes a trained model that reproduces a state in which vehicle equipment operates normally and estimates the output item ("A" in Fig. 2) with the input items. When normal data is newly input to the trained model, it is expected that the trained model estimates the output item with relatively small errors.

3.2 Making "Criteria"

Normal data are input into the trained model to obtain estimated values as output. Estimation errors between the estimated values and measured values are calculated for each time. Then, probability density distribution $p_n(d_n)$, "Criteria," of the estimation errors d_n under normal conditions is obtained with an appropriate distribution
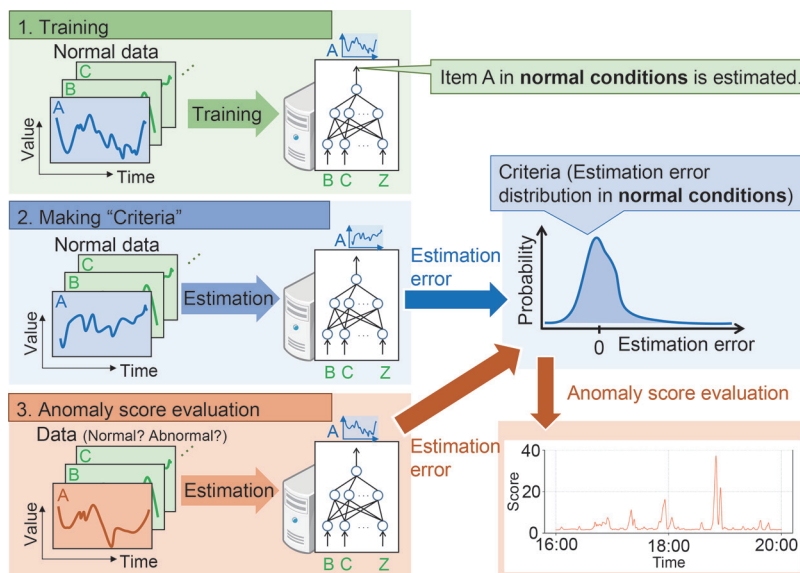

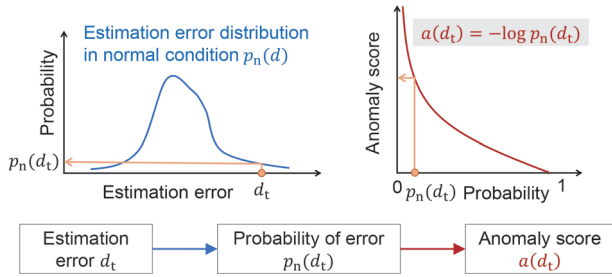**Fig. 2 Flow of anomaly detection**

Fig. 3   Anomaly score calculation [10]

estimation method such as Kernel density estimation. Criteria are expected to be a distribution centered around zero, since the trained model estimates the output item relatively accurately.

3.3 Anomaly score evaluation and anomaly detection

The anomaly score is estimated based on the estimation errors of test data. Estimation errors of the test data in anomalous conditions are expected to be larger than those in normal conditions when the output item is affected by anomalies. Therefore, based on the criteria, we define an anomaly score that becomes high for a high estimation error that appears infrequently in normal conditions.

Figure 3 shows the details of the anomaly score calculation. The probability $p_n(d_t)$ of the estimation error dt assuming it occurs under normal conditions is obtained for each time. Then, the anomaly score is calculated. The anomaly score is high when the estimation error deviates significantly from the criteria, i.e., in highly anomalous conditions.

In the anomaly detection, a threshold is set for the anomaly score, such as based on a probability of occurrence at the 99.9th percentile of the criteria. When the anomaly score exceeds the threshold, the anomaly is detected. However, in order to prevent excessive detections by instantaneous exceedances, a low-pass filter is applied to the anomaly score so that instantaneous exceedances are not judged as an anomaly.

4. Evaluation

We evaluated the proposed method by applying it to two types of monitoring data collected from vehicles in operations. One was for the engines on diesel trains where an engine overheating occurred, and the other was for the air-conditioning units on electric trains, where a compressor failure in an air-conditioning unit occurred.

4.1 Case 1: Engine

An engine is one of the most important pieces of equipment on diesel trains. Overheating of an engine can cause a train stop, which may in turn lead to significant line disruption. Therefore, engine failures need be detected in advance. Figure 4 shows an engine cooling system and items of collected condition monitoring data around the engine. Heat generated by the engine is released with a radiator via coolant. A radiator runs when temperature of the coolant is higher than the predetermined temperature due to continuous powering. Therefore, the temperature of the coolant in normal conditions is kept safe. However, when performance of the radiator has deteriorated for some reason, the temperature of the coolant rises to a dangerous value.
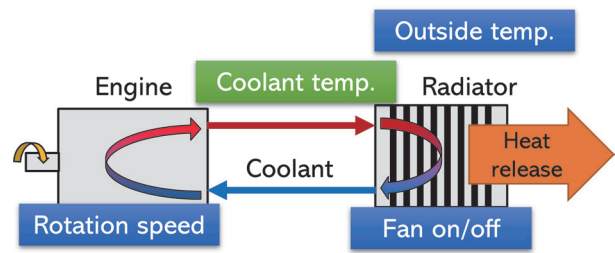

Fig. 4   Engine cooling system

Table 1   Datasets (engine)

Data	Label*	Vehicle	Term
Training	N	A	Jul. – Dec. 2020
Criteria	N	B	Jul. – Dec. 2020
Test	N→A	C	Dec. 2020

* N: Normal, A: Anomalous

Table 2   Training conditions

Optimization	Adam
Batch size	256
Lookback	30 (Engine)
	150 (Air-conditioning unit)
Dropout rate	0.1
Scaling	MinMaxScaler
Metrix	Mean squared error

Table 3   Input and output (engine)

Input (continuous)	Speed, Accel notch, Rotation speed of engine, Lubricant pressure, Atmospheric pressure, Fuel consumption, Outside temperature
Input (on and off)	Radiator
Output	Coolant temperature

4.1.1 Condition monitoring data

Table 1 shows condition monitoring data of engines. The training data was for about five months, and the criterion data was also for about five months. The test data to evaluate the degree of anomaly was for 11 days. The training data, criterion data, and test data were collected from different vehicles, but the vehicle type was the same. The test data is obtained in the last day when an engine overheated. The overheat was caused by poor heat exchange of the engine cooling system due to snow clogging around the radiator fan. The gradual clogging caused overheating for a day.

4.1.2 Evaluation

The training conditions are shown in Table 2, and the input and output items of the neural network in Table 3. The architecture of the neural network consists of 30 LSTM block layer and 30 node-layer as the middle layers. To focus on the overheat, "Coolant temperature" of the engine was selected as the output item, and items affecting the coolant temperature were selected as the input items. MinMaxScaler [11] was used as a data normalization method. It converts the maximum value to one and the minimum value to zero.

For calculating the anomaly score, the criterion was made by assuming a normal distribution due to a large amount of data, and a moving average of 100 samples (100 seconds) was taken as a low-pass filter.

4.1.3 Results

Figure 5 and Fig. 6 show the estimated coolant temperature and the anomaly score of the test data in normal conditions and the day of the overheating, respectively. The normal or anomalous data in Fig. 5 and Fig. 6 are for the same running section. The ambient temperature was about 0°C in normal conditions and about -5°C in the anomalous condition, which means that the radiator fan was easily blocked by snow clogging. The estimated coolant temperature indicates that the estimations were generally accurate in the normal conditions. On the other hand, in the anomalous condition, the measured values intermittently exceeded the estimated values in about 1.5 hours before the overheat occurred. This is due to that the coolant temperature in the anomalous condition easily increasing compared with the normal conditions. The heat exchange in the anomalous condition did not have a capacity to keep up with the continuous operation of the engine corresponding to the operation schedule and the route. The tendency to exceed this threshold was also reflected in the anomaly score. While the anomaly score in the normal conditions was generally around two, the anomaly score intermittently increased from about 1.5 hours prior to the overheat.

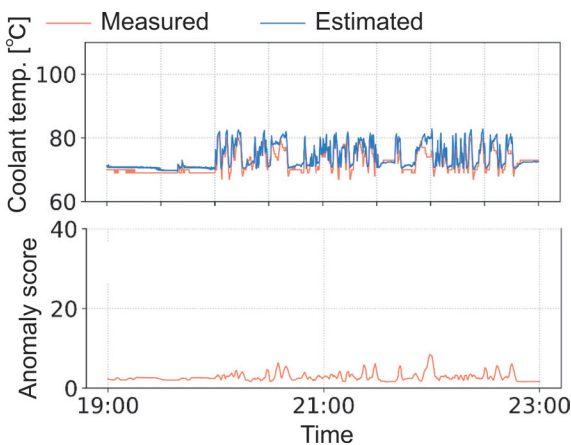The result shows that it was possible to capture the coolant temperature increasing associated with the overheat by using condition monitoring data even from different vehicles. This indicates that it is possible to use condition monitoring data from a common vehicle type to create a general model. In addition, an increase in the anomaly score was observed 1.5 hours prior to the time of the temporary stop due to overheating. By utilizing the method, the risk of failure during operation is reduced by having crews and employees confirm and address the condition of a vehicle before a failure occurs, and by adjusting operations if necessary.
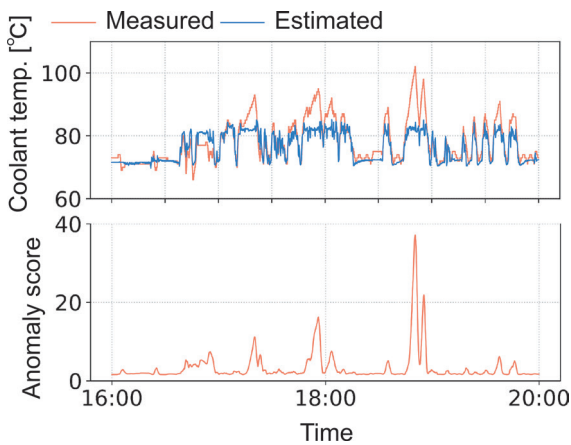
4.2 Case 2: Air-conditioning unit

Air-conditioning units are also important pieces of equipment for trains. Failure of air-conditioning units leads to passenger complaints and may even cause the train to be taken out of service. Therefore, this type of failure should be detected in advance. Figure 7 shows the heat exchange cycle and some of the items collected as monitoring data for air-conditioning units. In an air-conditioning unit, heat absorbed from cabin air is released through a refrigerant heat exchanger to the outside via coolant, then the blowing temperature is cooled to control cabin temperature. However, when the performance of the air-conditioning unit deteriorates for some reason, the blowing temperature rises abnormally.

4.2.1 Condition monitoring data

Table 4 shows condition monitoring data of air-conditioning units. Data from three to four months were used for training data, and data for creating the criteria were also from about three months in the same year as the training data. The sets of test data to evaluate the degree of anomaly were for three months in the year following the training and criteria data. Each data item was collected from different air-conditioning units. One of the sets of test data included
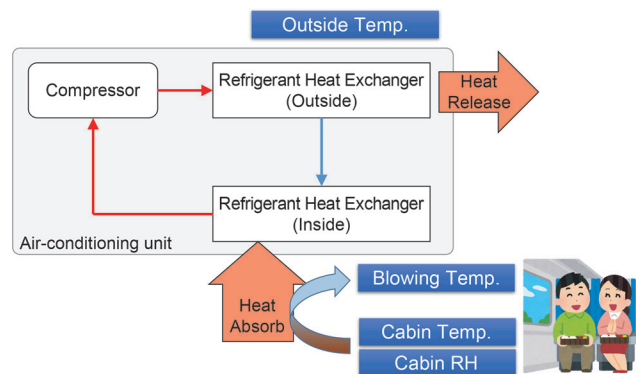
Fig. 5　Anomaly score (Dec. 9, 2020)

Fig. 6　Anomaly score (Dec. 17, 2020)

Fig. 7　Heat exchange cycle [10]

Table 4　Datasets (air-conditioning unit)

Data	Label*	Vehicle-unit	Term
Training-1	N	A-a	Jul. – Oct. 2016
Training-2	N	B-a	Aug. – Oct. 2016
Criteria	N	B-b	Aug. – Oct. 2016
Test-1 (T-1)	N	C-a	May – Jul. 2017
Test-2 (T-2)	N	C-b	May – Jul. 2017
Test-3 (T-3)	N	C-c	May – Jul. 2017
Test-4 (T-4)	A	C-d	May – Jul. 2017

* N: Normal, A: Anomalous

anomalous data where the blowing temperature did not cool enough due to deteriorated heat exchange performance. The fault was caused by a breakdown of a compressor in the unit. The fault possibly led to an insufficient circulation of coolant, and finally poor performance of the unit. The fault was identified by a crew on Jul. 13, 2017, then the vehicles were sent to a rolling stock depot on Jul. 18, 2017. The broken unit was replaced on Jul. 20, 2017.

4.2.2 Evaluation

The training conditions are shown in Table 2 and the input and output items of the neural network are shown in Table 5. The architecture of the neural network consists of 30 LSTM block layers and two 30 node-layers as the middle layers. To focus on the performance of an air-conditioning unit, "Blowing temperature" was selected as the output item, and items that affects the blowing temperature were selected as the input items. For calculating the anomaly score, the criterion was made by assuming a normal distribution.

4.2.3 Results

Figure 8 shows the daily average of the anomaly score. The anomaly score of T-4 rose in the last 1.5 months before the fault was identified, then suddenly settled down from 2.0 to 3.0 after the unit was replaced. The anomaly scores of other units remained between 2.0 to 3.0. This means the fault and the replacement of the air-conditioning unit caused rise and fall of the anomaly score, respectively. The score settled exactly before the replacement. This is assumed to be based on the reason that since the vehicles were put in a rolling stock depot two days before the replacement and the air-conditioning unit was barely run, the failure did not affect blowing temperature.

Figures 9 and 10 show the estimated blowing temperature on Jul. 16, 2017, for a normal and anomalous case, respectively. In the normal case, the blowing temperature is estimated precisely, while in the anomalous case, the estimated blowing temperature falls below the recorded temperature. The anomaly score in the anomalous case constantly fluctuates from 5.0 to 15.0, while the score for the normal case remains around 2.0.

Table 5   Input and output (air-conditioning unit)

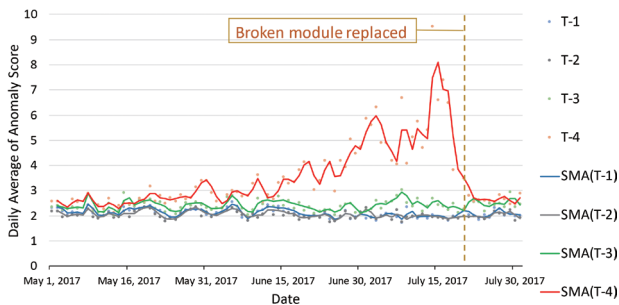| Input (continuous)	Speed, Air spring pressure, Outside temperature, Cabin temperature, Blowing temperature, Cabin humidity
Input (on and off)	Compressor, Bypass valve, Heater, Door open
Output	Blowing temperature

Fig. 8   Daily anomaly score average (solid line: two-segment SMA (simple moving average)) [10]

The result shows that it is possible to capture the insufficiently low blowing temperature associated with a deterioration in air-conditioning unit performance by using condition monitoring data even from different vehicles and terms. In addition, the increase in the anomaly score was confirmed 1.5 months prior to when the crew reported the failure. By utilizing this method, the risks of service degradation for passengers are reduced by replacing an anomalous unit before its failure appears. Furthermore, by applying the method to condition-based maintenance, it is possible to contribute to labor resource leveling, reducing required labor and costs.

5. Discussions

This research confirmed that trends in anomaly scores depend on type of equipment and failure. First, the speed at which anomaly scores increase differs between engines and air-conditioning units. In other words, some anomalies gradually increase like air-conditioning units, while others, as with engines, rise sharply. Furthermore, anomaly score trends can vary in a single day. In the evaluation of engines, for example, the anomaly score was actually normal when the engine was not running continuously, even though there was an anomaly. On the other hand, in the evaluation of air-conditioning units, the anomaly score remained high when there was an anomaly.

The conditions under which the proposed method can be applied are as follows:

- Failures are reflected in condition monitoring data.
- The input and output are correlated.
- Monitoring data contains a certain amount of continuous data.

If the conditions above are met, it is possible to detect an anomaly before or just after the failure has occurred.
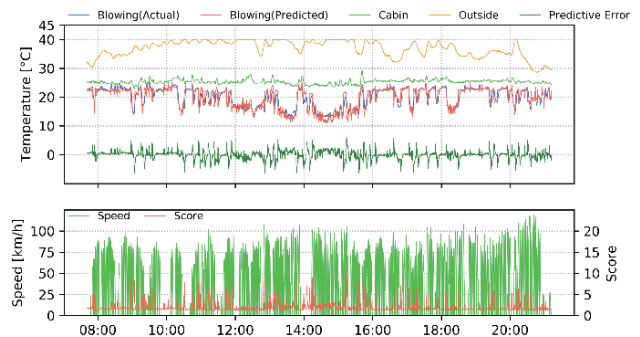

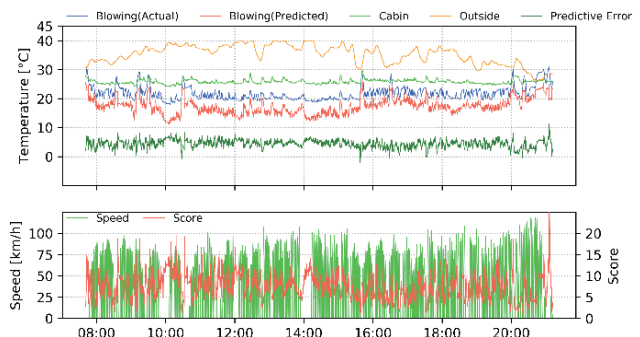**Fig. 9   Anomaly score of "T-1" (Jul. 16, 2017) [10]**

Fig. 10   Anomaly score of "T-4" (Jul. 16, 2017) [10]

6. Conclusions

We proposed an anomaly detection method using a neural network with LSTM, in order to detect anomalies of vehicle equipment using condition monitoring data. In this report, the proposed method was evaluated for two types of equipment failure. For engine overheating, it was confirmed that the coolant temperature anomaly in the engine increased before the overheating occurred. For air-conditioning unit performance degradation, the difference between normal and anomalous conditions was confirmed as the difference in the anomaly score. These evaluations showed the effectiveness of the proposed method.

References

[1] Perpetuum, Track Defect and Wheel Damage: Detection and Location., Accessed: Jun. 21, 2021. [Online]. Available: https://perpetuum.com/technology/

[2] S. Kita, et al., "Development of anomalous bogie detection method by the monitoring of the air spring pressure," *Proc. J-Rail 2018*, Vol. 27, Tokyo, Japan, Dec. 5-7, 2018, doi: 10.1299/jsmetld.2018.27.1213 (in Japanese).

[3] Shift2Rail, "Delivery of new smart maintenance concept & global safety framework!," shift2rail.org., https://shift2rail.org/news/read-about-the-latest-results-coming-from-cca/ (accessed Jun. 12, 2021).

[4] T. Anami, "Status of Initiatives for Smart Maintenance," *JR EAST Technical Review*, No. 39, pp. 5-10, 2020.

[5] A. Singh: Anomaly Detection for Temporal Data using Long Short-Term Memory (LSTM), Master's thesis at KTH Royal Institute of Technology and Communication Technology, 2017.

[6] Sepp Hochreiter, and Jürgen Schmidhuber, "Long short-term memory," *Neural Computation*, Vol. 9, No. 8, pp. 1735-1780, 1997.

[7] Felix Gers, J. Schmidhuber and Fred Cummins, "Learning to Forget: Continual Prediction with LSTM," *Neural Computation*, Vol. 12, No. 10, pp. 2451-2471, 2000.

[8] T. Yokouchi and M. Kondo, "Anomaly Detection for Train Equipment using LSTM," presented at the *J-RAIL2019*, Tokyo, Japan, No. S8-3, 2019 (in Japanese).

[9] Yokouchi, T., Takashige, T., and Kondo, M., "Anomaly Detection for Equipment on Railway Vehicle Using Condition Monitoring Data," *RTRI Report*, Vol. 36, No. 2, pp. 23-28, 2022 (in Japanese).

[10] T. Yokouchi and M. Kondo, "LSTM-based Anomaly Detection for Railway Vehicle Air-conditioning Unit using Monitoring Data," presented at the *IECON 2021*, Toronto, Canada, 2021.

[11] Pedregosa, et al., "Scikit-learn: Machine Learning in Python," *JMLR*, Vol. 12, pp. 2825-2830, 2011.

Authors

Toshihide YOKOUCHI
Researcher, Traction Systems Laboratory, Vehicle Technology Division
Research Areas: Condition Monitoring for Railway Vehicle

Tatsuro TAKASHIGE
Assistant Senior Researcher, Traction Systems Laboratory, Vehicle Technology Division
Research Areas: Condition Monitoring for Railway Vehicle, Diesel Engine

Minoru KONDO, Dr. Eng.
Senior Chief Researcher, Head of Traction Systems Laboratory, Vehicle Technology Division
Research Areas: Traction Motor, Condition Monitoring for Railway Vehicle

Evaluation of Influence of Reflection Point Shift on Axle Surface in Ultrasonic Flaw Detection

Kazunari MAKINO

Vehicle & Bogie Parts Strength Laboratory, Vehicle Technology Division

Ultrasonic inspection of axles to detect flaws, in which shear waves are emitted into an axle at certain angles, is widely applied. However, when shear waves are obliquely incident on a boundary surface, sound beam displacement may shift the geometric reflection point parallel to the boundary surface. In this study, two types of boundary surface, that is, an axle body and a wheel seat, are targeted. The relationship between a shear-wave incident angle and sound beam displacement is derived theoretically and then confirmed using finite element calculations. The propagation behavior of ultrasonic waves while inspecting surface flaws on an axle is discussed from the viewpoint of sound beam displacement.

Key words: *axle, ultrasonic flaw detection, sound beam displacement, shear-wave incident angle, boundary surface*

1. Introduction

Ultrasonic inspection of axles for flaw detection, in which shear waves are emitted into an axle at certain angles as shown in Fig. 1, is widely applied. Solid axles are inspected at different sites on the body surface, on which probes with different refraction angles are used. Hollow axles are inspected from their inner bore using an inserted probe head which is equipped with two angle probes, one of which emits ultrasound forward and the other backward.

Axles, or wheelsets, have certain free boundary surfaces, such as the axle body. However, they also have some boundary surfaces which are in contact with other fitted parts such as the wheels. Moreover, when a flaw exists on the surface of or inside an axle, an additional boundary surface appears at the opposite flaw faces. Now, when ultrasonic shear waves are obliquely incident on a boundary surface and total reflection occurs subsequently, the geometric reflection point shifts in the direction parallel to the boundary surface. This phenomenon is known as sound beam displacement [1-3]. When considering ultrasonic flaw detection of axles, it is therefore important and useful to fully understand the reflection behavior of

ultrasonic waves that are incident on such boundary surfaces.

In this study, we evaluated the influence of sound beam displacement on ultrasonic flaw detection of axles, targeting two types of boundary surface, that is, an axle body (free boundary surface) and a wheel seat (fitted part). First, we calculated the relationship between the shear-wave incident angle and the phase shift of reflected ultrasonic waves analytically and numerically, based on plane-wave reflection theory, which derives the relationship between the shear-wave incident angle and the sound beam displacement. Based on this finding, we then calculated the propagation behavior of ultrasonic shear waves obliquely incident on each boundary surface with a finite element (FE) model, to observe the sound beam displacement at the time of wave reflection at boundary surfaces.

Furthermore, we discussed theoretically the influence of sound beam displacement on the ultrasonic test results of surface flaws in axle bodies and the wheel seats of axles from the following two viewpoints: (i) the shift of reflected ultrasonic waves when a probe was placed at the position which geometrically faced a flaw; and (ii) the error of the flaw position, which was estimated from the probe position where the maximum ultrasonic echo from a flaw was obtained.

2. Theoretical investigation into sound beam displacement

2.1 An outline of sound beam displacement

When ultrasonic shear waves are obliquely incident on boundary surfaces and total reflection occurs subsequently as shown in Fig. 2, the reflected waves shift a distance D away from the geometric path [1]. When distance D is expressed by the shift of the reflection point in the x direction, that is, the sound beam displacement (SBD) Δ, the following equation is obtained [2, 3]:

$$\Delta = -\frac{\lambda}{2\pi}\frac{\partial\varphi}{\partial h} \qquad (1)$$

where λ is the wavelength of shear waves, φ is the phase shift of reflected waves against incident waves, and $h = \sin\eta_1$; η_1 is the incident angle of shear waves. The value of the sound beam displacement Δ divided by the wavelength λ, that is, Δ/λ, is referred to as the normalized sound beam displacement.

Wheel

Angle probe

Ultrasound

Axle

Axle body
(free boundary surface)

Wheel seat
(fitted part)

(a) Solid axle

Wheel

Probe head
(two built-in angle probes
moving rotationally)

(forward)

Axle

Ultrasound

Bore

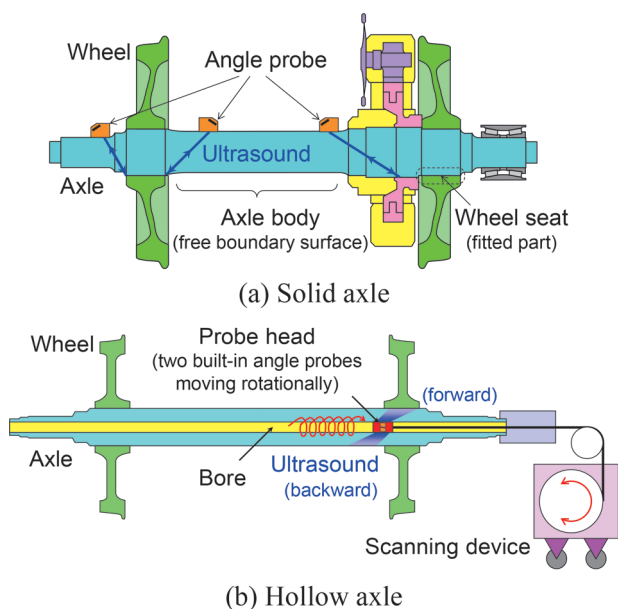(backward)

Scanning device

(b) Hollow axle

Fig. 1   Ultrasonic flaw inspection of axles

2.2 Sound beam displacement at the free boundary surface of an axle

When shear waves with an incident angle greater than the longitudinal-wave critical angle are obliquely incident on a free boundary surface of an axle (steel), the phase shift φ is obtained analytically by the following equation [2]:

$$\varphi = \tan^{-1}\left[\frac{8h^2\sqrt{h^2-q^2}\ \sqrt{1-h^2}\ (1-2h^2)^2}{16h^4\ (h^2-q^2)\ (1-h^2)-(1-2h^2)^4}\right] \quad (2)$$

where $q = c_T/c_L$; c_L is the longitudinal wave velocity and c_T is the shear wave velocity. Inserting (2) into (1), the relationship between the incident angle η_1 and the normalized sound beam displacement Δ/λ is obtained.

Figure 3 shows the relationship between η_1 and Δ/λ when the sound velocity in steel is set to $c_L = 5900$ m/s and $c_T = 3230$ m/s. When the incident angle η_1 is 45°, there occurs no sound beam displacement. When η_1 is smaller than 45°, sound beam displacement occurs in the positive direction of x which coincides with the x component of the propagating direction of incident waves, and when η_1 is larger than 45°, it occurs in the negative direction of x.

2.3 Sound beam displacement at the fitted surface of an axle

In the case of the axle–wheel interface of a wheelset wherein both surfaces are made of similar carbon steel, the acoustic impedances (product of density and sound velocity) of the materials on both sides of the boundary surface are almost equal. If this axle–wheel interface is treated as a perfect bonding surface, no reflection waves occur at the interface and the reflection behavior of ultrasonic waves cannot be expressed. Therefore, we applied a spring interface [4-6] to the axle–wheel interface, and in this manner, the sound beam displacement at the spring interface was investigated. Here we investigated a periodically cracked interface [7] shown in Fig. 4, which is equivalent to the axle–wheel spring interface, for ease of treatment in the calculation of ultrasound simulation described later in the paper. The periodically cracked interface is defined by the parameters s and w, which are the width of a periodic boundary and the width of a non-cracked part in s, respectively. In this model, the normal stiffness K_N, which corresponds to the spring constant normal to the spring interface, is given by:

$$K_N = \frac{E'}{s}\left\{\frac{4}{\pi}\ln\left[\sec\frac{\pi(1-w/s)}{2}\right]\right\}^{-1} \quad (3)$$

where $E' = E/(1-v^2)$ is the plane-strain longitudinal elastic modu-
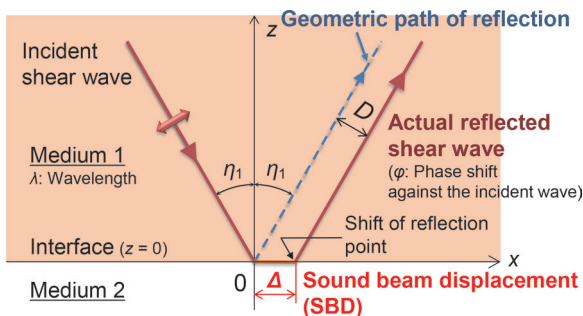
Fig. 2 Schematic of sound beam displacement (SBD)
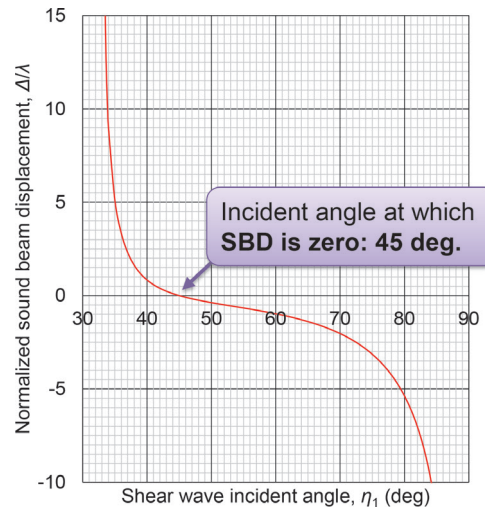
Fig. 3 Relationship between the shear-wave incident angle and normalizad sound beam displacement at the free boundary surface of an axle

lus; E is the longitudinal elastic modulus and v is Poisson's ratio.

When shear waves are incident on the spring interface with an angle of η_1, the phase shift φ of the reflected waves is obtained numerically by solving equations between stress and strain at the interface [6]. By regarding $\partial\varphi/\partial h$ in (1) as $\Delta\varphi/\Delta h$ (note: here Δ means increment), the relationship between the incident angle η_1 and the normalized sound beam displacement Δ/λ is calculated numerically by Δh and $\Delta\varphi$. Δh is derived from the equation $h = \sin\eta_1$ with the increment of $\Delta\eta_1$ at each incident angle of η_1.

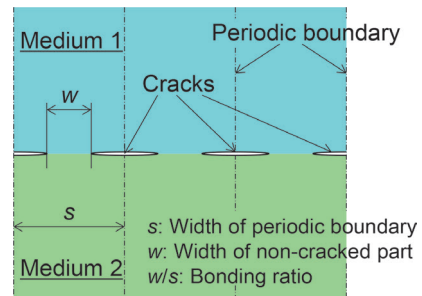**Fig. 4 Model with a periodically cracked interface equivalent to the spring interface**

As an example, Fig. 5 shows the relationship between η_1 and Δ/λ for the case where shear waves with a frequency of 2 MHz are incident on the interface with parameters of $s = 0.4$ mm and $w = 0.2$ mm, the materials of whose respective sides, medium 1 and 2, are both steel with $E = 209$ GPa and $v = 0.29$. In this case, the absolute value of sound beam displacement was smaller than that in the case of the free boundary surface shown in Fig. 3 (note the difference in the vertical axes). However, it was demonstrated theoretically that sound beam displacement also occurred at an interface where similar materials were in contact.
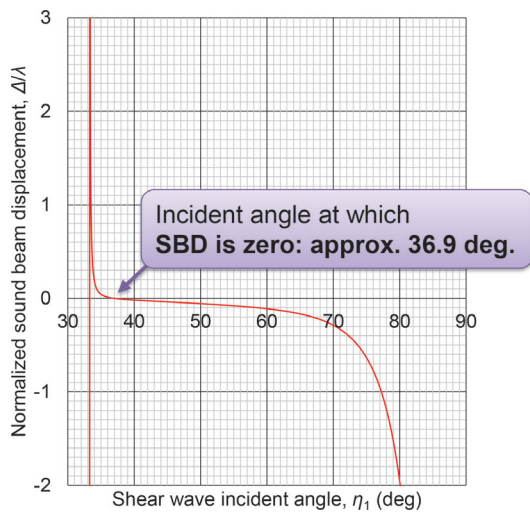
Fig. 5 Relationship between the shear-wave incident angle and normalized sound beam displacement at the axle–wheel interface
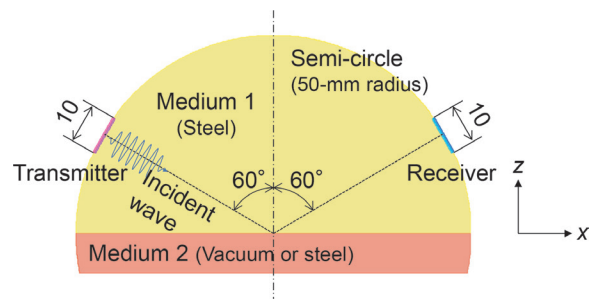

Fig. 6 Two-dimensional model for shear-wave oblique incidence with an incident angle of 60°

Table 1 Material properties of each element

Element	Material	Longitudinal wave velocity, c_L (m/s)	Shear wave velocity, c_T (m/s)	Density, ρ (kg/m^3)
Medium 1	Steel	5900	3230	7800
Medium 2	Vacuum	0	0	0
	Steel	5900	3230	7800
Probe	Acrylic resin	2730	1430	1180

3. Evaluation of sound beam displacement by ultrasound simulation

3.1 Calculation models and conditions

The reflection behavior of ultrasonic waves, when shear waves were obliquely incident on the free boundary surface of an axle and on the axle–wheel interface, was calculated by using FE models. Figure 6 shows a two-dimensional model on the x–z plane in the case of an incident angle of 60°. This model was composed of medium 1 (steel), medium 2 (vacuum or steel), and two transducers (a transmitter and a receiver). The transmitter and receiver were placed at positions that were geometrically symmetric to each other on a semi-circle of radius 50 mm, centered on the boundary surface between the two media. The length of each transducer was 10 mm. All media and transducers modeled using finite elements were composed of isotropic materials, and the material properties are shown in Table 1.

In the FE model that represented the free boundary surface of an axle (i.e., medium 2 is a vacuum), all elements were square-shaped with a side length of 0.1 mm. In the FE model that contained the axle–wheel interface (i.e., medium 2 is steel), the periodically cracked interface with parameters of s = 0.4 mm and w = 0.2 mm, which were the same values as those in section 2.3, was applied. The side length of each square element was 0.05 mm.

The incident waves were modeled as shear-vertical (SV) waves which oscillated on the x–z plane with a frequency of 2 MHz, and the displacement in the y direction (normal to the plane of the two-dimensional model) was fixed. The waveform was composed of eight waves, comprising five sinusoidal waves with two 1.5-wavelength transient waves on either side, as is shown schematically near the transmitter in Fig. 6. Since the series of calculations used were linear, the displacement amplitude can be selected arbitrarily, so it was set to 2 mm. Four cases, with incident angles of 35°, 45°, 60° and 75°, respectively, were modeled and calculated.

The time step of the calculation was approximately 13.6 ns. The ultrasonic wave propagation was calculated up to a time of 40 μs, when the reception of ultrasonic waves reflected at the interface had been completed. The ultrasound simulation software Com-WAVE Ver.9.5.2 (ITOCHU Techno-Solutions Corp.) was used to

perform the calculation.

3.2 Calculation results

Figure 7 shows the displacement amplitude distribution just before receiving reflected waves at the receiver, calculated in each case of the incident angle of 35° and 60° in a free boundary surface model. The sound beam displacement was not observed in the case of 45°. On the contrary, the sound beam displacement in the positive direction of x was observed in the case of 35°, as shown in Fig. 7(a), and the one in the negative direction of x was observed in the case of 60°, as shown in Fig. 7(b). These trends are consistent with the theoretically investigated results shown in Fig. 3. In an axle–wheel interface model, the displacement amplitude distribution also showed the sound beam displacement in all cases, except at an incident angle of 75°, the amplitude of whose reflected waves at the interface was too small to distinguish it from the component of surface waves.

Based on the displacement amplitude distribution obtained from the calculation in each FE model, the sound beam displacement was determined in 0.1 mm units, with reference to the beam centerline drawn by visual observation so as to pass through the maximum displacement amplitude point of reflected waves. Table 2 summarizes the comparison of sound beam displacement between visual observation and theoretical investigation mentioned in sections 2.2 and 2.3. Comparing the calculation results with the theoretical values, they generally agreed in the free boundary surface of an axle. On the other hand, although the theoretical values were less than 1 mm in the axle–wheel interface, the calculation results showed values in the order of several millimeters. However, the qualitative trend results agreed, in which the absolute value increases as the incident angle moves away from 45°.
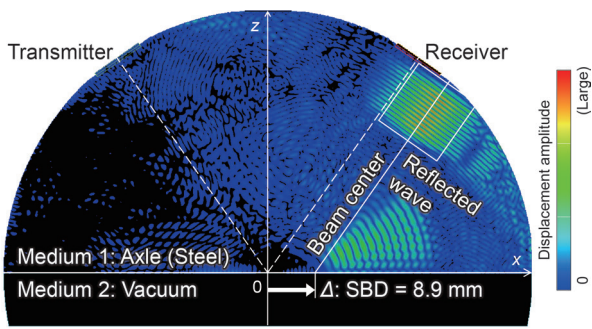
(a) Incident angle of 35°
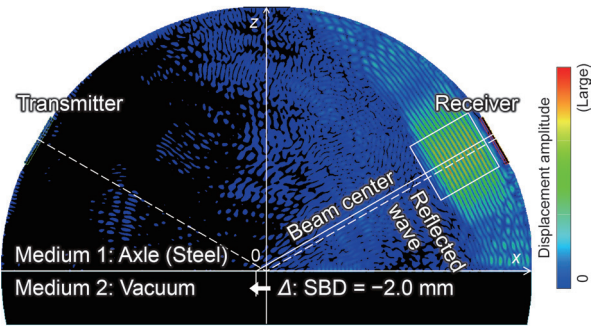
(b) Incident angle of 60°

Fig. 7 Displacement amplitude distribution just before receiving reflected waves in a free boundary surface model

Table 2 Comparison of sound beam displacement between visual observation of displacement amplitude distribution by FE calculation, and theoretical investigation

Shear-wave incident angle	Free boundary surface of axle		Axle–wheel spring interface	
	FE calc.	Theor. val.	FE calc.	Theor. val.
35°	8.9	8.3	4.2	0.07
45°	0	0	≈ 0	−0.06
60°	−2.0	−1.6	−4.2	−0.18
75°	−5.3	−5.1	(Not observed)	−1.0

(Units in millimeters)

4. Influence of sound beam displacement on axle ultrasonic flaw detection

4.1 Influence assumed for wave reflection at a flaw

When ultrasonic shear waves transmitted from a probe with an incident angle of η_1 degrees are incident on a boundary surface where a surface flaw exists as shown in Fig. 8, they first reflect at the boundary surface with a reflection angle of η_1 degrees. They are then incident on the flaw face with an incident angle of $(90 - \eta_1)$ degrees, that is, the complementary angle of η_1. After that, the waves reflect at the flaw face with a reflection angle of $(90 - \eta_1)$ degrees, and then they return to the probe to be received.

Considering a case involving the free boundary surface of an axle, when the incident angle η_1 is smaller than 45°, sound beam displacement with a positive value, Δ_1, occurs at the free boundary surface, and one with a negative value, Δ_2, occurs at the flaw face. In total, sound beam displacement with a negative value, Δ_{tot}, occurs at

the probe position. When η_1 is larger than 45°, the opposite phenomenon, that is, total sound beam displacement with a positive value, occurs at the probe position.

Therefore, the following two influences are assumed for axle ultrasonic flaw detection due to sound beam displacement. First, when a probe is positioned on a site on the axle surface which is derived geometrically from the flaw position and the probe refraction angle (i.e., the incident angle of ultrasound on the boundary surface), the arrival point of reflected ultrasonic waves shifts from the probe position. Secondly, when a probe is arranged to obtain the maximum ultrasonic echo from a flaw, the flaw position estimated from the probe position may contain some error. We evaluated the influence of sound beam displacement on axle ultrasonic flaw detection from these two viewpoints.
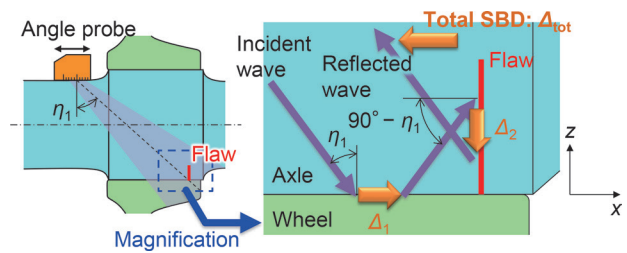
Fig. 8 Influence of sound beam displacement on ultrasonic inspection of a surface flaw

4.2 Calculation models and conditions

The transmission and reception of ultrasonic waves with an angle probe, in which shear waves were obliquely incident on an axle body and a wheel seat, were calculated by using an FE model. Figure 9 shows a two-dimensional model on the x–z plane in the case of a probe refraction angle of 55°. The thickness of the axle, corresponding to the diameter or the wall thickness of an axle, was set to 40 mm due to time constraints calculating various cases. The probe had a single transducer, with a length of 10 mm, which was used for both transmission and reception. A flaw with a height of 3 mm was placed on the axle surface. A gap of one-element width was set between the opposite flaw faces. The probe refraction angle was changed among five cases of 35°, 40°, 45°, 50° and 55°. Changes in the probe position, and in the model length in the x direction were also introduced to respective cases. All the media and probe, composing the finite elements, were made from isotropic materials, and the material properties shown in Table 1, identical to those mentioned in chapter 3, were used in this calculation.
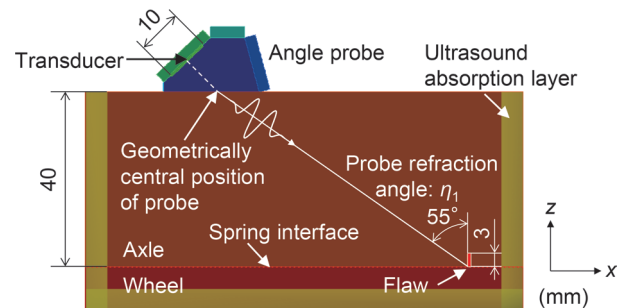

Fig. 9 Two-dimensional model calculating the influence of sound beam displacement on wheel-seat flaw detection with a probe refraction angle of 55°

In the FE model, all elements were square-shaped, with a side length of 0.1 mm. In addition, in the axle–wheel interface model, a periodically cracked interface was selected, with parameters of $s = 1$ mm and $w = 0.7$ mm. These parameters were based on a value of the normal stiffness K_N corresponding to the contact pressure due to the interference-to-diameter ratio between an axle and a wheel, and based on the periodic surface condition due to the move of a tool per one rotation in the machining process.

The incident waves were modeled as shear-vertical (SV) waves which oscillated on the x–z plane with a frequency of 2 MHz, and the displacement in the y direction was fixed. The waveform was a wavelet with three waves as is shown schematically near the probe in Fig. 9. The displacement amplitude was set to 2 mm. In each model with different interface or refraction angle, the origin of the probe was set to the position derived geometrically from the flaw position and the probe refraction angle, which is referred to as the geometrically central position in the following. The probe was moved along the axle surface with a pitch of 1 mm in the x direction. The received echo height, which was defined by the average volume strain among all elements composing the transducer in the probe, was calculated for each probe position. The maximum echo height and the probe position maximizing the echo height were obtained by approximating the data with a polynomial function, in a probe position vs. echo height graph (refer to Fig. 11 below).

The time step of the calculation was approximately 13.6 ns. The ultrasonic wave propagation was calculated up to a time of 45–65 μs, according to the path length determined by the refraction angle of the probe. The ultrasound simulation software ComWAVE was used for all the calculations. Similar calculations were performed for the incident waves with a frequency of 5 MHz, the details of those calculation conditions are omitted here.

4.3 Theoretical value of sound beam displacement for reflection at a flaw

Using the sound beam displacement Δ_1 due to the probe refraction angle of η_1 degrees, and Δ_2 due to its complementary angle of $(90 - \eta_1)$ degrees, as shown in Fig. 8, the total sound beam displacement at the probe, Δ_{tot}, is obtained by the following equation:

$$\Delta_{tot} = -\Delta_1 + \Delta_2 \tan \eta_1 \tag{4}$$

Opposite flaw faces may be in contact with each other in the case of actual axle flaws. However, the flaw faces which cause the displacement of Δ_2 were treated as a free surface of steel in this estimation.

Table 3 shows theoretical values of total sound beam displacement Δ_{tot}, calculated by the normalized sound beam displacement Δ/λ shown in Fig. 3 or 5 and (4), for the cases of the refraction angle η_1 from 35° to 55° with a frequency of 2 MHz, both in an axle body and in a wheel seat. It indicates that Δ_{tot} is larger in the case of the axle body than in that of the wheel seat. However, some of the theoretical values of sound beam displacement at the flaw face, Δ_2, were larger than the flaw height of 3 mm modeled in the FE calculation. It is unlikely that sound beam displacement exceeding the height of a flaw occurs on a flaw face. Therefore, it is estimated that the actual total sound beam displacement Δ_{tot} would be smaller than the theoretical values in this table.

In the cases with a frequency of 5 MHz, the wavelength λ, smaller than 2 MHz, accordingly yields smaller total sound beam displacement Δ_{tot}, calculated by the normalized sound beam displacement Δ/λ, than those shown in Table 3.

Table 3　Theoretical values of total sound beam displacement for the cases of respective refraction angles with a frequency of 2 MHz, both in an axle body and in a wheel seat

Axle part	Refraction angle, η_1 (deg.)	Sound beam displacement at interface, Δ_1 (mm)	Sound beam displacement at flaw face, Δ_2 (mm)	Total sound beam displacement, Δ_{tot} (mm)
Axle body	35	8.3	−1.1	−9.0
	40	1.4	−0.6	−1.9
	45	0	0	0
	50	−0.6	1.4	2.2
	55	−1.1	8.3	12.9
Wheel seat	35	0.04	−1.1	−0.8
	40	−0.03	−0.6	−0.5
	45	−0.05	0	0.05
	50	−0.08	1.4	1.7
	55	−0.11	8.3	11.9

4.4 Probe position achieving maximum echo height

In each model of an axle body and a wheel seat, the relationship between the probe shift from the geometrically central position and the echo height was calculated for five cases of refraction angles from 35° to 55° with a frequency of 2 MHz. As an example, Fig. 10 shows the propagation behavior of ultrasonic waves when a flaw in an axle body was detected at a refraction angle of 55°. When the probe was placed at the geometrically central position, the reflected waves at the flaw shifted forward, approximately 8 mm in the positive direction of x. At this time, when the probe position was moved forward by 4 mm, the height of the received flaw echo reached a maximum.

In this manner, the relationship between the probe shift from the geometrically central position and the echo height was obtained in each case of refraction angles using the FE calculation as shown in Fig. 11. The findings indicate that the overall echo height was higher in the case of a refraction angle of 40° or 45°, and that the probe position achieving the maximum echo height changed in the positive direction according to increase in the refraction angle.

Figure 12 summarizes the maximum echo height and the probe position achieving it, along with change of the refraction angle of the probe, based on the data for (a) an axle body and (b) a wheel seat shown in Fig. 11. The graph indicating the probe position in Fig. 12 also shows the theoretical values of total sound beam displacement Δ_{tot} shown in Table 3. The maximum echo height changed relatively gradually along with change of the refraction angle except in the vicinity of 45° of the wheel seat. The probe position maximizing the echo height shifted forward against the geometrically central position with increase in the refraction angle. The probe shift was greater in the case of an axle body than a wheel seat. The case of a refraction angle of 35° in an axle body showed the maximum probe shift of 8 mm in absolute value.

According to Fig. 12, the probe position maximizing the echo height by the FE calculation coincided qualitatively with the theoretical values of total sound beam displacement Δ_{tot}, along with change of the refraction angle of the probe. However, the results at the angle of 55° in the case of an axle body and those in the case of a wheel seat exhibit quantitative differences between FE calculation values and theoretical values of Δ_{tot}. Causes for those differences may be attributed to the following: (i) no consideration of the probe shift in the calculation of total sound beam displacement Δ_{tot}, (ii) the

(a) Just after incidence to an axle

(b) At the time of reflection at a flaw
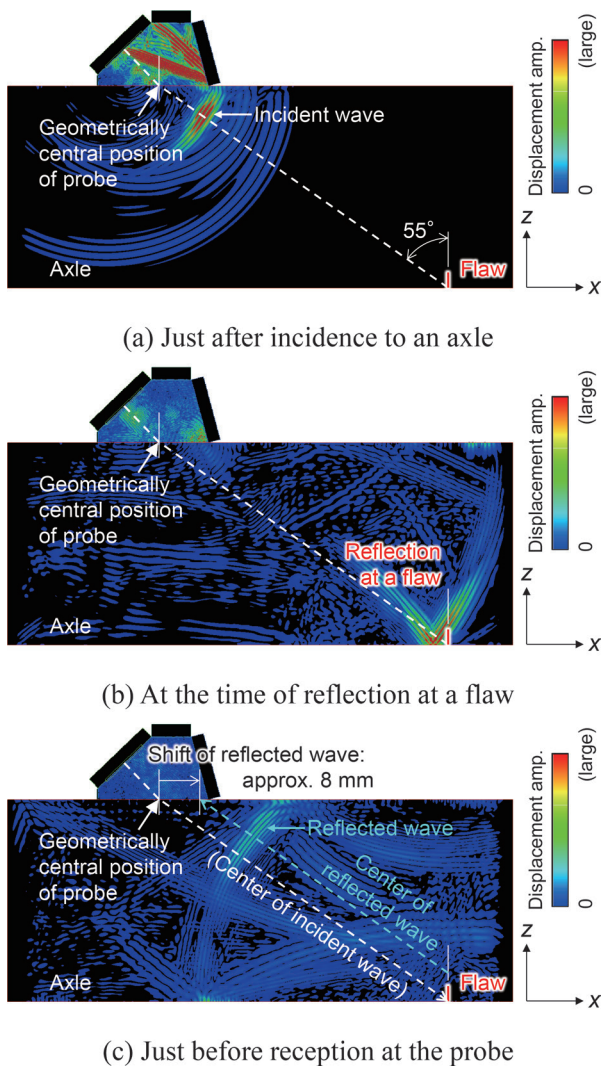

(c) Just before reception at the probe

Fig. 10 Ultrasound propagation when a probe with a refraction angle of 55° was placed at the geometrically central position in an axle body

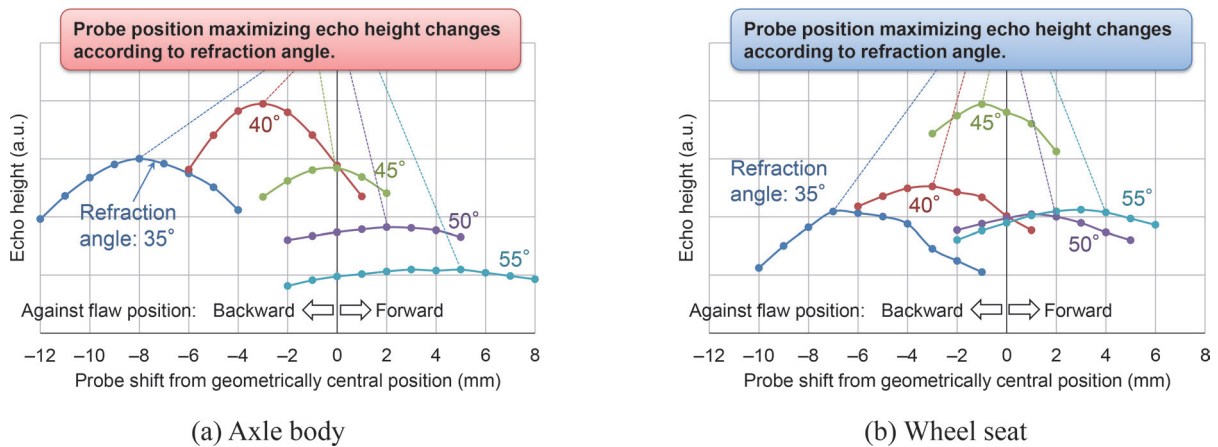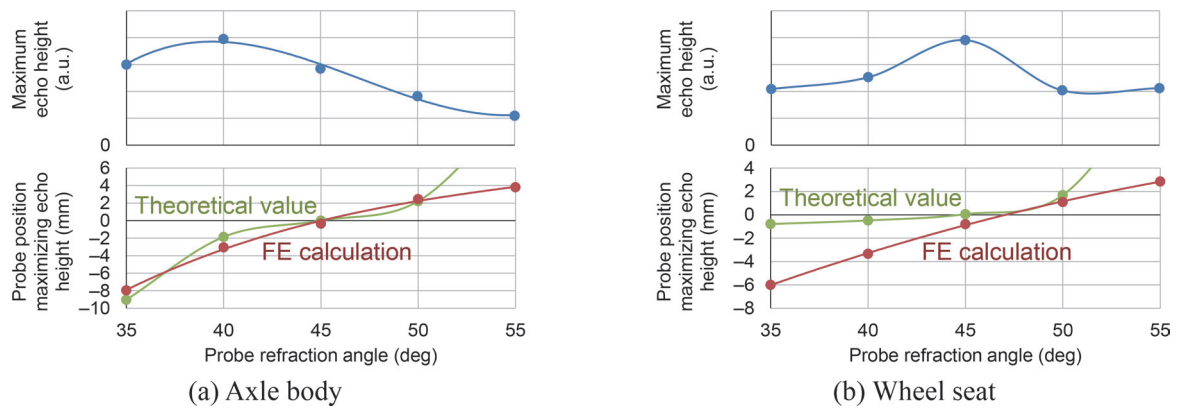flaw height of 3 mm limiting the amount of the sound beam displacement Δ_2, (iii) the sound beam displacement occurring at the incidence on an axle from a probe, which falls beyond the scope of this study, and (iv) inaccurate modelling at the axle–wheel interface.

Similar FE calculations were performed for the cases with a frequency of 5 MHz. There results showed that the probe position maximizing the echo height was around −3 to +1 mm in an axle body and −2 to +0 mm in a wheel seat along with change of the refraction angle. These results were not as remarkable as those for the frequency of 2 MHz shown in Fig. 12. However, the sound beam displacement also showed a certain influence on the results for the 5 MHz frequency.

5. Conclusions

In this study, we evaluated the influence of the shift of reflection points at the time of ultrasound reflections, that is, sound beam displacement, on the ultrasonic flaw detection of axles, targeting two types of boundary surface, that is, the free boundary surface of an axle (an axle body) and the axle–wheel interface (a wheel seat) by means of theoretical calculations and FE calculations. The obtained results are as follows:

1) We introduced the relationship between the incident angle of shear waves and sound beam displacement, for both free boundary surfaces in axle bodies and the axle–wheel spring interface corresponding to the fitting of a wheel in a wheel seat. The FE calculation showed the occurrence of sound beam displacement in fitted parts.

2) The influence of sound beam displacement on the echo height of a flaw on an axle surface was evaluated. The probe position achieving the maximum flaw echo height shifted from the geometrical position determined by the flaw position and the refraction angle. The maximum shift reached approximately 8 mm for flaw detection in axle bodies with a frequency of 2 MHz.

It is important in axle ultrasonic flaw detection to note that the reflection points of ultrasonic waves and their receiving positions deviate due to sound beam displacement on reflection surfaces and flaw faces. In the future, confirming the applicability and consistency of sound beam displacement to experimental data in ultrasonic flaw detection of axles, we will use it for the accurate evaluation of flaw positions when a flaw is detected during actual ultrasonic flaw detection.

(a) Axle body

(b) Wheel seat

Fig. 11 Relationship between probe shifting from the geometrically central position and echo height with a frequency of 2 MHz using the FE calculation

(a) Axle body   (b) Wheel seat

Fig. 12 The maximum echo height and the probe position achieving it along with change of the refraction angle of the probe with a frequency of 2 MHz

References

[1] Artmann, K., "Berechnung der Seitenversetzung des totalreflek-tierten Strahles," *Ann. Physik.*, 437, pp. 87–102, 1948.

[2] Niklas, L., "Gruppenlaufzeit und Bündelversetzung bei der Schrägreflexion Auswirkungen auf die Praktische Werkstoff-prüfung mit Ultraschall," *Materialprüf.*, 7(8), pp. 281–288, 1965.

[3] Fukuhara, H. and Saito, T., "Numerical calculation of the shift of probe index of ultrasonic angle probes," *NDT Int.*, 23(5), pp. 276–282, 1990.

[4] Drinkwater, B.W., Dwyer-Joyce, R.S. and Cawley, P., "A study of the interaction between ultrasound and a partially contacting solid–solid interface," *Proc. R. Soc. Lond.*, A 452, pp. 2613–2628, 1996.

[5] Makino, K. and Sakamoto, H., "Quantitative evaluation of the flaw echo of railway axles in consideration of contact pressure with a wheel," *QR of RTRI*, Vol. 55, No. 3, pp. 144–151, 2014.

[6] Makino, K. and Biwa, S., "Influence of axle–wheel interface on ultrasonic testing of fatigue cracks in wheelset," *Ultrasonics*, 53, pp. 239–248, 2013.

[7] Baik, J.-M. and Thompson, R.B., "Ultrasonic scattering from imperfect interfaces: A quasi-static model," *J. Nondestr. Eval.*, 4, pp. 177–196, 1984.

Author

Kazunari MAKINO, Ph.D. (Eng.)
Senior Researcher, Vehicle & Bogie Parts Strength Laboratory, Vehicle Technology Division
Research Areas: Nondestructive Testing of Bogie Parts, Axle Strength

Verification of Reduction Effect of Vertical Vibration of Car-body by High-damping Elastic Support of Under-floor Equipment

Ken-ichiro AIDA   **Tadao TAKIGAMI**
Vehicle Noise and Vibration Laboratory, Vehicle Technology Division

Yuki AKIYAMA
Vehicle Noise and Vibration Laboratory, Vehicle Structure Technology Division (Former)

We are developing high-damping elastic support of under-floor equipment as one method for reducing vertical car-body vibrations. In this study, two types of excitation test were performed using an actual vehicle. Firstly, we conducted excitation tests in the rolling stock testing plant to verify the effect of the elastically supported mass on the reduction of the elastic vibration of car-body. Secondly, to examine the vibration isolation performance of the developed rubber mount, we conducted stationary excitation tests using a vibration exciter.

1. Introduction

We have been studying high-damping elastic support for under-floor equipment as one method for reducing vertical car-body vibrations to improve ride comfort [1, 2]. The proposed method utilizes under-floor equipment as a kind of dynamic vibration absorber (DVA) inspired by the damping effect and the multimodal vibration reduction effect of passengers on railway vehicles [3]. Our proposed method is characterized by the support of under-floor equipment with high-damping material which has a natural frequency slightly lower than that of the target mode of the car-body elastic vibration. So far, we developed elastic mounting devices for actual railway vehicles owned by Railway Technical Research Institute (RTRI) and confirmed that multiple modes of car-body elastic vibration were simultaneously reduced by applying the developed elastic mounting devices [1, 2].

Recently, there have been many studies on methods for reducing elastic vibration of car-bodies using under-floor equipment as a DVA [e.g., 4, 5, 6]. However, there are few experimental studies on verifying the reduction of elastic vibration of car-bodies using under-floor equipment as a DVA when applied to an actual vehicle. This paper investigated the effect of the mass of under-floor equipment on the reduction of the elastic vibration of car-bodies in an experimental study using an actual vehicle [7]. In our previous paper [2], the mass of the under-floor equipment was about 3400 kg, assuming the mass of a main transformer, whereas in this paper we targeted a smaller mass which was less than about 1000 kg. To verify the reduction effect on elastic vibration of car-bodies, we conducted excitation tests using a test vehicle by applying an elastic mounting device in a rolling stock testing plant. Moreover, some under-floor equipment, such as air compressors or traction transformers, and so on, generates its own vibrations [8]. When such vibrations are transmitted to the car-body, they may increase car-body vibration. The isolation effect of the vibration generated by under-floor equipment itself can be expected by introducing elastic mounting devices. To check the vibration isolation performance of the developed mounting device, we also conducted stationary excitation tests with a vibration exciter.

2. Verification of car-body vibration induced by track irregularity

To investigate the effect of under-floor equipment mass on the reduction of elastic car-body vibration induced by track irregularity, we conducted excitation tests on the rolling stock testing plant in RTRI [9] using a Shinkansen (bullet train) type test vehicle shown in Fig. 1.

2.1 Setup of under-floor equipment

Figure 2 shows the under-floor equipment which was attached to the car-body in this study. Four pieces of under-floor equipment were built and installed under the test vehicle as shown in Fig. 2(a). The under-floor equipment consisted of a framework, a stack of thick steel plates as dummy mass and supporting members, as shown in Fig. 2(b). The steel plates were supported by four supporting members. Two support conditions were employed for the steel plates: rigid support (fixed normally, using bolts) and elastic support with high-damping material. We used rubber mounts made of butyl rubber, developed in our previous study [2], as the elastic supporting device, as shown in Fig. 2(c). The measured loss factor of the rubber mount was 0.29. The spring constant of the rubber mount was designed so that the natural frequency of the under-floor equipment was slightly lower than the natural frequency of the car-body to be targeted.
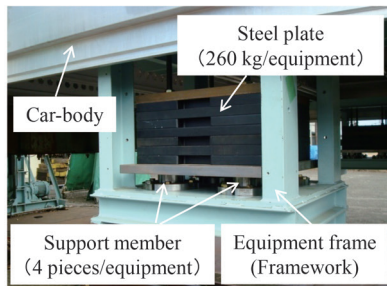
The weight of steel plates was 260 kg. Since the mass of the car-body was approximately 26 tons, the mass ratio of the steel

Fig. 1   The Shinkansen type test vehicle
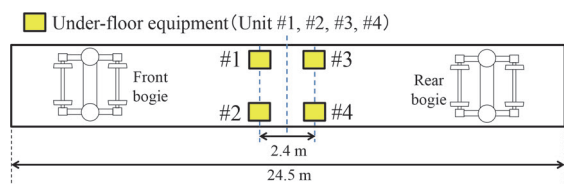
(a)   Layout of under-floor equipment

(b)   Under-floor equipment

(c)   Rubber mount (elastic supporting device)

Fig. 2   Setup of the under-floor equipment on test vehicle

Table 1   Supporting and mass conditions of under-floor equipment

Case	Support condition of mass				Elastically supported mass m_e
	Unit #1	Unit #2	Unit #3	Unit #4	
Case(a) Rigid support	Rigid	Rigid	Rigid	Rigid	(0 kg)
Case(b) Elastic support	Rigid	Elastic	Rigid	Rigid	260 kg
Case(c) Elastic support	Elastic	Elastic	Rigid	Rigid	520 kg
Case(d) Elastic support	Elastic	Elastic	Elastic	Rigid	780 kg
Case(e) Elastic support	Elastic	Elastic	Elastic	Elastic	1040 kg
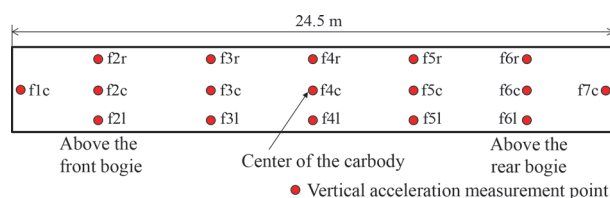
Fig. 3   Acceleration measurement points on floor

(i) 8.9 Hz (D-mode)   (ii) 10.9 Hz (B-mode)
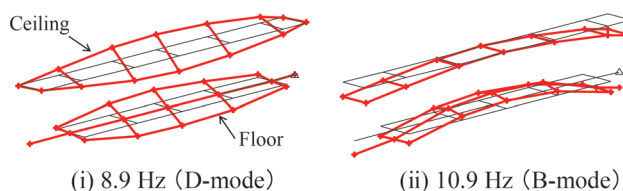
Fig. 4   Mode shapes and natural frequencies of the test vehicle

plates per under-floor equipment versus the car-body was about 1%, therefore the mass ratio of the steel plates in the four pieces of under-floor equipment versus the car-body was about 4%. Table 1 shows the supporting conditions of the equipment. We implemented five cases: rigid support in four pieces of under-floor equipment (Case(a)) and elastic support with four different support conditions (Case(b)(c)(d)(e)). We set the elastically supported masses (m_e) to 260, 520, 780 and 1040 kg.

2.2 Experimental modal analysis

We carried out an experimental modal analysis to check the elastic modes of the car-body when the under-floor equipment was loaded (Case(a)). All four wheelsets of the vehicle were excited at the same time without a time delay between the wheelsets. Figure 3 shows the measurement points of vertical acceleration on the floor. In addition, vertical accelerations on the ceiling at 14 points were also measured.

Figure 4 shows the identified vibration modes around 10 Hz. D-mode is an asymmetric diamond-shaped mode (diagonal distortion mode) at 8.9 Hz, and B-mode is the first bending mode of a freely supported elastic beam at 10.9 Hz. It is known that these modes have a large influence on ride comfort. This paper aimed to reduce these two modes simultaneously by applying the proposed method.

2.3 Excitation conditions

To investigate the effect of the proposed method on the reduction of vertical vibration of car-bodies by track irregularity, simulated running excitation tests that simulate running conditions on a certain track were conducted. The excitation signal was decided to reproduce acceleration measured on both sides of the axle boxes of a wheelset while running on a commercial line. All wheelsets were excited with respective time delays between each axle depending on the assumed running speed. In this study, the assumed running speeds were set to 240 km/h and 320 km/h. Vertical accelerations of the floor shown in Fig. 3 were measured.

2.4 Excitation test results

2.4.1 Acceleration power spectral density

Figure 5 shows acceleration power spectral densities (hereinafter referred to as "PSD") measured at f2c (above the bogie), f4c (the center of the car-body), and f4r (longitudinal center of the floor near the window) for simulated running excitation at a speed of 240 km/h.

Each PSD in Fig. 5 displays a prominent peak around 10.7 Hz. The peak around 10.7 Hz corresponds to the B-mode shown in Fig. 4. Compared to this peak value of the rigid support case (Case(a)), it was found that the peak values were lower in the elastic support cases (Case(b)(c)(d)(e)). The fall in the peak value around 10.7 Hz was small when m_e was small, as in Case(b), while the peak values fell significantly as m_e increased.

Focusing on Fig. 5(c), two dominant peaks around 10 Hz were
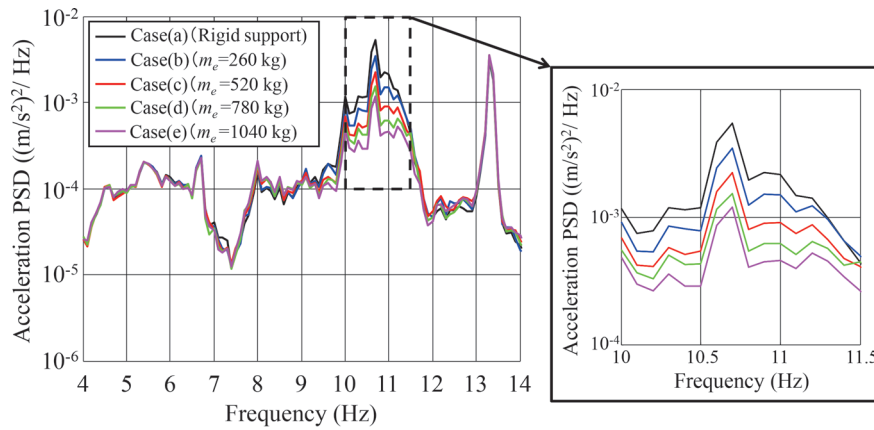
(a) At measurement point f2c
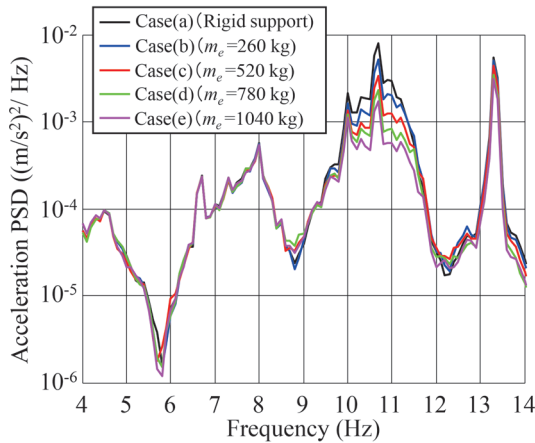
(b) At measurement point f4c
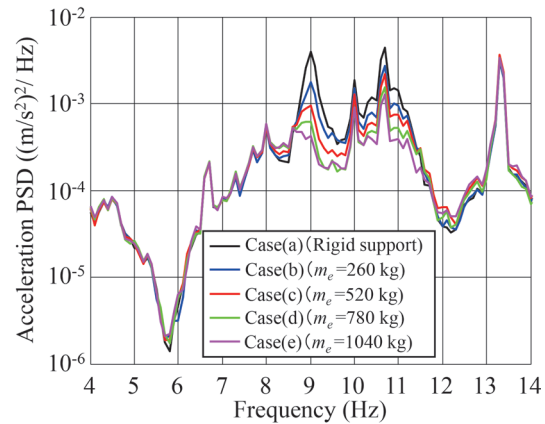
(c) At measurement point f4r

Fig. 5 Acceleration PSDs (simulated running excitation corresponding to 240 km/h)

observed. The peak around 9.0 Hz corresponds to the D-mode shown in Fig. 4. It was found that both peak values around 9.0 Hz and 10.7 Hz were lower in the elastic support cases (Case(b)(c)(d) (e)) and the reduction effect grew as m_e increased.

These results confirm that a simultaneous vibration suppression effect for the two elastic vibration modes can be expected, even when the elastically supported mass of the under-floor equipment is not very large, when using the proposed method. However, these results also confirm that a large elastically supported mass of under-floor equipment is needed to achieve a large vibration reduction effect.

2.4.2 Ride quality level

We evaluated the ride comfort using the ride quality level (L_T) which is widely used in Japan [10]. We calculated L_T from the vertical acceleration measured on the floor under simulated running excitation at 240 km/h and 320 km/h.

Figure 6 shows the difference between the L_T values (hereinafter, ΔL_T) in each elastic support case (Cases (b)(c)(d)(e)) and the rigid support case (Case(a)) at f4c and f4r. A negative ΔL_T value means that the ride comfort improved with elastic support. It is reported that a difference of 3 dB in L_T can be perceived by passengers [11]. Figure 6 shows that L_T decreased even when m_e was 260 kg (Case(b)). However, the larger the elastically supported mass was, the greater the fall in L_T. Focusing on point f4c, L_T fell by 1 dB or

less in Case(b) (mass ratio of me versus car-body about 1%), whereas L_T fell by more than 3 dB in Case(e) (mass ratio of m_e versus car-body about 4%).

Figure 7 shows the ΔL_T between the elastic support of m_e = 1040 kg (Case(e)) and the rigid support (Case(a)) at 17 measurement points on the floor in Fig. 3. Figure 7 shows that L_T fell at all measurement points in the elastic support case. The largest decrease in L_T was in the center of the car-body (point f4c), which is near the position where the elastically supported under-floor equipment was installed, whereas a reduction in L_T was also observed above the bogies and at the ends of the car-body. It was found that L_T fell across the whole of the floor of the car-body with elastic support.

These results from the two different excitation signal conditions confirm that the improvement of ride comfort grows as the elastically supported mass of under-floor equipment increases when using the proposed method. To reduce the elastic vibration of car-bodies effectively by utilizing the under-floor equipment, we think that the under-floor equipment should be located near the center of the car-body (anti-node position of the D-mode and B-mode) and that the under-floor equipment should be supported elastically with high-damping material having a natural frequency slightly lower than that of target mode of the car-body elastic vibration. Moreover, the mass of the equipment with elastic support should be large.
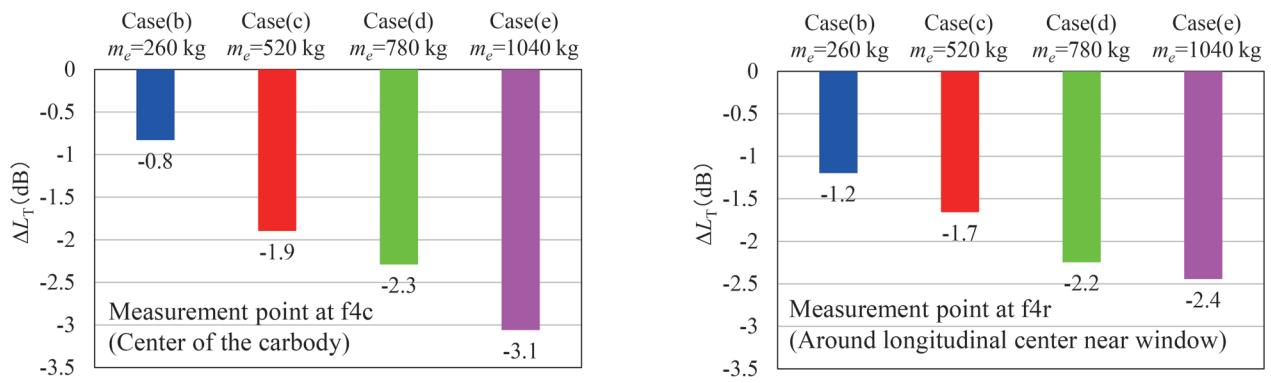
(a) Simulated running excitation corresponding to 240 km/h
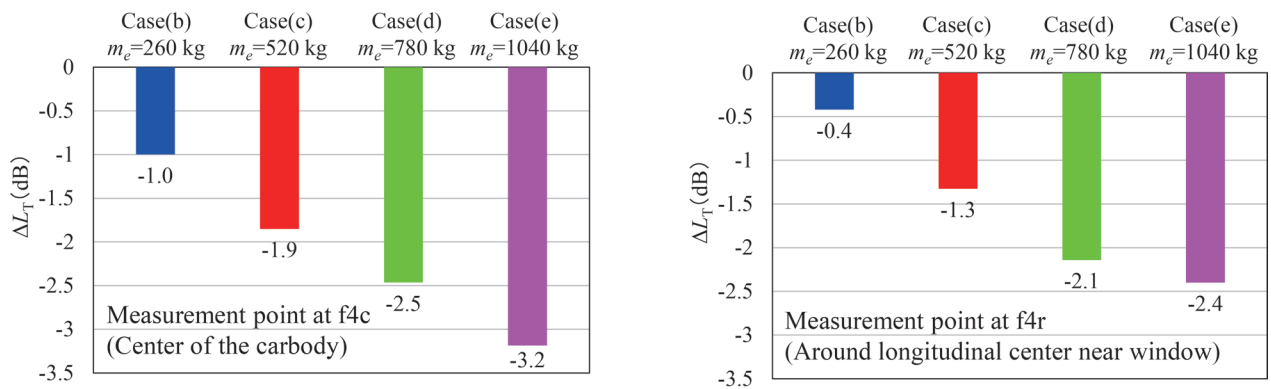
(b) Simulated running excitation corresponding to 320 km/h

Fig. 6   Change in ride quality level with different elastically supported masses

	f1	f2	f3	f4	f5	f6	f7	
r		-0.9	-0.7	-2.4	-0.6	-1.0		r
c	-2.0	-1.7	-1.2	-3.1	-0.3	-1.6	-1.8	c
l		-1.0	-0.9	-2.6	-0.8	-0.8		l

	Above the front bogie		Center of the carbody		Above the rear bogie	

$\triangle L_T$ (dB)

| 0 |
| -1.0 |
| -2.0 |
| -3.0 |

(a) Simulated running excitation corresponding to 240 km/h

	f1	f2	f3	f4	f5	f6	f7	
r		-1.9	-0.5	-2.4	-0.6	-1.7		r
c	-2.2	-2.2	-1.3	-3.2	-0.9	-1.7	-2.0	c
l		-2.0	-0.7	-2.3	-0.6	-1.6		l

	Above the front bogie		Center of the carbody		Above the rear bogie	

$\triangle L_T$ (dB)

| 0 |
| -1.0 |
| -2.0 |
| -3.0 |

(b) Simulated running excitation corresponding to 320 km/h

Fig. 7   Change in ride quality level for all measurement points on floor in Case(e)

3. Verification of vibration isolation effect induced by under-floor equipment excitation

We conducted stationary excitation tests to check the vibration isolation of the developed elastic mounts against vibrations induced by the under-floor equipment. In this test, the test vehicle shown in Fig. 1 was stationary on rails and excited using an exciter.

3.1 Setup of the stationary excitation test

Figure 8 shows the set-up of the excitation test. Steel plates on the support members shown in Fig. 2(b) were removed from the #2 under-floor equipment, and the exciter was installed in its place to simulate vibrations from the equipment. Two support conditions were employed for the exciter: rigid support (fixed normally, using bolts) and elastic support with rubber mounts. The car-body was

excited vertically using the exciter and the vertical acceleration of the equipment frame and the floor of the car-body were measured.

3.2 Excitation conditions

Two different conditions were employed in the stationary excitation tests: sinusoidal excitation and random excitation. An excitation signal with a constant frequency of 58 Hz was used in sinusoidal excitation. The value of 58 Hz was determined by taking an example of the rotating frequency of cooling fans of ventilating equipment in commercial vehicles. A band-limited random signal with a uniform frequency component in the range of 40-200 Hz was used for the random excitation.
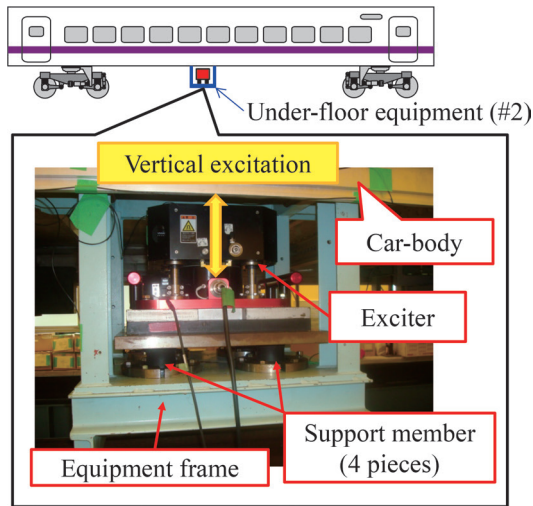
Fig. 8   Setup of stationary excitation test using an exciter
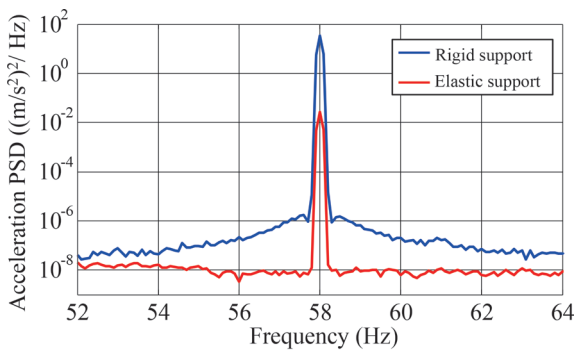
(a) Equipment frame (near support members)
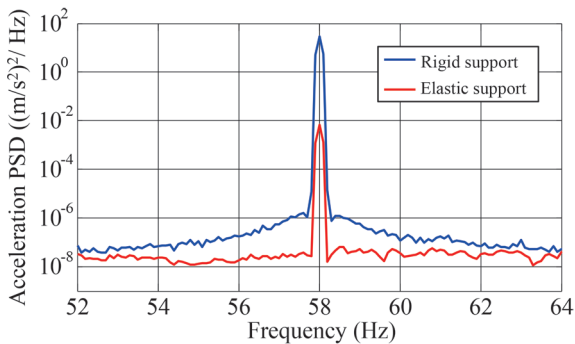
(b) Floor (point f4c shown in Fig. 3)

Fig. 9   Acceleration PSDs (sinusoidal excitation)

3.3 Excitation test results

3.3.1 Sinusoidal excitation

Figure 9 shows the acceleration PSDs measured on the equipment frame near the support members and the floor at the center of the car-body (point f4c shown in Fig. 3) under sinusoidal excitation. Results confirmed that the elastic support with rubber mounts reduces the peak values of the excitation frequency in the PSD of both the equipment frame and the floor of the car-body.

3.3.2 Random excitation

Figure 10 shows the acceleration PSDs measured on the equipment frame near the support members and the floor at the center of the car-body (point f4c shown in Fig. 3) under random excitation. It was found that the acceleration PSDs values decreased over a wide frequency range with the elastic support on rubber mounts. Since vertical vibrations fell not only in the equipment frame but also on the floor of the car-body, vibration isolation performance of the developed rubber mount against vibration transmitted from the under-floor equipment to the car-body was verified with an actual railway vehicle.

4. Summary

This paper presented a method to reduce the elastic vibration of car-body by supporting under-floor equipment with high-damping elastic mounts.
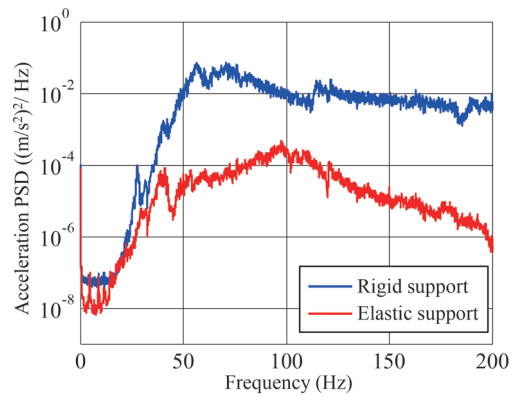
(a) Equipment frame (near support members)
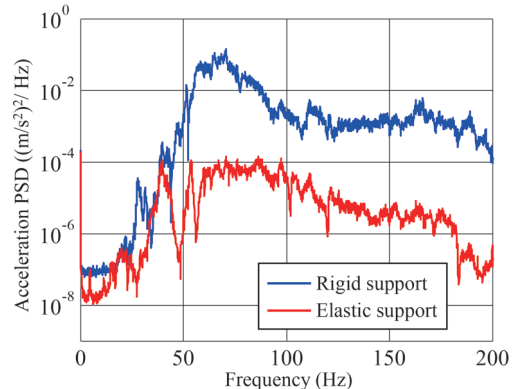
(b) Floor (point f4c shown in Fig. 3)

Fig. 10   Acceleration PSDs (random excitation)

We conducted excitation tests in the rolling stock testing plant to examine the effect of this method on reducing car-body vibrations induced by track irregularity. As a result, two dominant peaks in the acceleration power spectrum densities of the floor corresponding to elastic vibration modes were reduced simultaneously when the developed rubber mounts were used. The improvement of ride comfort grew as the elastically supported mass of under-floor increased.

To examine the vibration isolation performance of the developed rubber mount, excitation tests were performed with a vibration exciter installed on the under-floor equipment. The sinusoidal excitation tests demonstrated that the developed rubber mounts reduce the peak value in the acceleration power spectrum density of the car-body floor corresponding to the excitation frequency. From the random excitation test, we confirmed that vertical vibration of the car-body floor was reduced over a wide frequency band.

These results confirm that the proposed method can reduce vertical car-body vibrations induced not only by track irregularities but also by under-floor equipment vibration.

References

[1] Tomioka, T. et al., "Reduction of Carbody Flexural Vibration by High-Damping Elastic Support of Equipment," *Proceedings of the Second International Conference on Railway Technology*: *Research*, *Development and Maintenance* (*Railways 2014*), Paper No. 9, 2014.

[2] Aida, K. et al., "Reduction of Carbody Flexural Vibration by the High-damping Elastic Support of Under-floor Equipment," *Quarterly Report of RTRI*, Vol. 56, No. 4, pp. 262-267, 2015.

[3] Tomioka, T. and Takigami, T., "Experimental and numerical study on the effect due to passengers on flexural vibrations in railway vehicle carbodies," *Journal of Sound and Vibration*, Vol. 343, pp. 1–19, 2015.

[4] Gong, D. et al., "Method of multi-mode vibration control for the carbody of high-speed electric multiple unit trains," *Journal of Sound and Vibration*, Vol. 409, pp. 94-111, 2017.

[5] Huang, C. et al., "Numerical and experimental studies on the car body flexible vibration reduction due to the effect of car body-mounted equipment," *Proceedings of the Institution of Mechanical Engineers*, *Part F*: *Journal of Rail and Rapid Transit*, Vol. 232, Issue 1, pp. 103-120, 2018.

[6] Dumitriu, M., "Numerical study of the influence of suspended equipment on ride comfort in high-speed railway vehicles," *Scientia Iranica Transactions B*: *Mechanical Engineering*, Vol. 27, Issue 4, pp. 1897-1915, 2020.

[7] Aida, K. et al., "Reduction of vertical vibration of railway vehicle with high-damping elastic support of underfloor equipment," *Transactions of the Japan Society of Mechanical Engineers*, Vol. 87, No. 902, 2021 (in Japanese).

[8] Wang, Q. et al., "Carbody vibrations of high-speed train caused by dynamic unbalance of underframe suspended equipment," *Advances in Mechanical Engineering*, Vol. 10, Issue 12, 2018.

[9] Miyamoto, M., "JR Rolling Stock Testing Plant Capable of Testing at a Speed of 500 km/h," *Quarterly Report of RTRI*, Vol. 32, No. 4, pp. 211-212, 1991.

[10] Suzuki, H., "Research trends on riding comfort evaluation in Japan," *Proceedings of the Institution of Mechanical Engineers*, *Part F*: *Journal of Rail and Rapid Transit*, Vol. 212, Issue 1, pp. 61-72, 1998.

[11] Yamazaki, K. et al., "A study on the evaluation of ride comfort," *Bulletin of Railway Labor Science Research Institute*, Vol. 36, pp. 57-73, 1982 (in Japanese).

Authors

Ken-ichiro AIDA
Senior Researcher, Vehicle Noise and Vibration Laboratory, Vehicle Technology Division
Research Areas: Carbody Structure, Ride Comfort Evaluation

Yuki AKIYAMA, Dr. Eng.
Assistant Senior Researcher, Vehicle Noise and Vibration Laboratory, Vehicle Structure Technology Division (Former)
Research Areas: Carbody Vibration of Control, Vibration Analysis, Ride Comfort Evaluation

Tadao TAKIGAMI, Dr. Eng.
Senior Chief Researcher, Vehicle Noise and Vibration Laboratory, Vehicle Technology Division
Research Areas: Flexural Vibration of Carbody, Vibration Analysis, Ride Comfort Evaluation

Thermal Deformation Analysis for Gas Pressure Welding of Rail

Hajime ITOH   **Ryu-ichi YAMAMOTO**

Rail Maintenance Laboratory, Track Technology Division

We developed a thermal deformation analysis model using numerical calculation in order to quantitatively understand the deformation behavior of rail gas pressure welding. We found that the degree of deformation at the center of the rail base and the jaw part of the rail head are smaller to that of other parts. Furthermore, we also identified that hot cracks occur in these parts in crack simulation tests. This paper describes the developed thermal deformation analysis model for rail gas pressure welding and presents test results validating this method.

Key words: *gas pressure welding, numerical analysis, deformation*

1. Introduction

Gas pressure welding (GPW) is the main rail welding method used in Japan for the production of continuous welded rails (CWR) because of the high reliability and relatively small size of device required for this kind of welding. GPW accounts for 40% of total rail welding in the Japan Railways Group [1].

The welding principle is to promote refinement of oxide inclusions by increasing the temperature and plastic deformation of the weld interface due to heating with an oxy-acetylene flame and axial pressing.

In this method, although a bulge is formed due to plastic deformation, it is trimmed with a special blade just after the heating process to reduce the amount of finishing work.

Weld failures in gas pressure welds are extremely rare in Japan, because gas pressure welds executed under standard conditions are highly reliable, and all welds are inspected by non-destructive method immediately after welding [2]. However, as shown in Fig. 1, rare cracking does occur at the low-strength weld interface which contains oxide inclusions, because the bonding strength of the weld interface is not able to withstand the tensile stress in the trimming process [3]. These cracks are referred to as "trimming cracks" below.
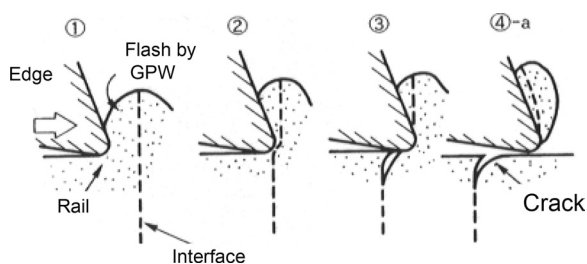
Fig. 1   Schematic illustrations of trimming cracks

Figure 2 shows an example of trimming cracks in the rail gas pressure weld. Trimming cracks often show a black fracture surface covered with a high-temperature oxide film, as shown in Fig. 2, since the weld interface breaks at high temperature.

Trimming cracks tend to occur at the corners and the bottom of rails. If they occur under the jaw of a rail head or in the center of a rail bottom, they are likely to be missed by a magnetic particle inspection conducted just after welding, and may lead to rail failure.

In order to prevent trimming cracks, improvements in the heating burner [4], the use of a new pressure method [3], and the application of a strong reducing flame [5] have been proposed to reduce

(a) Fracture surface   **(b) Magnification by SEM**
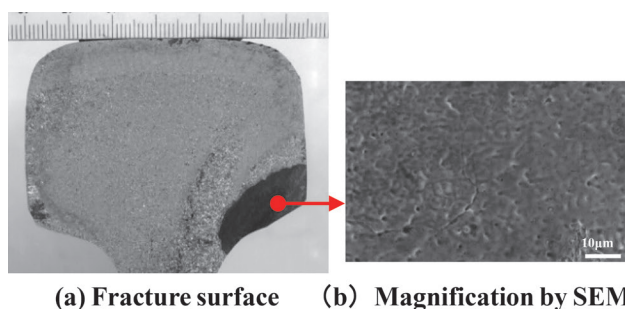
Fig. 2   Example of trimming crackin a rail gas pressure weld

oxide inclusions at the weld interface, and certain results have been obtained. On the other hand, it has been considered that trimming cracks at the corners of rails are caused by the low deformation degree of these areas. Generally, it is difficult to observe deformation behavior during gas pressure welding. Therefore, no study focusing on the degree of deformation in each area has been conducted so far, and no preventive methods that take deformation into account have been proposed.

In recent years, the development of numerical analysis technology and the increase in computational resources have made it relatively easy to perform numerical analysis of large and complex models, and studies using numerical analysis have been increasing in the welding industry [6].

In this study, we constructed an analytical model of heating and deformation of rail gas pressure welds using numerical calculations. Using the model, the deformation behavior of rail gas pressure welds was evaluated quantitatively. This paper describes the details of the analytical model and the results of tests conducted to verify the validity of the analytical model.

2. Thermal deformation analysis for gas pressure welding

Figure 3 shows a schematic illustration of the model used in this study. The model is a quarter-symmetric model centered on the weld interface. The heat flux distribution by gas flame and radiation were applied in the heating range, and radiation and atmospheric convection were applied as boundary condition in the outside of the heating range. The Stefan-Boltzmann law was applied to radiation, and atmospheric convection was assumed to be natural convection.

The weld interface was loaded in the longitudinal direction until an upset length of 24 mm was reached. The initial temperature conditions were 30°C for both the rail and the ambient air.
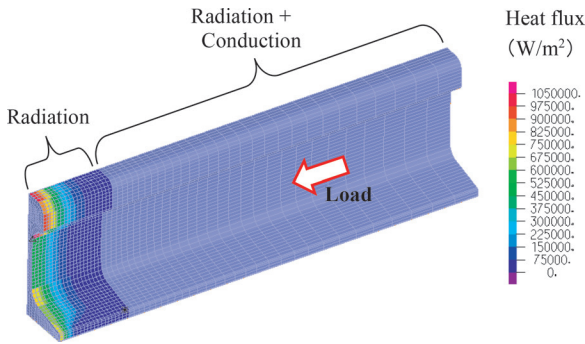
Fig. 3   Analytical model for heating and deformation of rail gas pressure weld

2.1 Thermal model

As mentioned above, the quantity of heat is given as the heat flux from the gas flame into the rail in this study. Generally, in case of heating with an oxy-acetylene gas burner, the gas flame formed at the burner nozzle is divided into a white core (internal flame) and an external flame as shown in Fig. 4(a).

It is known that the external flame has a lower temperature compared with the white core. The gas flame easily changes its shape when it contacts with heating. In case of heating a material with a uniform surface, such as a flat plate or a round bar, the flame can be regarded as a constant shape, as shown in Fig. 4(b). In this study, the heat input distribution into a rail is given as a heat flux distribution. Several analytical studies have been conducted on the heat input distribution from a gas flame as a Gaussian distribution (normal distribution) [7, 8]. However, it is considered that the distribution depends on the shape of the burner and number of the nozzles. Therefore, the following Gaussian distribution type function (Eq.(1)) is used in this study as the distribution of heat input caused by a gas flame.

$$q\,(r) = \frac{q_0}{(\alpha + \beta)} \left(\alpha e^{\frac{r^2}{2\sigma_{b1}{}^2}} + \beta e^{-\frac{r^2}{2\sigma_{b2}{}^2}} \right) \qquad (1)$$

White cone
(Internal flame)

External flame

(a) In the air   (b) On the plate
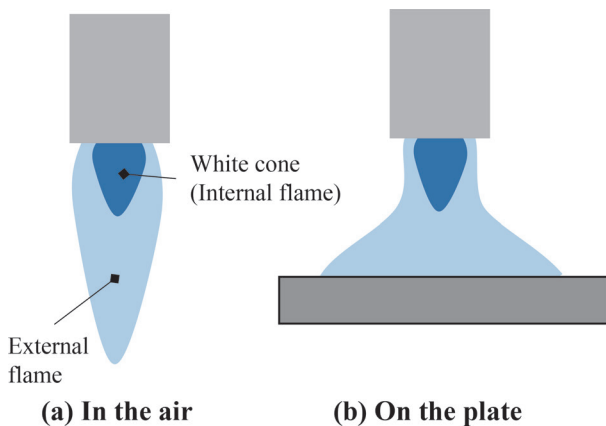
Fig. 4   Schematic illustration of a gas flame shape

where r is the distance from the heating center, q_0 is the heat flux per unit area at the heating center, and both α and β are the heat flux ratio between the white core and the outer flame. In addition, σ_{b1} and σ_{b2} correspond to the standard deviation of the heating flame distribution and were set to be 1/3 of the heating range. Assuming that the total heat input Q, which is the heating value calculated from the acetylene gas flow rate multiplied by the transfer coefficient, is given within the heating range, the following two equations are derived by Gaussian integration.

$$Q = A_0 \int_{-\infty}^{+\infty} q\,(r)\, dr \qquad (2)$$

$$q_0 = \frac{(\alpha + \beta)\, Q}{A_0 \sqrt{2\pi\,(\alpha\sigma_{b1}{}^2 + \beta\sigma_{b2}{}^2)}} \qquad (3)$$

where A_0 is the area of the heating range. Using A_0, the heat flux q_0 at the center of the gas pressure weld was obtained. Figure 5 shows an example of the heat flux conditions and heat flux distribution used in this study.
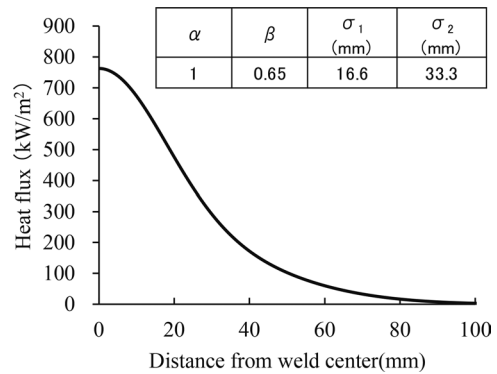
Fig. 5   An example of heat flux conditions and distribution

As presented above, the study focused on the distribution in the longitudinal direction of rail. However, it is also necessary to determine the heating flame distribution in the circumferential direction of rail. The heat input for each burner was determined by multiplying the total heat input Q by the area ratio (burner area divided by total area) calculated from the burner nozzle diameter. It is assumed that the heating flames interacted with those formed at adjacent burners. Therefore, the heat input of rail circumference was divided into eleven sections. The heat input from the burner nozzle corresponding to each section was averaged. Table 1 shows the quantity of heat input on each part around the rail.

2.2 Material model

Temperature dependence of the material model was considered for five physical constants: specific heat (c), thermal conductivity (k), Young's modulus (E), Poisson's ratio (v), and yield stress (σ_y). Figure 6 shows the material properties used in the analytical model. Since the analysis used in this study is based on plastic deformation, a stress-strain relationship that takes the temperature dependence into account is necessary. In this study, high-temperature tensile tests (test temperatures: 1273K, 1373K, and 1473K) were conducted using specimens of rail steel, and the tensile stress σ and strain ε obtained from the test results were approximated by $\sigma = a\varepsilon^b$ based on the results. Note both a and b are determined based on the results of the high-temperature tensile tests.

Table 1   Quantity of heat input on each part around rail

No.	Part	Bunner nozzle area (mm²)	Total quantity of heat (W)
1	Head	2.41	306
2	Uppper corner	1.23	157
3	Side	2.28	289
4	Lower corner	1.17	149
5	Upper neck	2.54	322
6	Web	2.32	294
7	Lower neck	1.73	220
8	Upper base	3.04	267
9	Base end	0.59	75
10	Base	2.16	274
11	Base center	1.91	242
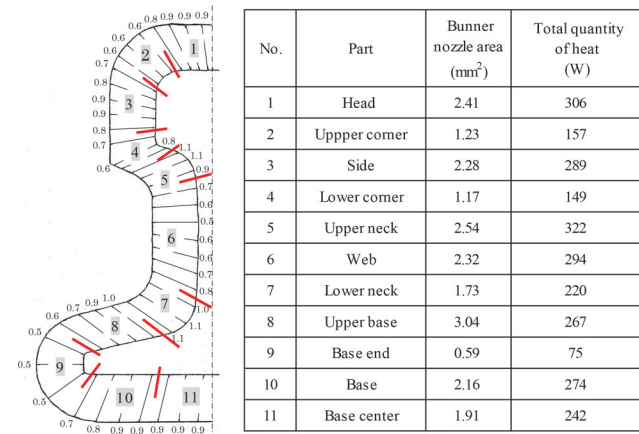
(a) Thermal properties   (b) Structural properties

Fig. 6   Material properties used in the analytical model

2.3 Gas pressure welding test conditions

To verify the analysis results, gas pressure welding tests were conducted using a portable gas pressure welding machine (weight:150 kg) with a JIS E 1101 60 kg standard rail. Figure 7 shows the gas pressure welding test situations. The gas pressure welding conditions were set to the standard conditions of rail gas pressure welding: oxygen 100 L/min, acetylene flow 105 L/min, and upset pressure 22 MPa (171 kN). The upset length during welding was measured with a contact-type displacement gauge installed on the rail end. The center temperature of the weld interface was measured with a K-type thermocouple (a temperature sensor containing Chromel and Alumel conductors) inserted in a machined hole in the rail. Burner swing (moving the burner from side to side to prevent melting of the surface) was started when the upset length reached 14 mm, and heating and pressurizing operations were stopped when the upset length reached 24 mm. The size of the bulge (deformation height) of the pressure weld on the longitudinal and horizontal cross sections was measured and compared with the analytical results.
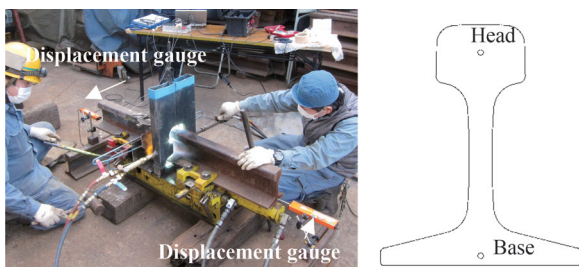
3. Verification of analysis model

Figure 8 shows the appearance of a rail gas pressure weld together with the analytical results. There is no significant difference between the experimental and analytical results. However, in the experimental result, the bulge in the head is uneven due to surface melting. On the other hand, the analytical results ignore the melting phenomenon of surface, so that the bulge shape is smooth. The external form of the rail gas pressure welds was measured with a coordinate measuring machine to compare with the analytical results for each section of the longitudinal and horizontal cross sections. Figure 9 shows the results of the comparison of the deformation heights of the gas pressure welds for each measurement location. Although there is difference of about 15% between the analytical and experimental deformation heights near the weld interface on the head, the deformation heights on the base show relatively good agreement. In addition, although there are differences in the deformation height and deformation shape on the weld interface at the base edge, center of the web, and side of the head in the horizontal section, all of them are within a 20% difference margin.

Figure 10 shows the results of the analysis and experiment of the temperature at the weld interface and upset length. The temperature curves at the weld interface are good agreement with the experimental results at all locations. The difference in both the timing of deformation initiation and the deformation rate were within a margin of about 3%.

From the above, we believe that this analytical model can accurately represent the heating and upset process in rail gas pressure welding.

4. Identification of deformation characteristics on gas pressure welds Analyses and discussions

4.1 Deformation on gas pressure welds by analysis results

In order to quantitatively evaluate the degree of deformation of the gas pressure welds, equivalent plastic strain was used as an indicator in this study. Figure 11 shows the equivalent plastic strain distribution on the weld interface obtained by the analytical model of the rail gas pressure welding for each upset length. Figure 11(b)

(a) Image of gas pressure (b) Temperature
welding in action   measuring positions

Fig. 7   Gas pressure welding test situations
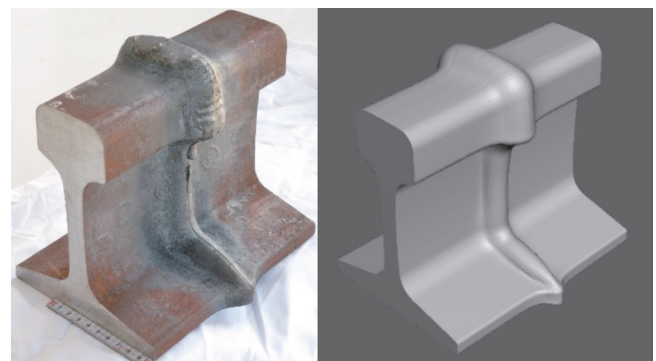
(a) Experiment   (b) Analysis

Fig. 8   Appearance of gas pressure weld

(a) View position   (b) Head (Longitudinal)   (c) Base (Longitudinal)

(d) Base end (Horizontal)   (e) Web (Horizontal)   (f) Side of head (Horizontal)
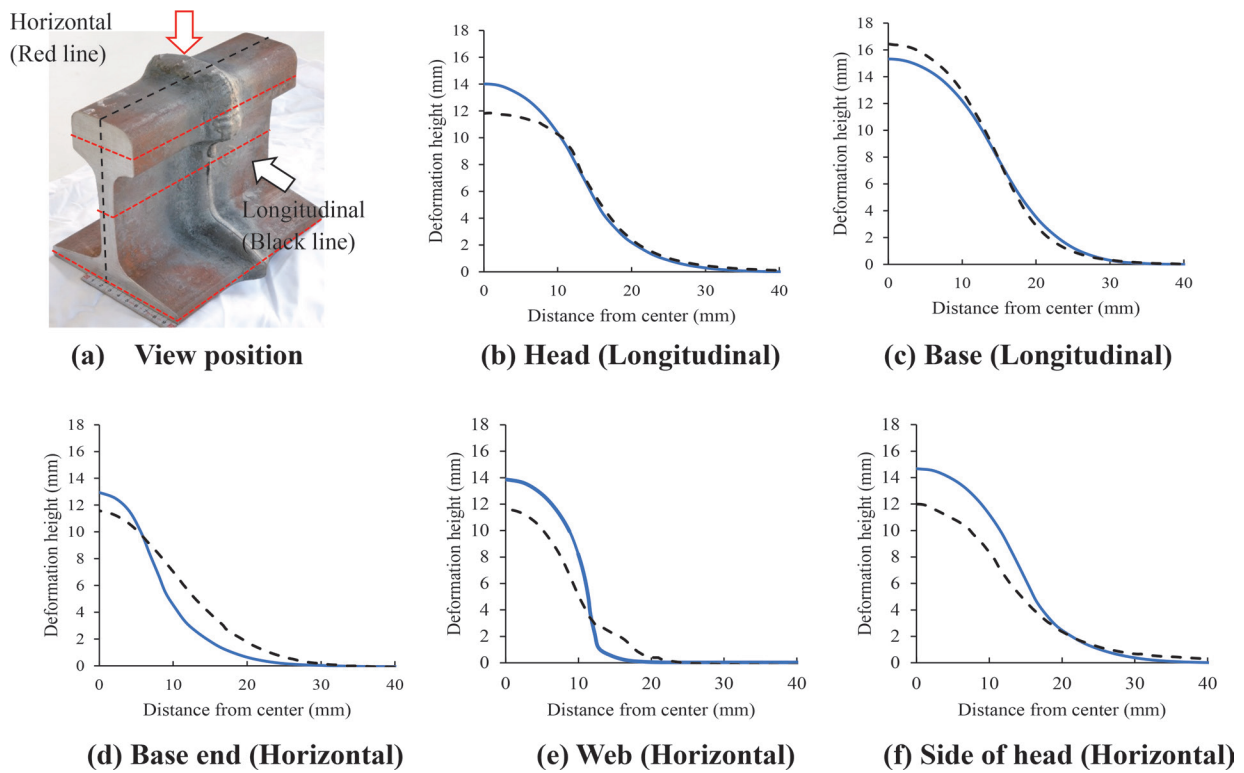
Fig. 9 Comparison of the deformation height between analysis and experiment

(a) Temperature
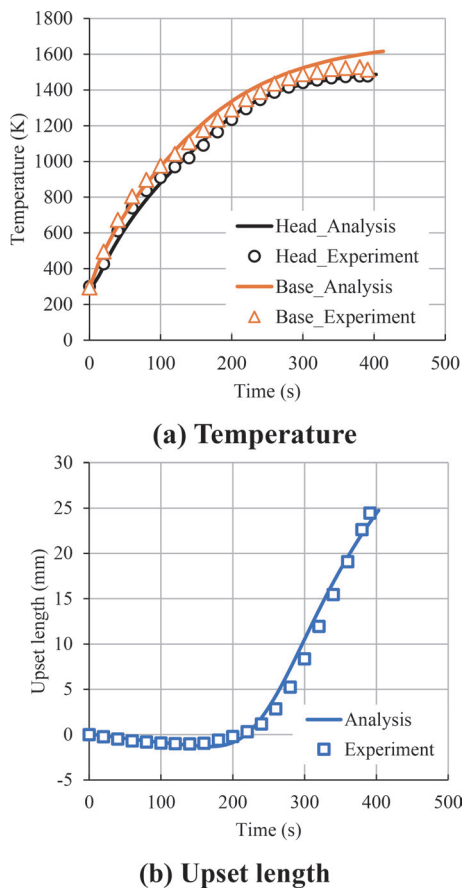
(b) Upset length

Fig. 10 Conparision of analytical resulys with experi mental results for temperature and upset length

plots the equivalent plastic strain in each location on the rail original cross-section. As shown in Fig. 11(a), the equivalent plastic strain on the weld interface is not uniform across the cross-section. For example, large strains occur at the web and base edges, while the strains at the head and center of base are smaller than those in other locations. As shown in Fig. 11(b), the equivalent plastic strain in each region increases with upset length. Additionally, the gradient of the equivalent plastic strain to upset length is large in the web and base edge. On the other hand, the gradient is small under the lower corner of the head and at the center of the base. From these results, it is considered that it is difficult to ensure the weld quality under the lower corner of the head and at the center of the base due to the degree of deformation. Therefore, trimming cracks are more likely to occur in these areas.

4.2 Validation of the analytical model Conclusions

The results of the above analysis revealed that the deformations of the lower corner of the head and the center of the base were relatively low. Thus, it was suggested that trimming cracks occurred in these areas due to the low degree of deformation when welding conditions were poor. On the other hand, it is difficult to determine whether trimming cracks occurred in these areas due to deformation since no trimming cracks were observed under standard conditions. Therefore, we conducted rail gas pressure welding tests in which the welding conditions were intentionally set to be unfavorable to the deformation of the weld interface.

Table 2 shows the gas pressure welding conditions used in this section. The gas flow rates were 100 L/min in oxygen and 105 L/min in acetylene, which are the same as the standard conditions. On the other hand, the applied pressure was 43 MPa, about twice as large as the standard condition, and the upset length was 15 mm, about 60% of the standard condition. Figure 12 shows the analysis results

(a) Contour diagram of equivalent plastic strain

(b) Plot graph of equivalent plastic strain
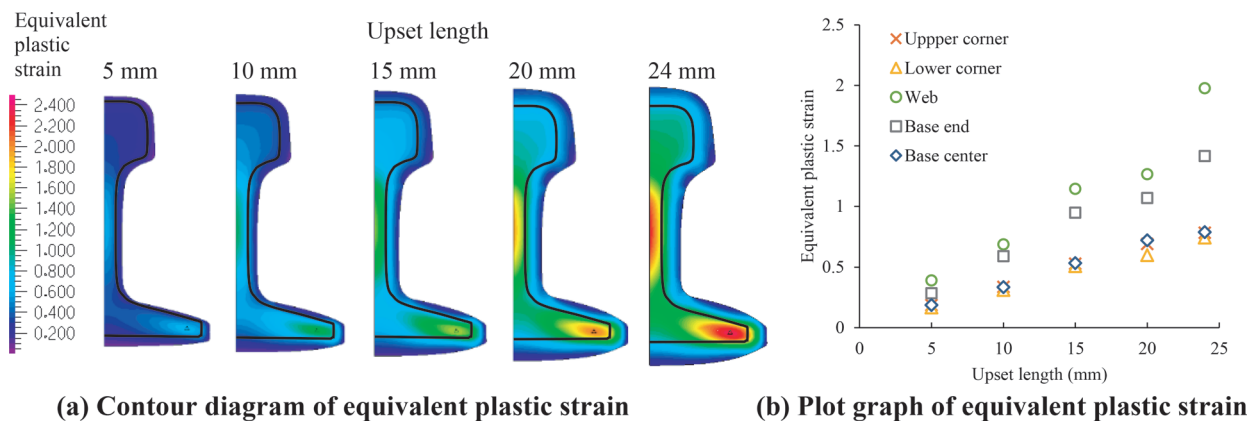
Fig. 11   Equivalent plastic strain distribution on weld interface for each upset length

(equivalent strain distribution at the weld interface) under the conditions shown in Table 2. The results show that the deformation was lower than that under the condition with 24 mm of upset length shown in Fig. 11. Especially, this trend is significant in the lower corner of head and in the center of base.

Table 2   Gas pressure welding conditions for occurring test

Gas flow rate(L/min)		Upset pressure (MPa)	Upset length (mm)
Oxygen	Acetylene		
100	105	43	15

No.	Position	Plastic strain
1	Head	0.43
2	Uppper corner	0.41
3	Lower corner	0.33
4	Web	0.76
5	Lower neck	0.53
6	Upper base	0.55
7	Base end	0.56
8	Base center	0.37
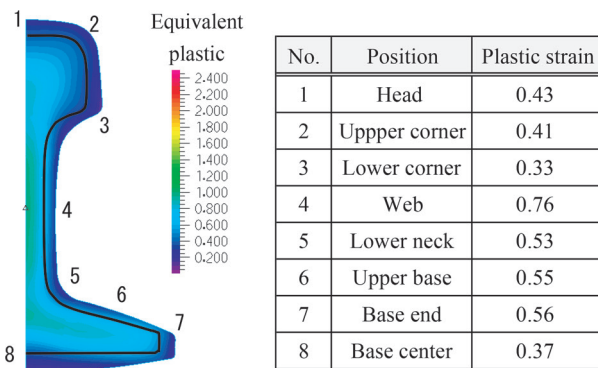
Fig. 12   Results of deformation analysis under occurring test conditions

Figure 13 shows the results of a magnetic particle test. The results of the magnetic particle test showed flaw indications of 18 mm and 11 mm length on the lower corner of head and the center of base, respectively. In order to confirm the appearance of the defects and the strength of the specimen, a slow bending test was conducted with a concentrated load at the center of the 1 m span (head-up position). Figure 14 shows the fracture surface of the slow bending test. The results of the test showed that the fracture load of the specimen was 481 kN and the deflection of the specimen was 4.7 mm, which are much lower than the criteria in the bending test for gas pressure weld of JIS 60 kg standard rail (load:1400 kN, deflection:25 mm). In addition, trimming cracks were observed on the fracture surface under the lower corner of head and the center of base, where the deformation degree was predicted to be low by the analytical model.

These results indicate that it is possible to predict occurrence of defects in rail gas pressure welds by calculating the deformation using the analytical model.
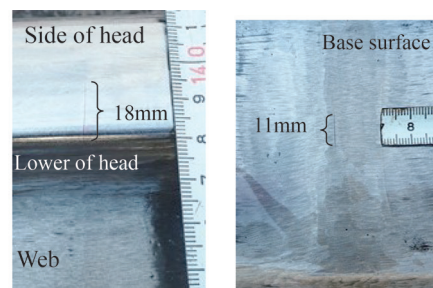
(a) Flaw indications in magnetic particle test
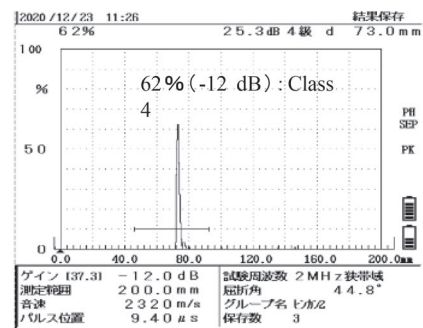
(b) Flaw echo in ultrasonic test

Fig. 13   Results of magnetic particle testing and ultrasonic tests on specimens

5. Conclusion

We developed an analytical model for simulating the heating and deformation of a rail gas pressure weld to quantitatively understand the deformation behavior of the weld interface. The results obtained in this study are as follows.

(1) An analytical model of heating and deformation of a rail gas pressure weld using a heat input model approximated by a Gaussian distribution and a material was developed. This model considered the material properties at high temperatures.

(a) Fracture surface   (b) Magnification
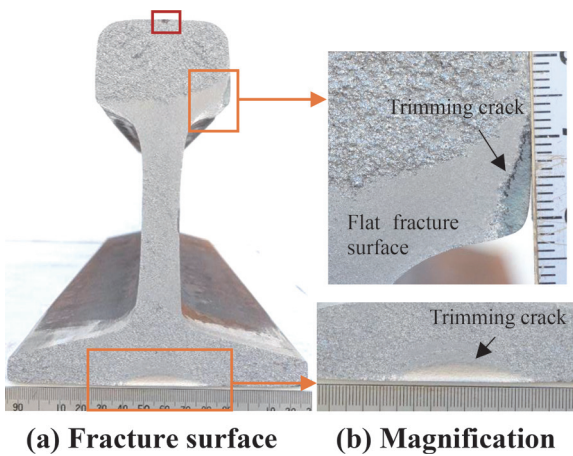
Fig. 14   Fracture surface in slow bending

Comparing the analytical results with the experimental results, it was confirmed that the model can accurately represent the heating and upsetting processes in rail gas pressure welding.

(2) From the analysis results of the model, it was found that the deformation in the lower corner of head and the center of base was smaller than that in other parts of the model. Occurring tests showed that trimming cracks occurred in these areas. Therefore, it is considered that trimming cracks are likely to occur in these areas due to small deformation.

(3) It was shown that the analytical model of the rail gas pressure welding can be used to predict the occurrence of defects in the rail gas pressure weld. The authors would like to express their sincere gratitude to Prof. Christopher Barnes for his guidance and teachings, without which the writing of this paper would not have been possible.

References

[1] Yamamoto, R., "Welding Technology of Rails," *Journal of the Japan Welding Society*, Vol. 81, No. 8, pp. 641-649, 2012 (in Japanese).

[2] Yamamoto, R., "Rail Welding in Japan," *11th International Heavy Haul conference,* Cape Town, South Africa, September 2-5, 2017.

[3] Oishibashi, H., Ueyama, K., "Investigation for Quality Estimation Mechanism of Gas Pressure Welds," *Quarterly Journal of the Japan Welding Society,* Vol. 2, No. 14, pp. 422-428, 1996 (in Japanese).

[4] Tatsumi, M., Fukada, Y. et al., "Improvement of Gas Pressure Welding for Rail," *RTRI Report*, Vol. 13, No. 5, pp. 27-32, 1999 (in Japanese).

[5] Yamamoto, R., Tatsumi, M., Itoh, H., Komizo, Y., "Experimental Examination for Decreasing the Oxide Inclusions in Gas Pressure Welding of Rail," *Quarterly Journal of the Japan Welding Society*, Vol. 29, No. 4, pp. 258-266, 2011 (in Japanese).

[6] Mochizuki, M., Mikami, Y., Okano, S., Shibahara, M., "Simulation of Welding Deformation and Residual Stress," *Journal of the Japan Welding Society,* Vol. 84, No. 1, pp. 66-74, 2015 (in Japanese).

[7] Tsuji, I., Okumura, Y., "A Study on Line Heating Process for Plate Bending of Ship Steels," *Transactions of the West-Japan Society of Naval Architects,* No. 76, pp. 149-160, 1988 (in Japanese).

[8] Oishibashi, H., Akama, M., Ueyama, K., "Finite Element Analysis of Deformations and Stresses of Gas Pressure Welding and Hot Shearing," *Quarterly Journal of the Japan Welding Society,* Vol. 14, No. 2, pp. 435-442, 1996 (in Japanese).

Authors

Hajime ITOH, Dr. Eng.
Senior Researcher, Rail Maintenance & Welding Laboratory, Track Technology Division
Research Areas: Rail Welding, Nondestructive Inspection of Rail

Ryu-ichi YAMAMOTO, Dr. Eng.
Senior Chief Researcher, Head of Rail Maintenance & Welding Laboratory, Track Technology Division
Research Areas: Rail Welding, Nondestructive Inspection of Rail

Fatigue Life Evaluation of PC Sleepers Based on Wheel Load Measurement Results

Keiichi GOTO
Structural Mechanics Laboratory, Railway Dynamics Division

Tsutomu WATANABE **Shintaro MINOURA**
Track Dynamics Laboratory, Railway Dynamics Division

Manabu IKEDA
Structural Mechanics Laboratory, Railway Dynamics Division

In this study, the remaining life of PC sleepers is evaluated from the viewpoint of the fatigue life of PC-steels of PC sleepers. Specifically, a method of acquiring the stress waveform of PC-steels during train running is developed. Furthermore, using this waveform, we calculate the fatigue strength of PC-steels in consideration of the occurrence probability of wheel loads in actual measurement, and quantitatively evaluate the fatigue life of PC-steels. The result of this study shows that PC-steels for a post-tension type have a longer fatigue life than those for a pre-tension type, and PC-steels for both types have a fatigue life of over 300 years.

Key words: *prestressed concrete sleeper, fatigue life, field measurement, numerical analysis*

1. Introduction

Prestressed concrete sleepers (hereinafter referred to as "PC sleepers") are an important component of railway tracks and have been indispensable for increasing running speeds and improving ride comfort in recent years [1]. Some PC sleepers on commercial lines have already exceeded their design service life, which is generally considered to be about 50 years [2]. Railway operators are, therefore, proceeding with a fact-finding survey of aged PC sleepers and conducting studies on replacement standards to plan future maintenance [3]. Given that PC sleepers are factory made, they rarely pose a problem from the viewpoint of material durability like resistance to neutralization and salt damage; their service life is mainly determined from a mechanical viewpoint. The section force generated in a PC sleeper forms a large proportion of the variable load, and the number of repetitions is very large; therefore, it is important to study the PC sleeper service life from the viewpoint of fatigue fractures, especially of the prestressing steel (PS) placed inside PC sleepers [4]. There are, however, many unclear points about PC sleeper fatigue life because PC sleeper design assumes full prestress in the serviceability limit state, and so verifications are omitted.

Therefore, this study constructed a method for analyzing vehicle-track dynamic interaction that can reproduce bending moments (BM) of PC sleepers generated during train running. It also constructed a numerical analysis method that can evaluate the PS stress inside PC sleepers for two types of PC sleepers with different tensioning methods. The PS stress waveform generated during train running was then obtained by combining the results of both these methods. Furthermore, by calculating the tensile fatigue strength of the PS from this stress waveform and the measured probability of wheel load (WL) occurrence, the fatigue life of PC sleepers was quantitatively evaluated, and the difference in tensioning methods was also clarified.

2. Dynamic response of PC sleeper

This chapter describes the construction of a vehicle-track dynamic interaction analysis method and evaluates the BM of PC sleepers at a welded rail joints using this method.

2.1 Target section and measurement outline

Figures 1 and 2 outline a track structure and PC sleepers to be examined. The target section was a straight track with continuously welded 50 kgN rails (Japanese Industrial Standers (JIS) E 1101) and type 3 pre-tensioned PC sleepers (3PRs) specified in JIS E 1201. Figure 3 shows a type 3 unbonded post-tensioned PC sleeper (3PO), which has the same shape as 3PR but differs only in the tensioning method. 3PO was used for comparison in the fatigue life with 3PR in this study.

Figure 4 shows rail surface roughness in the target section, which was measured using a rail top surface roughness measuring instrument with a length of 1 m. The roughness of up to 0.5 mm near Sleeper No. 6 and 7 occurred due to a welded rail joint.

The BM of the PC sleepers was measured as trains passed. The BM was calculated by converting from the output of strain gauges attached to the side surface of the rail section of each sleeper (near the upper and lower edges). The passing trains were commuter and freight trains. For details of this measurement, see Reference [5]).

2.2 Numerical analysis method

2.2.1 Dynamic vehicle model

Figure 5 shows the dynamic vehicle model. This vehicle model is a half-body model with the car-body, bogie, and wheelset assumed to be rigid bodies, and is constructed by connecting them with dampers and springs. This model expresses the condition of running vehicles by exerting forced displacement in the traveling direction on each rigid body. It assumes conventional commuter train vehicles.
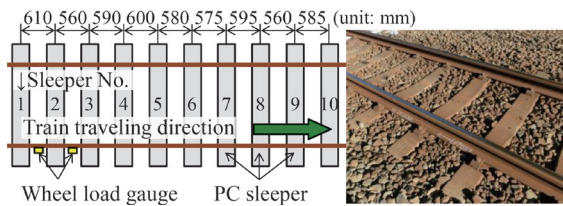
Fig. 1   Outline of the target section
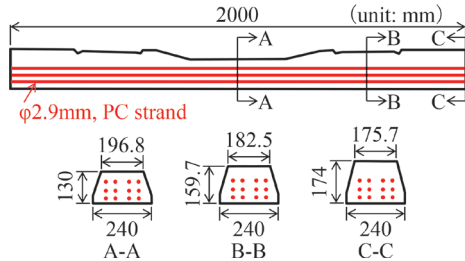
Fig. 2   Outline of 3PR
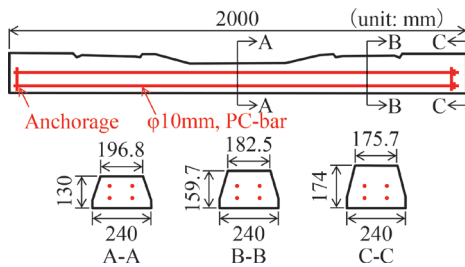
Fig. 3   Outline of 3PO
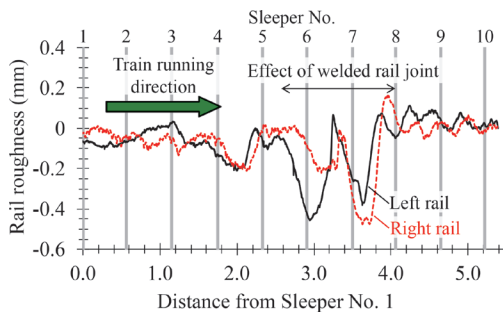
Fig. 4   Rail surface roughness in the target section

2.2.2 Dynamic track model

Figure 6 shows the dynamic track model. Rails and PC sleepers are modeled with beam elements. Rail pads, ballast, and roadbeds are modeled with springs and dampers. The present study modeled this track for approx. 24 m.

2.2.3 Wheel-rail contact model

The contact between the wheel and rail was considered only in the vertical direction, and a penalty method was used to calculate the dynamic interaction force. During contact calculation, the rail surface roughness was expressed by considering the roughness amount pre-defined as a function of the rail position.
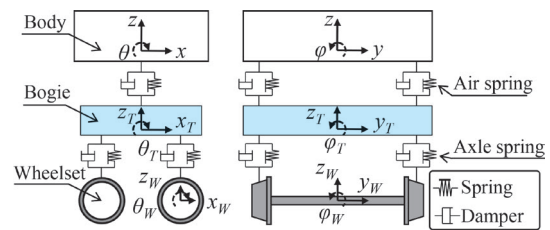
Fig. 5   Dynamic model of vehicle (half vehicle)
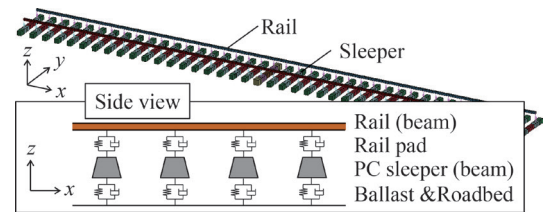
Fig. 6   Dynamic model of track

2.2.4 Analysis specifications

Table 1 summarizes analysis specifications for components used in this study. These specifications were determined by reference to design standards, measured values [5] for the target section, and a previous study [6].

2.3 Numerical analysis results

Figure 7 shows the BM waveform at the left rail position (see Fig. 1 and 4) of Sleeper No. 7 as an example showing a comparison between the measured and analyzed values. The measured values are the results from the passage of adjacent two bogies, and the analyzed values the results from the passage of one bogie (i.e., a half vehicle).

Figure 7 also shows the difference in the analysis of the rail with and without rail surface roughness. First, focusing on the measurement results, the waveforms generated during the passage of each bogie are almost the same; therefore, we can see that the BM of a bogie as one unit acts repeatedly on PC sleepers. Secondly, focusing on the analysis results (with rail surface roughness), we can see that the characteristics such as the measured waveform shape and maximum value are accurately reproduced.

Figure 8 shows the effect of vehicle speed on the PC sleeper BM. It shows the BM at the left and right rail positions and at the sleeper center position, comparing the conditions with/without rail surface roughness. The figure clarifies the train-speed dependency in which the BM increases as vehicle speed increases in condition of rail surface roughness.

3.   Evaluation of PS stress by static detailed analysis

In this chapter, we constructed a numerical analysis model with which the static bending test of PC sleepers can be simulated and to evaluate the stress state of PS placed inside the PC sleepers.

3.1 Outline of static bending test

Figure 9 outlines the PC sleeper static bending test defined in JIS E 1201 and 1202. There are two types of bending tests: one is at rail positions and the other is at the sleeper center position. This

Table 1　Analysis specifications

Vehicle (Semi-vehicle)	Conventional commuter train (Static wheel load: 54.3 kN) Train speed: 83 km/h (measured)
Rail	Type: 50 kgN rail Track gauge: 1067 mm Bending rigidity EI: 3.94 MN*m^2 Unit weight: 77.0 kN/m^3
Rail pad (per side)	Spring constant: 110 MN/m Damping constant: 30 kN*s/m
Sleeper	Type: 3PR Spacing: Fig. 4 (measured) Young's modulus E: 33.0 GPa Unit weight: 23.0 kN/m^3
Support spring of sleeper (per side)	Spring constant: 68.7 MN/m (measured) Damping constant: 98 kN*s/m
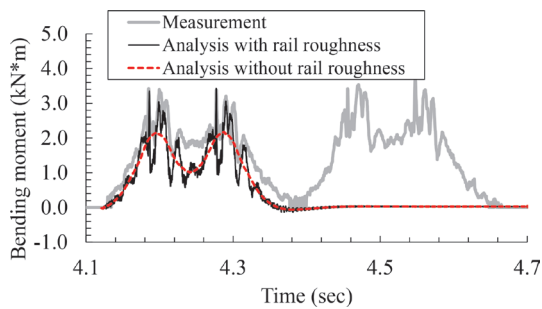
Fig. 7　BM waveform of Sleeper No. 7
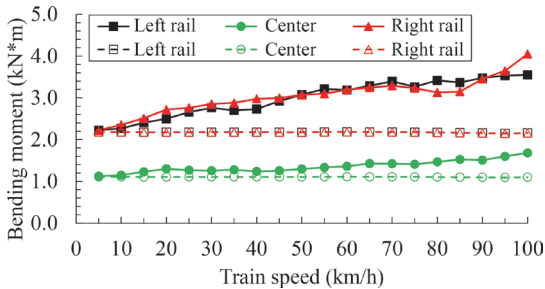
Fig. 8　Effect of vehicle speed on BM

study conducted only the bending test at rail positions. The PC sleepers to be examined were 3PRs (Fig. 2) and 3POs (Fig. 3) shown in Chapter 2. Tests were conducted on two new products.

3.2　Numerical analysis method

3.2.1　Numerical analysis model

Figure 10 shows an analysis model for the 3PR and 3PO bending tests. This analysis model consists of the concrete that makes up the PC sleepers, PS (PC strands or PC bars), stirrups or anchorages, and the load receiver and supports. It was designed as a 1/2 model in consideration of the symmetry of the structure. The concrete, load receiver, and supports were modeled with eight-node solid elements, the PS and stirrup with beam elements, and the anchorage with shell elements. The load receiver and support were defined as rigid bodies. As for the boundary conditions, the symmetric boundaries of the analysis model were constrained in consideration of
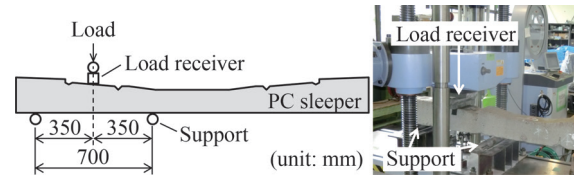
Fig. 9　The outline of PC sleeper static bending test

(a) Concrete, load receiver and support

(b) PC strands and stirrup (3PR)

(c) PC bar and anchorage (3PO)
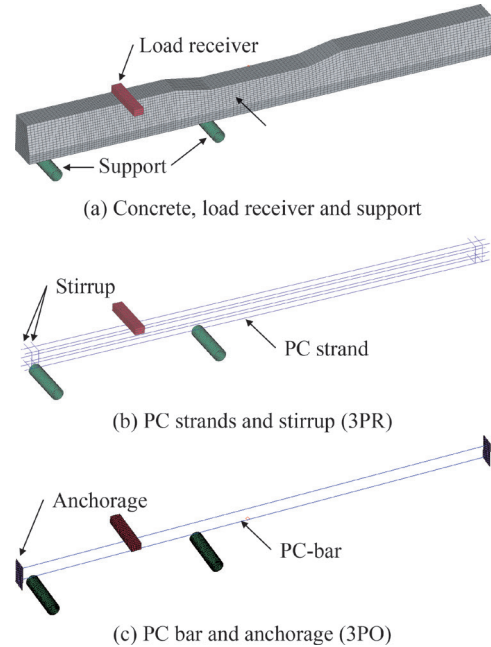
Fig. 10　Analysis model of the bending test

plane symmetry, the load receiver constrained the degrees of freedom other than the vertical direction (loading direction), and the support constrained all degrees of freedom. For the adhesion between concrete and PS, the complete adhesion model was used for 3PRs, and the model allowing only axial slip of the PS was used for 3POs. Plane-plane contact was defined between the concrete and load receiver and between the concrete and supports.

3.2.2　Material constants and material models

Table 2 lists the material constants used in this analysis. The concrete material constants were determined based on the design standard [2] from the uniaxial compression strength value of the test piece. The material constants for PS were derived from the mill sheet. The effective rate of the tensile force introduced into the PS was defined as 75% for 3PRs or 95% for 3POs based on the design standard [2] and bending test results. The initial tensile stress equivalent to this tensile force was applied to each PS element.

Figure 11 shows the material model used in this analysis. Figure 11 (a) shows the single-axis converted stress-strain relationship in terms of the concrete, which was modeled to enable expression of compression fracture and tension softening. Figure 11 (b) shows the single-axis converted stress-strain relationship in terms of the PS. The constant for this material model was read and input from the mill sheet.

Table 2 Material constants in this analysis

	Material	Elastic modulus E (GPa)	Poisson's ratio	Strength (MPa)
3PR	Concrete	35.0	0.20	f'_c: 60.0 f_t: 3.53
	PC strand	200.0	0.30	σ_y: 1500.0 σ_u: 1998.0
	Stirrup	200.0	0.30	Elastic
3PO	Concrete	34.7	0.20	f'_c: 60.0 f_t: 3.53
	PC-bar	200.0	0.30	σ_y: 1200.0 σ_u: 1415.5
	Anchorage	200.0	0.30	Elastic

(a) Concrete (b) PC-steel
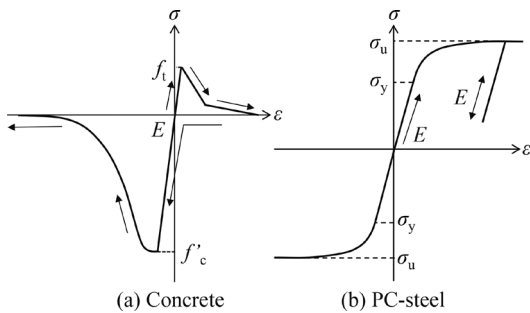
Fig. 11 Material model

3.3 Numerical analysis results

3.3.1 Validation of the analysis results

Figure 12 shows a comparison between the test results with the analysis results. The figure shows that the rigidity reduction with the occurrence of cracks and the load-bearing capacity and the load-displacement relationship up to the fracture were reproduced accurately. Figures 13 and 14 show a comparison of the occurrence of cracks. The results of the analysis are shown by the contour diagram of the plastic strain corresponding to the maximum load. In addition to the number of major cracks, the figure shows that their development tendencies are similar.

3.3.2 Evaluation of PS stress state

Figure 15 shows the relationships between the BM and concrete stress and between the BM and tensile stress of the PS for 3PR and 3PO. As for the concrete stress, the figure shows the stress in the sleeper longitudinal direction at the concrete element at the outermost tension directly under the load receiver. Also for the PS, it shows the tensile stress of the lowest element directly under the load receiver that caused the maximum tensile stress. The BM on the horizontal axis in this figure was obtained by converting the applied load in Fig. 12 based on simple beam theory. In this figure, we can confirm that the concrete stress shifted from the compression zone to the tension zone as the BM increased, and after it reached the tensile strength, the stress decreased by the occurrence of cracks. This figure also shows the PS tensile stress increased sharply after the concrete cracking. We can see that this sharp rise in PS stress started at smaller BM at 3PR than at 3PO.
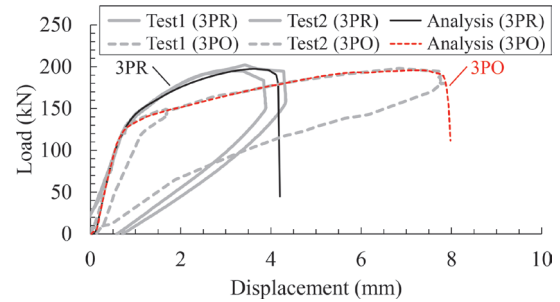
Fig. 12 Comparison between bending test and numerical analysis
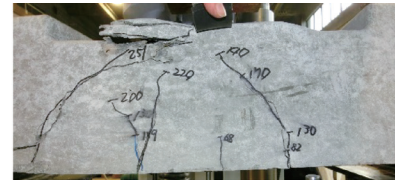
(a) Test result (after loading)
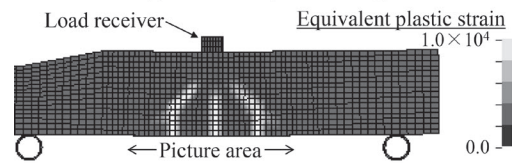
(b) Analysis result (at max. load)

Fig. 13 Comparison of cracking (3PR)

(a) Test result (at max. load)
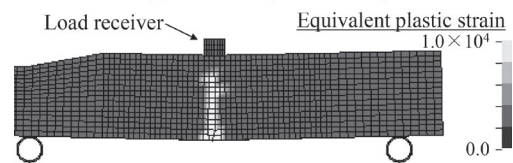
(b) Analysis result (at max. load)

Fig. 14 Comparison of cracking (3PO)

4. PS fatigue life evaluation considering the probability of WL occurrence

In this chapter, we evaluated the fatigue life of PC sleepers focusing on the tensile fatigue strength of PS based on the measurement results regarding the probability of WL occurrence in addition to the studies in the previous chapters.

4.1 Actual condition of WL and its occurrence probability

To know the actual conditions of WLs, we measured WLs of running trains in the target section in Chapter 2. Figure 1 shows the WL measurement positions. Using WL gauges installed on the rail web, WL measurements were conducted for 44 days on a total of
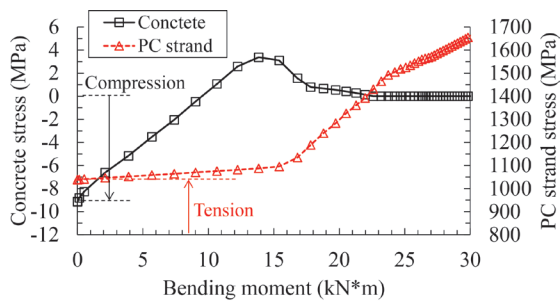
(a) 3PR
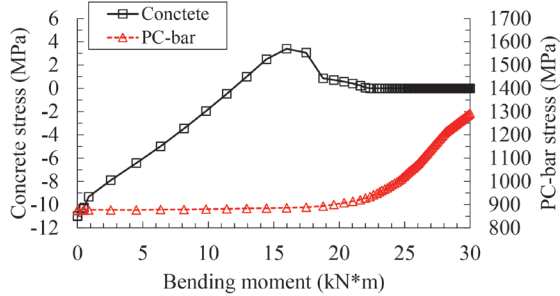
(b) 3PO

Fig. 15 Stress state of concrete and PS

Fig. 16 WL excess and occurrence probability

Fig. 17 Flow of PS fatigue life evaluation

Fig. 18 Example of the PS stress waveform

Fig. 19 Equivalent number of repetitions

8167 trains (commuter and freight trains).

Figure 16 shows the measurement results summarized by WL excess and occurrence probability distributions. It clarifies the peak probability of occurrence corresponding to the running of commuter and freight trains.

4.2 PS fatigue life evaluation

As the target of fatigue life evaluation, we selected the PS of Sleeper No. 7 at the welded rail joint where the largest BM occurred in the target section to examine in Chapter 2 (Fig. 1). Figure 17 shows the flow of PS fatigue life evaluation in this study. First, based on the BM waveform of the PC sleeper during one bogie passing (Fig. 7) from the dynamic interaction analysis in Chapter 2 and the relationship between the BM and PS stress (Fig. 15) from the detailed static analysis in Chapter 3, the stress waveform of the PS during one car passing is created via the BM, which is a common parameter for both. The WL of traveling vehicles varies as seen from the measurement results. Therefore, we decided to create a PS stress waveform corresponding to each WL value within the measured WL range by multiplying the BM waveform calculated from the dynamic interaction analysis by the ratio of the measured WL to the static WL. Figure 18 shows an example of the PS stress waveform calculated for PS strands. Next, the random PS stress wave-

form corresponding to each obtained WL value was decomposed into individual independent waves ($\sigma_{1,m}$, $\sigma_{2,m}$, ..., $\sigma_{n,m}$) and the number of repetitions ($N_{1,m}$, $N_{2,m}$, ..., $N_{n,m}$) by using the range pair method [2]. Furthermore, the equivalent number of repetitions, N_m, per single-bogie passage at each WL value, P_m, converted to the maximum variable stress, σ_{max}, at the reference WL was obtained as shown in Fig. 19 by using Miner's law [2]. Next, the expectation value, $N_{m,exp}$, of the equivalent number of repetitions per single-bogie passage shown in Fig. 20 was calculated by multiplying the equivalent number of repetitions, N_m, per single-bogie passage at each WL value, P_m, by the probability of occurrence at each WL value in Fig. 16. Finally, the total, N_{exp}, of the expectation values, $N_{m,exp}$, of the equivalent number of repetitions was calculated, and the expectation value of the PS tensile fatigue strength for each year was calculated.

Figure 21 shows the results of examining the PS fatigue life. This study assumed that PS fatigue fractures occur when the expectation value of PS tensile fatigue strength reaches the maximum variable stress, σ_{max}, at the reference WL. The values in the figure are those obtained by dividing the expectation value of PS tensile fa-
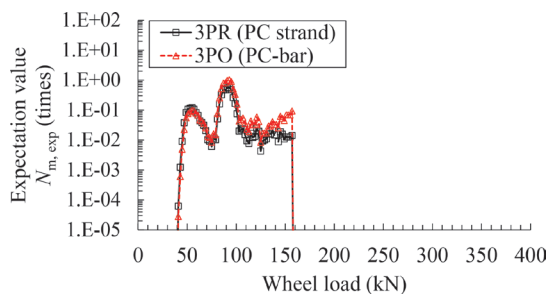
Fig. 20 Expectation value of equivalent number of repetitions
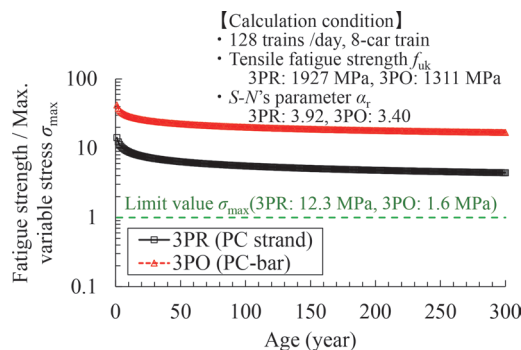
Fig. 21 Results of examining the PS fatigue life

tigue strength by the maximum variable stress, σ_{max}. The figure shows that post-tensioned 3POs have a longer fatigue life and higher fatigue resistance than pre-tensioned 3PRs. The main reason for this was that, in 3POs, the increase in PS stress for the increase in BM was smaller and the variable stress was smaller as seen from Fig. 15. However, both results are well above the limit even at 300 years of use; under the conditions of this study, it is highly unlikely that PS fatigue fractures will determine the life of PC sleepers.

5. Conclusion

The findings from this study are summarized as follows:
(1) We validated the present method by constructing a vehicle-track dynamic interaction analysis method that can reproduce the PC sleeper BM generated during train running and comparing the analyzed values with the measurement results of the welded rail joint.
(2) We constructed a detailed analysis method that can accurately reproduce the load-displacement relationship and the crack occurrence situation, in the static bending test of PC sleepers specified in the JIS standard.
(3) We obtained the PS stress waveform generated during train running from the above method and made it possible to evaluate the PS fatigue life by examining the actual WL occurrence probability for this waveform. As for the welded rail joints to examine, the post-tensioned type has higher fatigue resistance than the pre-tensioned type; however, both have a fatigue life of 300 years or more, indicating that it is extremely unlikely that PS fatigue fractures will determine the life of PC sleepers.

This study targeted new PC sleepers under very limited conditions. Therefore, in the future, we plan to examine the effects of differences in line section conditions on fatigue life and to comprehensively evaluate the life of PC sleepers, including the effects of aging (e.g., decrease in compression strength, prestress loss, reduced cross-section due to wear, PS corrosion).

References

[1] Watanabe, T., "Prestressed concrete sleeper," *RRR*, Vol. 72, No. 10, pp. 28-31, 2015 (in Japanese).
[2] Railway Technical Research Institute, *Design Standards for Railway for Railway Structures and Commentary (Track structures)*, Maruzen Co., Ltd., Tokyo, 2012 (in Japanese).
[3] Watanabe, T., and Sogabe, M., "Evaluation of loading capacity of aged prestressed concrete sleeper," *J. Japan Railway Civil Engineering Association*, Vol. 56, No. 4, pp. 242-245, 2018 (in Japanese).
[4] Wakui, H. and Okuda, H., "A study on limit state design method for prestressed concrete sleepers," *Concrete Library of JSCE*, No. 33, pp. 1-25, 1999.
[5] Watanabe, T., Goto, K., Matsuoka, K., and Minoura, S., "Validation of a dynamic wheel load factor and the influence of various track irregularities on the dynamic response of prestressed concrete sleepers," *J. Rail and Rapid Transit*, Vol. 234, No. 10, pp. 1275-1284, 2020.
[6] Suzuki, T., Ishida, M., Abe, K., and Koro, K., "Measurement on Dynamic Behavior of Track near Rail Joints and Prediction of Track Settlement," *QR of RTRI*, Vol. 46, No. 2, pp. 124-129, 2005.

Authors

Keiichi GOTO, Dr. Eng.
Senior Researcher, Structural Mechanics Laboratory, Railway Dynamics Division
Research Areas: Dynamic Interaction between Vehicle and Bridge, Post-derailment Vehicle Behavior

Tsutomu WATANABE, Dr. Eng.
Senior Researcher, Track Dynamics Laboratory, Railway Dynamics Division
Research Areas: Structure-borne Noise, Vibration, Concrete Sleeper, Numerical Simulation

Shintaro MINOURA, Dr. Eng.
Assistant Senior Researcher, Track Dynamics Laboratory, Railway Dynamics Division
Research Areas: Cryogenic Systems

Manabu IKEDA, Dr. Eng.
Senior Chief Researcher, Head of Structural Mechanics Laboratory, Railway Dynamic Division
Research Areas: Hybrid Structures, Steel Structures

Design Method for Grouted Ballastless Track Roadbed Improvement

Kazuki ITO
Track Structures and Geotechnology Laboratory, Track Technology Division

Yoshitsugu MOMOYA
Track Technology Division

Takahiro KAGEYAMA
Track Structures and Geotechnology Laboratory, Track Technology Division

In order to reduce the cost of track maintenance, grouted ballastless tracks for existing lines where ballast voids are filled with cement grout have been developed and put into practical use. However, there is a problem that some constructed grouted ballastless tracks laid on soft roadbeds are in need of repair within only a few years after operations restart. Therefore, we have developed a method for improving grouted ballastless tracks laid on soft roadbeds and carried out construction work to verify the developed method on existing lines. The roadbed improvement thickness for construction was determined according to design flow proposed in this paper. This paper also describes the improvement method developed for grouted ballastless tracks for existing lines and its verification results.

Key words: grouted ballastless track, roadbed improvement, design method

1. Introduction

Ballasted tracks require regular track maintenance because plastic settlement occurs because of deformation of ballast beds due to repeated train passage. In order to reduce track maintenance costs, a paved track [1] was developed that suppresses settlement in track beds by filling ballast gaps with heated asphalt. Subsequently, for the purpose of improving workability, an E-type pavement track [2] filled with cement asphalt mortar instead of heated asphalt was developed, however there was still a need to reduce construction costs. Therefore, a track (hereinafter referred to as "grouted ballastless track") (Fig. 1) was developed to make ballast bed into pre-packed concrete by filling ballast gaps with low-cost cement-based grout material [3].

On the other hand, cohesive soil such as *Kanto* loam is widely distributed in the Tokyo metropolitan area. Therefore, some grouted ballastless tracks will be repaired within a few years after operation due to the softening of the roadbed and poor drainage of rainwater; maintenance costs may be higher than for ballasted tracks in those conditions [4].

On the basis of the experience of laying and repairing so far, it is essential to install drainage facilities when laying new grouted ballastless tracks on the soft roadbed. It has been reported that the damage to grouted ballastless tracks has been reduced by the installation of drainage facilities [5]. In addition, it has been reported that most of the damage to grouted ballastless tracks is occurs in locations where the tracks are laid on roadbeds with a coefficient of ground reaction K_{30} value of about 30 MN/m^3 [6]. However, roadbed improvement, which is considered to be one of the most effective countermeasures, has not been implemented. One of the reasons is that the construction of grouted ballastless tracks is carried out at night (between the last train and the first train), and is difficult to extend the length of construction without benefit being outweighed by cost.

This research therefore aimed to develop a grout filling road-bed improvement method (hereinafter referred to as "post-filling method") [7] in which roadbed improvement and the construction of grouted ballastless track are performed simultaneously, targeting locations where grouted ballastless tracks are constructed on soft roadbeds (Fig. 2). In this construction method, roadbed improve-
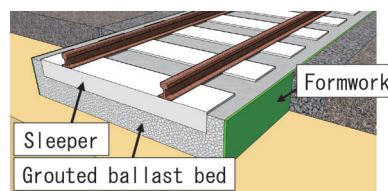
Fig. 1 Structure of grouted ballastless track
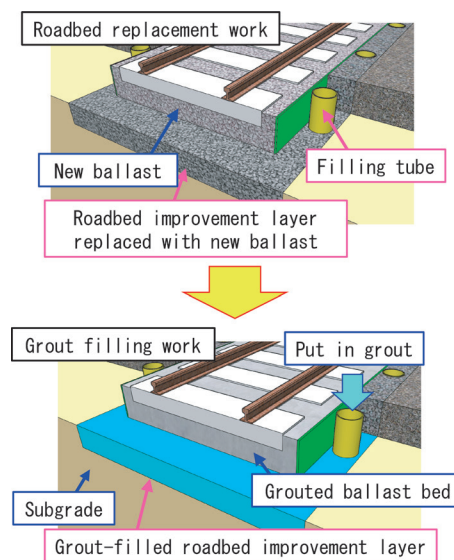
Fig. 2 Grout filling roadbed improvement method (post-filling method)

ment is divided into two stages (roadbed replacement work and grout filling work), to optimize the efficiency of each task and extend the length of construction per day. By applying roadbed improvement to grouted ballastless tracks, vertical stress generated in roadbeds and plastic settling can be suppressed, and bending stress generated in the lower surface of grouted ballastless bed can be reduced. Compared to when there is no roadbed improvement, applying this method is expected to reduce the risk of fatigue fracture of grouted ballast bed.

The roadbed improvement design method developed in this study determines the roadbed improvement thickness so that the settlement remains within the allowable limit, and the roadbed itself does not cause fatigue fractures due to repeated train loads during the design service life.

This report describes the procedure for determining the improvement thickness using the developed roadbed improvement design method, and results which confirm the settlement suppression effect of this method through construction on commercial lines.

2. Roadbed improvement thickness design method

2.1 Design procedure

Figure 3 shows the design flow for roadbed improvement, which is described here. The first step is to investigate the subgrade stiffness in (1) and set the design conditions in (2). In (3), based on the survey result of (1), the design response value is obtained for when the roadbed improvement is applied. In (4), an improved thickness is selected which satisfies the design conditions set in (2), then the improved thickness selected in (5) is examined to ensure that it can actually be constructed, and to determine the design roadbed improved thickness. Using this design method, the appropriate roadbed improvement thickness can be determined by checking the settlement amount of grouted ballastless tracks and the fatigue fracture of grouted ballast bed with respect to the design working life and the allowable settlement amount.

In the following sections, the above design procedure is described in detail. In the case described, the existing line where grouted ballastless tracks were already laid, grouted ballastless tracks were removed, and the grout filling roadbed improvement method constructed together with the reconstruction of grouted ballastless tracks (post-filling method). This paper explains the process where improved thickness was designed and constructed according to the design flow of Fig. 3 (post-filling method).

2.2 Survey of subgrade stiffness

The construction site shown in Fig. 4 is a grouted ballastless track laid directly on *Kanto* Loam, and preliminary surveys were conducted between the upper and lower lines. Preliminary surveys included a simple dynamic cone penetration test and collection of subgrade soil (undisturbed sample). At a later date, repeated triaxial compression tests of the collected subgrade soil were carried out.

Figure 5 shows the distribution of K_{30} values in the depth direction converted from the simple dynamic cone penetration test. The K_{30} value of soft layers up to a depth of 2,500 mm was around 20 MN/m^3, and the K_{30} value deeper than 2,500 mm was about 100 MN/m^3 at the maximum and about 60 MN/m^3 on average.

As a result of conducting soil tests on the collected subgrade soil, the natural water content ratio was w_n 47.7%, the saturation degree was S_r 78.8%, and a plasticity index was I_p 32.4. There was
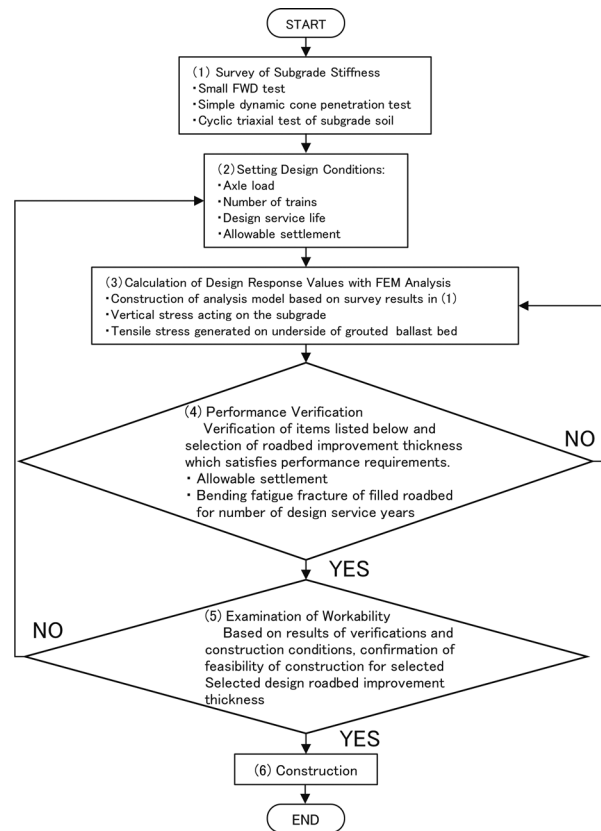
Fig. 3　Design flow
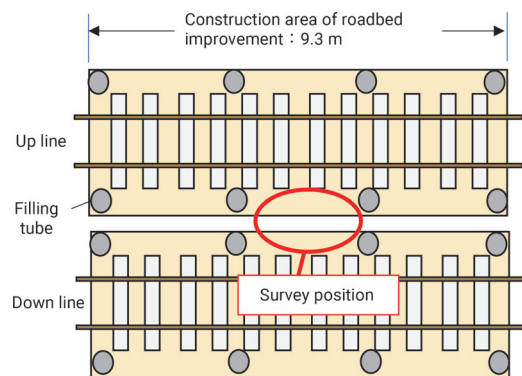
Fig. 4　Construction area of roadbed improvement
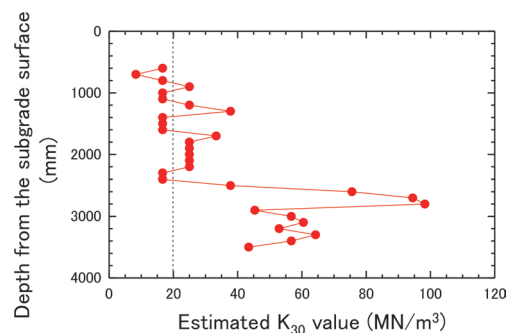
Fig. 5　Distribution of K_{30} value in the depth direction

concern that the strength might decrease as water content increased. On the other hand, as the survey was conducted during the rainy

season, it was considered that the degree of saturation was not always high throughout the year.

Using the undisturbed sample of the collected subgrade soil, repeated triaxial tests (CU) were carried out under a natural water content ratio state (w_n 47.7%). In the test, applied vertical stresses were 15 kPa, 20 kPa, and 25 kPa in total of 3 steps assuming the vertical stress (Train load) acting on the subgrade soil, and the confining pressure was set to 15 kPa, that was taken into consideration the vertical stress acting on the subgrade due to its own weight directly under the labor-saving track. The number of repeated loads in each loading step was 50,000, and the loading frequency was 1 Hz.

Figure 6 shows the relationship between the maximum strain of subgrade soil and the number of loads at each load step. The increment tendency of the maximum strain at each load step can be expressed by the formula in Fig. 6. Furthermore, from the relationship between the estimation formulas $Y = aX^b$ of vertical strain and the vertical stress [8], the relationship between the vertical stress acting on the roadbed and the coefficients "a" and "b" is shown in Fig. 7.

2.3 Setting of design conditions

The design conditions for the construction site are shown below.
・ Annual tonnage: 39 million tons
・ Train conditions
Passenger train: Static axle load 110 kN
Freight train: Static axle load 165 kN
Train speed: 90 km/h
Number of trains: 293 passenger trains / day
2.6 freight trains / day (calculated from 18 trains a week)
Train formation: Passenger 10-car formation 221 trains / day
Passenger 15-car train 72 trains / day
Cargo 25-car train 2.6 trains / day
・ Design service life : 20 years
・ Allowable settlement during the service life: 16 mm

2.4 Calculation of design response value by FEM analysis

Vertical stresses generated on subgrade and bending stresses generated on the lower surface of the grouted ballast bed due to train loads were calculated by FEM analysis using a linear elastic model.

For the load conditions in the analysis, the axle load in the analysis was set to 170 kN, referencing the maximum axle load of freight trains of 165 kN, and two axles were loaded in the center of the model as shown in Fig. 8. The wheelbase was set to 2100 mm, assuming passenger trains. As this analysis was a static linear elasticity analysis, actual loads of passengers and freight trains were used for checking the amount of subgrade settlement. And the actual loads modified by velocity impact rate were used for checking the bending fatigue fractures of grouted ballast bed with respect to the response value obtained in the analysis. The roadbed improvement thicknesses examined in the analysis were 200 mm, 250 mm, 300 mm, 350 mm and 0 mm (no roadbed improvement).

Table 1 shows the physical property values used in the analysis. The elastic modulus of grouted ballast bed was 15000 N/mm² obtained from the uniaxial compression test. The elastic modulus of subgrade was set based on the K_{30} value estimated by the simple dynamic cone penetration test.

Figure 9 shows the relationship between the roadbed improvement thickness and the vertical stresses generated on subgrade surfaces. The vertical stresses on the subgrade surface decreased as the improved thickness increased, and the roadbed improvement thickness of 350 mm decreased subgrade stress by about 39% compared
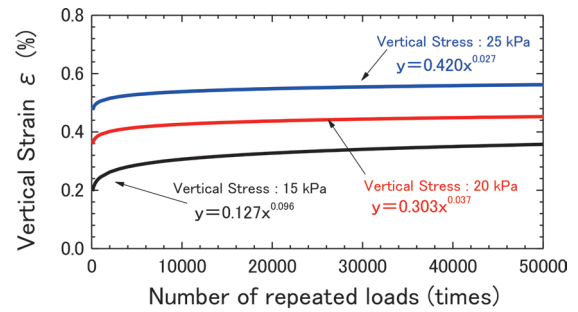
Fig. 6 Formula for estimating maximum strain of each vertical stress
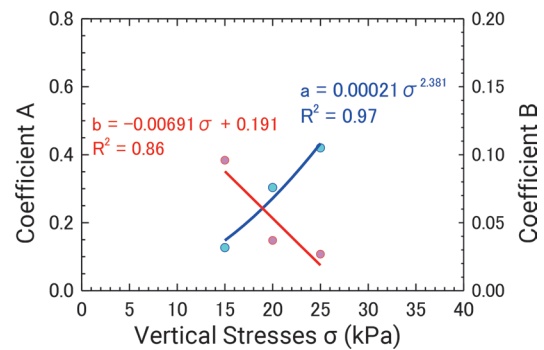
Fig. 7 Relationship between the value of each coefficient and vertical stress
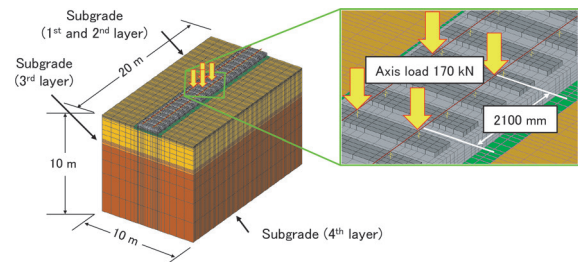
Fig. 8 FEM Analysis model

Table 1 Physical property values used in the FEM analysis

Elements	Elastic modulus (N/mm²)	Poisson's ratio	remark
Rail	210000	0.3	–
Rail pad	–	–	Spring constant of rail pad : 60MN/m
PC sleeper	35000	0.17	–
Filling ballast bed	15000	0.3	Freight line type
Roadbed improvement layer	1000	0.3	–
Subgrade (1st and 2nd layers)	13.5	0.3	Roadbed surface – depth of 2500mm
Subgrade (3rd layer)	47.8	0.3	depth of 2500 mm – 3000 mm
Subgrade (4th layer)	67.8	0.3	Deeper than 3000 mm

to when there was no roadbed improvement. In addition, since there was a soft layer with a K_{30} value of about 20 MN/m³ from the subgrade surface to a depth of 2,500 mm at the construction site, it was
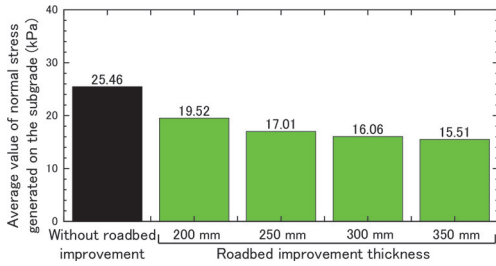
Fig. 9 Vertical stress generated on the subgrade surface
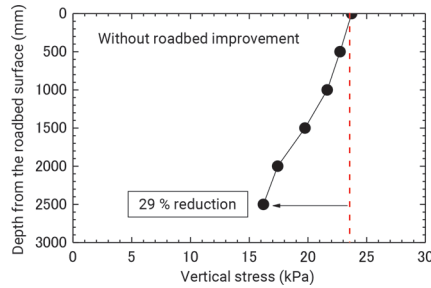
Fig. 10 Distribution of vertical stress in the depth direction
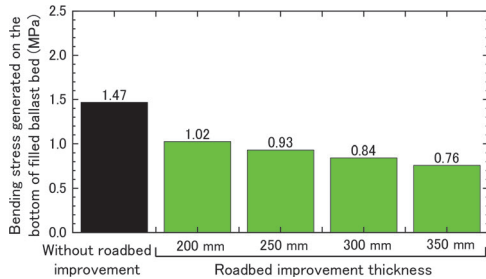
Fig. 11 Bending stress generated in the filled ballast bed
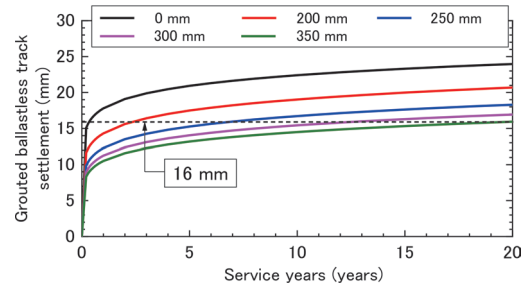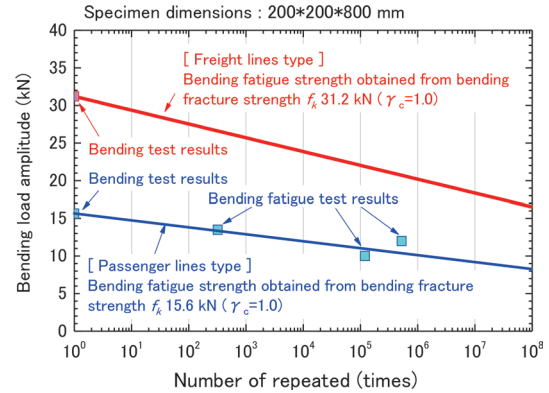

Fig. 12 Estimated grouted ballastless track settlement

Fig. 13 Fatigue strength of filled ballast bed with grout material for passenger trains and freight trains

considered that this layer would be plastically deformed with trains passing repeatedly. Therefore, in order to evaluate the amount of plastic settlement to a high level of accuracy, the distribution of vertical stress in the depth direction at the center position of the track was estimated by FEM analysis (Fig. 10). The vertical stress of the subgrade surface (0 mm) was 23.7 kPa, while the vertical stress at the depth of 2,500 mm was 16.2 kPa, and the vertical stress was reduced by about 29%. Based on this, the amount of the total subgrade settlement was obtained by calculating the amount of settlement of each 500 mm depth from the estimation formula.

Figure 11 shows the relationship between the roadbed improvement thickness and the bending stress generated on the underside of roadbed improvement layers. The bending stress generated on the undersurface of filling ballast layers was reduced as the improved thickness increased, and by applying the improved thickness of 350 mm, it was reduced by about 48% compared to the case without roadbed improvement.

2.5 Performance verification

2.5.1 Verification of settlement

If there are both passenger and freight trains running, it is necessary to estimate the amount of settlement for each train load and accumulate each amount of settlement. In that case, as the large

amount of settlement that occurs at the initial stage of loading is added together, the accumulated amount of settlement would be overestimated. Therefore, in the estimation of the settlement, since the passenger train passed first, it was decided to add the settlement caused by the freight train to the settlement by the passenger train excluding the settlement caused by the first train.

Figure 12 shows the relationship between the amount of the grouted ballastless track settlement at 200 mm, 250 mm, 300 mm, and 350 mm and the service years of grouted ballastless tracks. From the figure, the amount of the subgrade settlement after 20 years of service was 23.97 mm without roadbed improvement, 20.69 mm with improved 200 mm, 18.30 mm with improved 250 mm, 16.94 mm with improved 300 mm, and 15.94 mm with improved 350 mm. According to the verification results, the improved thickness, in which the settlement was within the allowable value of 16 mm after 20 years of service, was 350 mm.

2.5.2 Verification of fatigue fracture of the grouted ballast bed

In order to verify fatigue fracture of the grouted ballast bed, bending tests and bending fatigue tests were conducted using grout materials for passenger trains, which has a lower bending strength than grout materials for freight trains.

Figure 13 shows the test results of grouted ballast bed using grout material for passenger trains and the relationship between the number of repeated loads at fatigue fracture and the load amplitude obtained from the estimation formula [9] for estimating the fatigue strength of concrete. From the figure, the bending fatigue strength of concrete obtained from equations (1) and (2) was in general agreement with the test results. Since the bending fatigue strength of grouted ballast bed can be estimated by applying the estimation formula of the fatigue strength of concrete, the bending fatigue strength of grouted ballast bed using grout material for freight trains

is estimated based on the bending fracture strength of 31.2 kN.

$$f_{crd} = k_{cr} \cdot f_k \cdot \left(1 - \frac{\sigma_{min}}{f_k}\right) \cdot \left(1 - \frac{\log N}{K}\right) / \gamma_c \qquad (1)$$

$$f_b = \frac{P_b \cdot L}{Bh^2} \qquad (2)$$

Where,

f_{crd} : Fatigue strength of concrete
f_k : Strength characteristic value of concrete
K : 17
k_{cr} : 1.0
σ_{min} : Minimum stress
N : Fatigue life (times)
γ_c : Material coefficient of concrete
f_b : Bending strength of concrete
P_b : Destructive load of concrete
L : Distance between fulcrums
B : Width of specimen
h : Specimen height

The fatigue fracture of grouted ballast bed was checked based on the fatigue strength characteristics of grout material for freight lines against the bending stress of grouted ballast bed obtained by FEM analysis. In this check, the number of fatigue fractures when both passenger trains and freight trains pass was calculated with reference to the total number of equivalent repetitions described in "Design standards for railway structures and commentary concrete structures" [9].

In the performance verification, referring to "Design standards for railway structures and commentary track structure" [10], the variable wheel load coefficient uses a velocity impact factor of 1.27, which corresponds to 90 km/h; the wheel load action coefficient is 1.0, the structural analysis coefficient was 1.0, the concrete material coefficient was 1.3, the track component coefficient was 1.1, the track structure coefficient was 1.1. From the performance verification results shown in Table 2, the performance verification result was less than 1.0, and the roadbed improvement thickness that inspection was 350 mm.

2.6 Examination of workability

According to the performance verification results in the previous section, the roadbed improvement thicknesses that satisfied the design conditions in both the settlement and the fatigue fracture was 350 mm. The construction time allowed for this construction was 4 hours from 0:30 to 4:30, and it was necessary to lay the roadbed improvement layers and grouted ballastless tracks after removing the existing grouted ballastless tracks. On the other hand, based on the preliminary construction study, the construction of the roadbed material replacement work per night was taken into consideration for the removal work and laying work of the grouted ballastless track for the total construction length of 18.6 m for the upper and lower lines. It was determined that setting the extension to 4.65 m, would be sufficient to construct a roadbed improvement thickness of 350 mm. Therefore, the design roadbed improvement thickness in this construction was set to 350 mm.

3. Construction and effect analysis on commercial lines

Figure 14 shows images of construction work in progress. For

Table 2 Fatigue fracture verification results

	case1	case2	case3	case4	case5
Roadbed improvement thickness (mm)	0	200	250	300	350
Verification result	1.91 (≧1.0 NG)	1.33 (≧1.0 NG)	1.21 (≧1.0 NG)	1.09 (≧1.0 NG)	0.99 (<1.0 OK)

(a) Excavation of subgrade soil
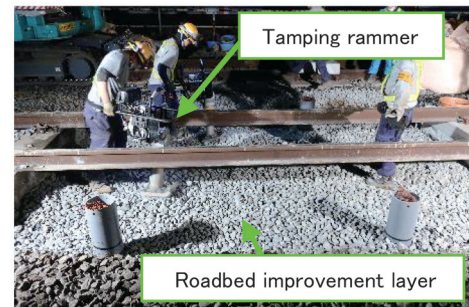
(b) Compaction of roadbed improvement layer
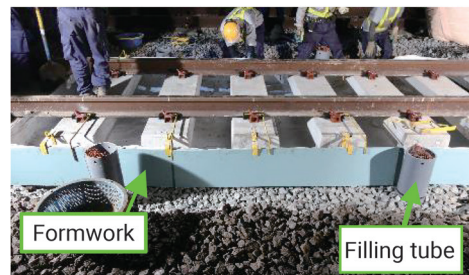
(c) Installation of formwork used for grouted ballastless tracks

(d) Grout filling work

Fig. 14 Construction work in progress

the grout filling work of roadbed improvement layers, the construction length per night was set to 9.3 m (total of 2 days). In replacement work of roadbed material, in order to minimize the settlement of roadbed in the state of ballast tracks, new ballast spread in the improvement area was carefully compacted with a tamping rammer
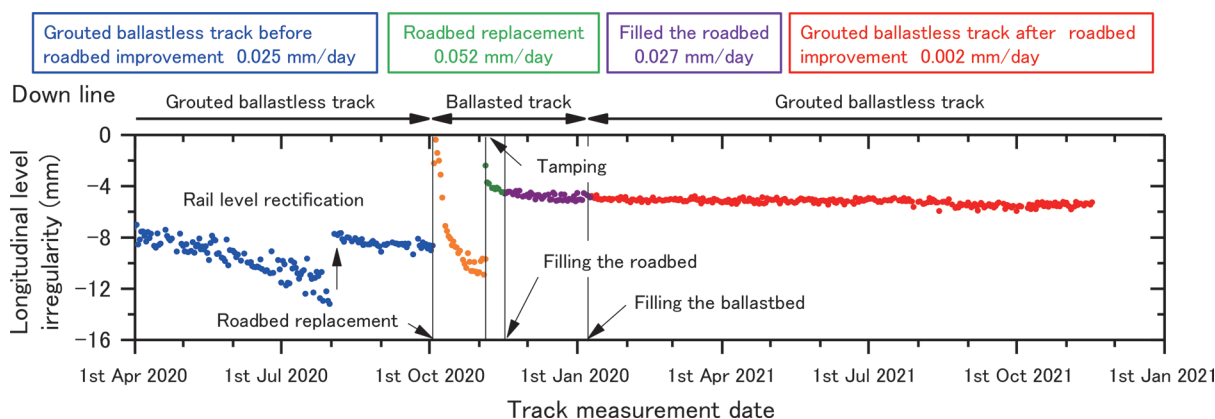
Fig. 15 Longitudinal level irregularity (Down line)
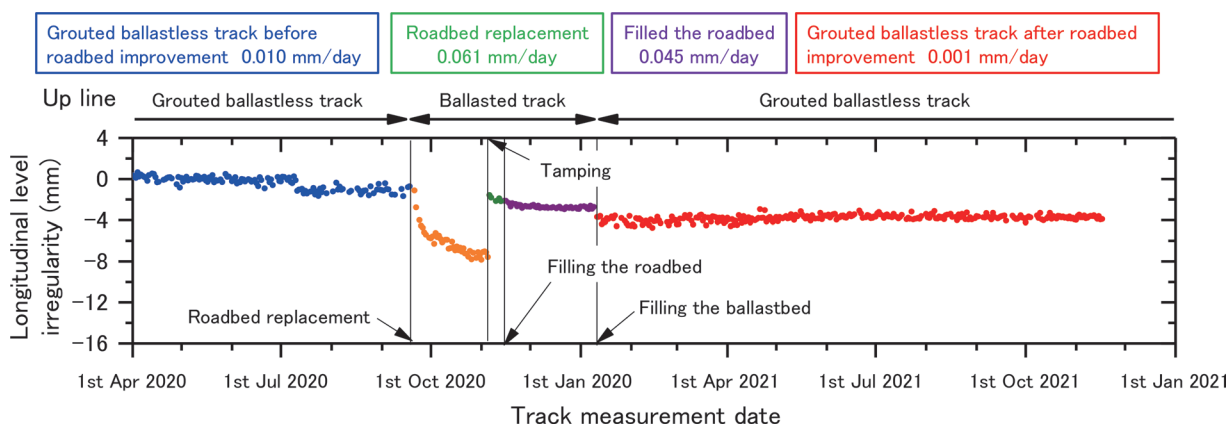
Fig. 16 Longitudinal level irregularity (Up line)

every 1/2 (175 mm) of the roadbed improvement thickness. In grout filling work, filling time for the construction length of 9.3 m was about 1 hour with one set of filling equipment (filling performance: about 400 L/min).

Figures 15 and 16 show the increment of longitudinal level irregularity on the down line and the up line at the roadbed improvement point.

The longitudinal level irregularity increment on the down line was 0.025 mm / day before roadbed improvement (Nov. 2019-Aug. 2020) of the existing line with grouted ballastless track. The condition of the ballast track after replacement of the roadbed (6 days before filling the roadbed) was 0.052 mm / day and after filling the roadbed (6 days after filling the roadbed) was 0.027 mm / day. Therefore, progress in longitudinal level irregularity was reduced by about 48%. The longitudinal level irregularity of the grouted ballastless track (9th. Jan. 2021) after the roadbed improvement was -4.9 mm and -5.3 mm after 10 months of filling, and although the verification period was short, the longitudinal level irregularity advance was about 0.002 mm / day, which was less than 1/10 of that before the roadbed improvement.

The longitudinal level irregularity increment on the up line was 0.010 mm / day (between Apr. 2020-Sep. 2020) before the roadbed improvement of the grouted ballastless track. The ballast track condition after roadbed replacement (9 days before roadbed filling) was 0.061 mm / day, and the ballast track condition after roadbed filling (9 days after roadbed filling) was 0.045 mm / day. Longitudinal level irregularity increments were reduced by about 26%. Furthermore, the average value of longitudinal level irregularity increment

from after roadbed filling to before ballast filling was 0.007 mm / day. The longitudinal level irregularity of the grouted ballastless track (9th. Jan. 2021) after roadbed improvement was -3.7 mm and -3.9 mm 10 months after filling. Like the down line, the verification period was short, but progression in longitudinal level irregularity was 0.001 mm. It improved to less than 1/10 before the roadbed improvement.

4. Summary

The results described in this paper are summarized below.

(1) We have developed a design method for roadbed improvement methods for grouted ballastless track. The roadbed improvement thickness was determined to be 350 mm according to the proposed roadbed improvement thickness design flow by the verification of construction on commercial lines. It was also confirmed that the grout filling roadbed improvement method (post-filling method) allows that roadbed improvement layers and grouted ballastless tracks are implemented at the same time without any problem.

(2) The effect of improving the roadbed shows that the amount of longitudinal level irregularity increment was reduced to 1/10 or less on both the upper and lower lines when compared before and after the roadbed improvement. Based on current longitudinal level irregularity and longitudinal level irregularity increment, it is expected that the longitudinal level irregularity after 20 years can be suppressed to within 16 mm.

References

[1] Research Group of maintenance-free Ballast Track, "Development of A new Track System with Asphalt Treating Method – A Track Strength Method of the Preconstructed Service Track –," *Railway Technology Research Report*, No. 862, 1973 (in Japanese).

[2] Nagafuji, T., Tsumenaga, T., Tada, I., "Characteristics of impregnation material named PTCAM for E-type paved track," Railway Technical Research Institute, No. A-83-56, 1983 (in Japanese).

[3] Hojyo, T., "Efforts for Phase 2 TC-type grouted ballastless track construction," *Shinsenro*, Vol. 57, No. 7, pp. 8-11, TetsudoGengyosha, 2003 (in Japanese).

[4] Hori, Y., Hagio, Y., Iwata, M., Arima, S., "Development of orbital subsidence repair method by interval pressure injection," *65th JSCE Annual Meeting*, 2010.9 (in Japanese).

[5] Hagio, Y., Kubomura, K., Sekiguchi, A., "Implementation of measures for defective drainage points in TC-type labor-saving tracks," *63rd JSCE Annual Meeting*, 2008.9 (in Japanese).

[6] OMODAKA, A., KUMAKURA, T., KONISHI, T., "Influence of road condition and soil consistency on track irregularity advance," *Railway Engineering-2017*.

[7] Ito, K., Momoya, Y., Kijiya, I., Takahashi, T., "Study on deformation characteristics of existing line ballastless tracks applying roadbed improvement," *JSCE Proceedings E1 (Pavement Engineering)*, Vol. 76, No. 2, I_305-I_313, 2020 (in Japanese).

[8] Ito, K., Momoya, Y., Kijiya, I., "Development of Roadbed Improvement Method that can be Constructed Simultaneously with Existing Ballastless Track," *Railway Technical Research Institute Report*, Vol. 34, No. 4, 2020 (in Japanese).

[9] Railway Technical Research Institute, *Design standards for railway structures and commentary Concrete structures*, 2004 (in Japanese).

[10] Railway Technical Research Institute, *Design standards for railway structures and commentary Track Structure*, 2012(in Japanese).

Authors

Kazuki ITO, Dr. Eng.
Senior Researcher, Track Structures and Geotechnology Laboratory, Track Technology Division
Research Areas: Ballasted Track
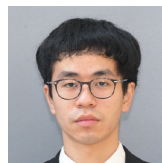
Takahiro KAGEYAMA, Dr. Eng.
Researcher, Track Structures and Geotechnology Laboratory, Track Technology Division
Research Areas: Ballasted Track

Yoshitsugu MOMOYA, Dr. Eng.
Director, Head of Track Technology Division
Research Areas: Ballastless Track, Ballasted Track

Estimating the Physical and Mental State of Drivers Using Physiological Indicators

Chizuru NAKAGAWA
Human Science Division

Takahiro WATANABE
Ergonomics Laboratory, Human Science Division (Former)

Naohiro AKIU   **Ayako SUZUKI**
Ergonomics Laboratory, Human Science Division

Takashi KOJIMA
Vehicle Dynamics Laboratory, Vehicle Technology Division

Sachiko YOSHIE
Comfort Science and Engineering Laboratory, Human Science Division

Using physiological data from a basic experiment simulating railroad driving in general participants, we studied a method for detecting mental and physical states that may interfere with driving. As a result, characteristic changes in brain activity are observed in the group that experienced a psychological upset. In addition, we selected heart rate and respiration as physiological indices that can be easily measured during driving and proposed a method for selecting effective indices for estimating mental and physical states for each individual. We examine the relationship between brain activity associated with psychological agitation and a questionnaire score on resilience (ability to adapt well) and found a weak correlation between them.

Key words: *brain activity, state estimation, autonomic index, resilience, driver, arousal level*

1. Introduction

The purpose of this study is to support drivers in sensing their mental and physical states to help them avoid mental and physical states that may lead to serious accidents. The physical and mental states that can impede appropriate behavior and judgment include impaired consciousness due to illness, excessive tension such as psychological agitation, and decreased arousal level such as drowsiness. This study considers psychological agitation (excessive tension) and decreased arousal level.

The Railway Technical Research Institute (RTRI) has built a system for measuring biological information and behavior, including a multipoint electroencephalograph (MEG), and has conducted experiments with subjects using a railway driving simulator [1]. As a result, characteristic changes in brain activity in the prefrontal cortex, pupil diameter, heart rate, and respiration that occur when psychological agitation occurs were captured, but the patterns of these changes varied greatly among individuals and overcoming this problem of individual differences was an issue to obtain detection accuracy that would be sufficient for future goals.

Therefore, the present study aimed to estimate tension using practical physiological indices based on a multifaceted view of the physio-pathological characteristics of psychological agitation. First, we investigated the relationship between psychological agitation and physiological changes and personality traits [2]. In addition, we examined practical physiological indices suitable for detecting changes in the state of tension and methods for solving the problem of individual differences [3, 4]. In addition, when the state of tension is considered in relation to the arousal level, over-tension is positioned as an excessive increase in the arousal level, and its opposite is a decrease in the arousal level (non-tension to drowsiness). Therefore, over-tension and non-tension were considered as the detection targets.

2. Examination of brain activity and psychological characteristics during psychological agitation

In the authors' study using a driving simulator, the θ- and α-wave components of the prefrontal EEG tended to be attenuated in participants who delayed emergency brake operation due to psychological agitation caused by the detection of obstacles on the track. However, it was difficult to verify the relationship between brain activity and psychological agitation in this experiment because of the complexity of brain stimuli such as mass control operation and visual information from the forward-facing image.

Therefore, we conducted a basic experiment in which psychological agitation was induced by sudden sound stimuli during a task using a cognitive task that abstracted the driving task and investigated the relationship between performance results such as the percentage of correct answers in the experiment and questionnaire responses regarding physiological indices and personality [2].

2.1 Experimental details

2.1.1 Experimental system and participants

Figure 1 shows the experimental setup. The experimental apparatus consisted of a 50-inch monitor, a keyboard for operation, and a PC for task control. The physiological data were measured as electroencephalogram (EEG), electrocardiogram (ECG), respiratory waveform and pupil diameter using 128-channel high-density EEG electrodes.

The participants were 16 ordinary men (mean age: 27.8 years), and their consent to participate in the experiment was obtained after adequately explaining the experiment before the start of the experiment. The experiment was conducted with the approval of the Eth-

ics Review of Human Life Engineering Experiments by the Research Institute of Human Engineering for Quality Life (Ethics approval number H30-23-1e).

2.1.2 Experimental Tasks

A train driver, using sight while the train is in motion, is able to gather information on the direction of travel, detect signal and signs, and continue driving while adjusting the line of sight as necessary.

In this experiment, two tasks (a central vision task and a peripheral vision task) symbolizing an actual driving situation were performed simultaneously. The contents of each task were as follows.

[Central vision task] A circular white frame was constantly displayed in the center of a black screen. Whenever a white number (1 to 3) appeared randomly inside the frame, the operator pressed the key with the same number as soon as possible.

[Peripheral vision task] Whenever a blue or red ● was shown in one of the four corners of the screen, the operator pressed a key of the same color.

The participants were instructed to keep their gaze within the white frame in the center of the screen during the task and to perceive the circles in the four corners with peripheral vision. During the task, pink noise (about 40 dB) was played into the earphone of the participants to the experiment to mask ambient sound.

The duration of one trial was 3 minutes. After two practice trials, 12 trials (T1 to T12) were conducted as the main task. At the end of each trial, the participants responded to a questionnaire on self-evaluation and level of concentration. Psychological agitation was induced by playing 75 dB white noise (sound stimulus) for 0.5 s after 120 s from start of trial only for T7 and T11 trials.

Fig. 1   Experimental setup

2.1.3 Personality traits survey

Before the experiment began, a survey using a personality questionnaire, the "NEO-FFI" [5], was conducted. This questionnaire was designed to investigate individual characteristics regarding five personality traits (openness to experience, conscientiousness, extraversion, agreeableness, and neuroticism).

In addition, the "Stress Tolerance Checklist" [6] and the "S-H Resilience Test" [7] were conducted as follow-up surveys two years after the experiment was conducted. The purpose of this was to verify the difference between those who were susceptible to the sound stimuli and those who were not. These two groups were identified from the results of the experiment described in section 2.2. The "Stress Tolerance Checklist" was designed to measure the degree of tolerance to stress and consisted of 20 questions on a 4-point scale. The "S-H Resilience Test" is a test of the ability to recover from stress (resilience) and consists of 27 questions on a 5-point

scale in Part 1 and 8 questions on a 4-choice scale in Part 2. It is composed of three factors of social support (how the person feels about the degree of support and cooperation from those around him, such as family, friends, colleagues, etc.), self-efficacy (how the person feels about the degree of problem-solving, etc.), and sociability (how the person feels about the degree of affinity and cooperation in dealing with others). The higher the score, the higher the resilience.

2.2 Experimental results

2.2.1 Grouping by reaction time and percentage of correct responses

To investigate the effects of the sound stimuli on the performance of the participants in the experiment, we examined the reaction time and the percentage of correct responses to the peripheral vision task immediately after the sound stimulus. To account for individual differences, the reaction time to the task immediately after the sound stimulus was divided by the average reaction time to the task from T1 to T6 for each participant and was calculated as the "percentage of delayed reaction."

The participants were grouped by the percentage of correct responses immediately after the sound stimulus. Participants who answered correctly in both sessions of the task were classified as group A, those who answered incorrectly in either session were classified as group B, and those who answered incorrectly in both sessions were classified as group C. The results of the percentage of delayed responses for each group are shown in Fig. 2(a).

In addition, to examine the persistence of the sound stimulus effect, when the error rate in the 20 seconds post-stimulus was examined, the error rate of group C was found to be the highest (Fig. 2(b)). This result suggested that, for the group whose performance on the task decreased immediately after the sound stimulus, performance continued to decrease after the sound stimulus.

2.2.2 Differences in EEG changes in performance groups

To examine the transition of EEG changes immediately after sound stimulus, we examined the power spectral density (PSD) changes every 0.5 seconds in each of the three bands of θ, α, and β. The change was the difference between the PSD for 5 s after the sound stimulus and the mean value for 120 s before the sound stimulus, divided by the mean PSD for T1 to T6. The results showed that there was no clear change immediately after the sound stimulus in groups A and B, but there was a tendency for the frontal β-band component to decrease in group C after the stimulus (Fig. 3).

The prefrontal cortex is an area that controls memory and mental activity, and β waves predominantly appear in areas of the brain with brisk mental activity [8] and have been reported to increase during states of concentrated tension [9, 10]. Therefore, the decrease in β wave intensity in the present experiment likely indicate a state of reduced concentration and distraction to the task induced by sound stimulus, which may have worsened performance in the task.

2.2.3 Results of analysis of heart rate, pupil diameter

In participants with a significant decrease in the β-band component of the EEG, the heart rate tended to increase temporarily immediately after the sound stimulus, but no characteristic change was observed in the other participants.

Pupil diameters expanded more after the sound stimulus rather than before the stimulus for all participants. While it took more than

(a) Percentage of delayed responses (b) Error rate
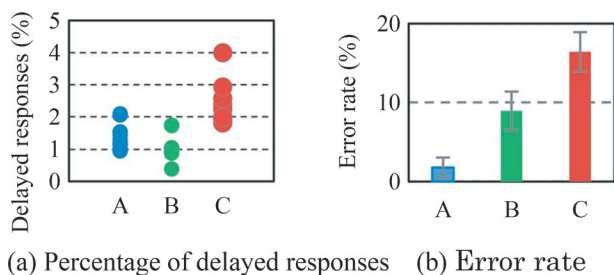
Fig. 2 Performance results by group

Fig. 3 Changes in three frequency bands of brain waves by group after sound stimulus

one minute after the sound stimulus to return to the pre-stimulus pupil size for the participants whose heart rate increased temporarily, the pupil size returned to the pre-stimulus pupil size approximately 10 seconds after the sound stimulus for the other participants. This result is consistent with the previous simulator experiments [11].

2.2.4 Results of the personality traits questionnaire

There were no correlations between groups or EEG in the five factors of the NEO-FFI personality questionnaire. Stress tolerance is considered to be weak when the score is less than 40 and strong when it is greater than 50 in the stress tolerance checklist, but no participant had a score less than 40. Moreover, there were no differences between groups.

For the S-H resilience test factors, changes in β-intensity after sound stimulation were compared among the groups (Fig. 4). The results showed a weak positive correlation (correlation coefficient 0.50) between self-efficacy scores and changes in EEG β-intensity. This likely suggest an association between low self-efficacy and a marked decrease in β-intensity in group C. However, due to the small sample size, further validation of this association is required.

3. State estimation by physiological indices for practical use

For future use in the driver's seat, physiological indices that are resistant to noise and can be easily measured are desirable. For this reason, use of autonomic physiological indices that can be measured relatively easily was investigated [3, 4].

3.1 Selection of suitable physiological indices for estimating driver status

The autonomic nervous system unconsciously acts "autonomously," to sustain homeostasis of the living body, and consists of two systems, the sympathetic nervous system, and the parasympathetic nervous system [12]. When the sympathetic nervous system is activated, it works to increase the body's activity level and athletic performance by increasing the heart rate, blood pressure, and respiratory rate, and is generally considered to indicate a state of tension or stress. In contrast, the parasympathetic nervous system suppresses the activities of heart rate, blood pressure, and respiration, and invigorates the activities of the digestive system to calm the body and mind, suppress energy consumption, and store energy, which is generally considered to indicate a relaxed state. However, there is also a stereotactic response in which the parasympathetic nervous system is activated when concentrating on gathering information about the outside world in the face of a certain situation [12], and it does not strictly indicate a relaxed state only.
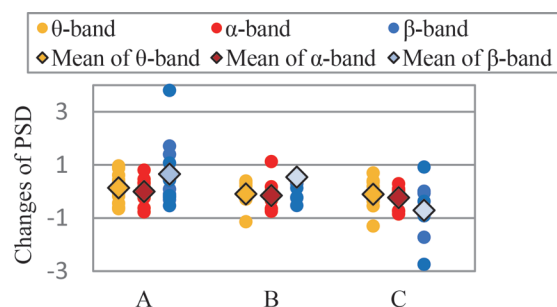
Since the state of activation of the autonomic nervous system reflects tension and stress, it is highly likely to be effective in detecting psychological agitation (over-tension), which is the purpose of this study. Although heart rate, blood pressure, respiration, psychogenic sweating, and pupillary system changes are physiological indices of autonomic nervous system activity, heart rate and respiration are considered appropriate in terms of practicality, such as stability and simplicity of measurement. For this reason, this section discusses a method for estimating the state of tension from heart rate and respiration.

3.2 Physiological indices based on heart rate and respiration

Typical physiological indices obtained from heart rate are heart rate (HR) and autonomic indices LF and HF [13, 14]. LF is said to reflect both sympathetic and parasympathetic nervous system activity, while HF reflects parasympathetic nervous system activity, and most wearable devices in recent years utilize these indices.

Although there are several methods of measuring respiration, in this study, the changes in abdominal circumference were measured as respiratory waveforms in consideration of the realization of simple measurement in the future. The physiological indices obtained from this respiratory waveform are (1) respiratory interval, (2) respiratory amplitude, and (3) respiratory variability.

Of LF and HF, HF (0.15-0.40 Hz component of heart rate variability) derived from the parasympathetic nervous system is easier to grasp the autonomic nervous system activity than LF (0.05-0.15 Hz component of heart rate variability), which is affected by both the sympathetic nervous system and the parasympathetic nervous system. Therefore, HF is mainly considered here.

The bandwidth of HF is wide because it captures the respiratory cycle component of the heart rate variability. This is because respiratory sinus arrhythmia (RSA), a respiratory-synchronized component of heart rate variability, reflects parasympathetic nervous system activity, and HF is set to cover the bandwidth where RSA is likely to appear. However, the respiratory cycle fluctuates greatly on a daily basis due to speech, deep breathing, resting and exercise, etc. In the case of very slow breathing, RSA may appear in the LF band. Therefore, although respiration should be taken into account to detect RSA, heart rate alone is easier to measure, and in most cases, RSA is calculated from heart rate variability without measuring respiration. In this study, we analyzed both heart rate and respiration, and investigated a method to capture the RSA-derived component of heart rate variability more accurately than the conventional HF method. As an example of the correspondence between heart rate variability and respiration, the measurement data is shown in Fig. 5.

The upper row shows the heart rate variability (HRV), the mid-
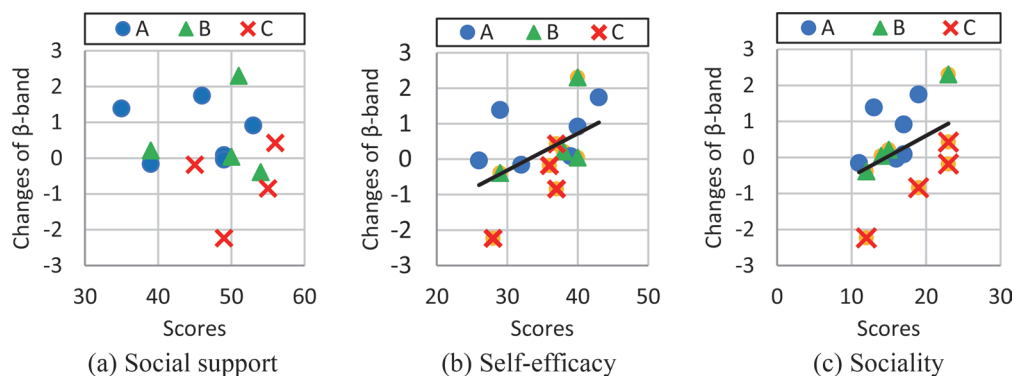
Fig. 4 Comparison of EEG changes and 3-factor scores in the S-H resilience test

dle row shows the respiratory waveform, and the lower row shows the RSA (calculation method described later) and respiratory waveform. The circular markers (○) on HRV in the upper row correspond to the inspiratory points of respiration (the minimum value of the respiratory waveform in the middle row), indicating that the phases of the HRV waveform and respiratory waveform are reversed.

For RSA extraction utilizing respiration, Kotani et al., proposed a method focusing on respiration information [15]. Although the details are omitted here because of manuscript limitation, Kotani et al., demonstrated the validity of RSA extraction by heart rate variability (HRV) analysis using respiratory cycle, and defined the RSA component as "the difference between the HRV values when respiration showed maximal and minimal values." However, respiratory measurement using abdominal circumference is easily affected by posture and other factors, and the maxima are unclear in slow breathing. Therefore, in this study, the RSA component RC (see below) was defined as the difference between the maximum and minimum values of one respiratory segment starting and ending at the inspiratory start point of breathing [3].

HRV: Heart rate variability   RSP : Respiration waves,
INT : Interval of respiration   RC: RSA components
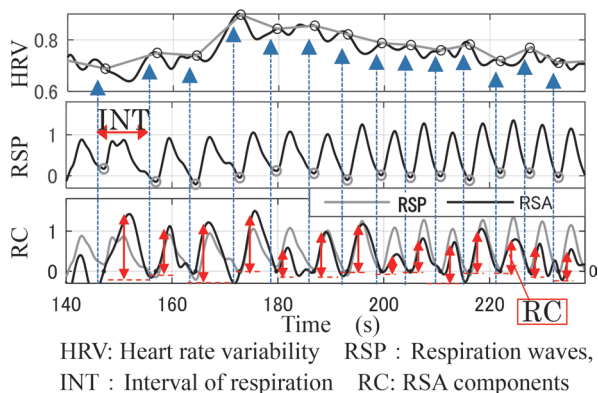
Fig. 5 Relationship between heart rate variability, respiration, and RC

3.3 Experiment overview

3.3.1 Experimental system and participants

Ten healthy adult men (mean age 32.4 years, standard deviation 7.4) participated in the experiment using a simple driving simulator that simulated train driving. Prior written and verbal explanations were provided to the participants and consent was obtained for participation in the experiment, which was conducted for a fee.

3.3.2 Measurement Items

For physiological indices, electrocardiogram (ECG) using CM5 chest leads, respiratory waveform by chest circumference change, and electroencephalogram (EEG) and pupil diameter by 128-channel high-density EEG electrodes were measured 1), but only ECG and respiratory waveform data were used in this paper for analysis.

For subjective evaluation, a cue tone was sounded every 30 seconds during the experiment, and the subjects answered their arousal level at that time, on a 5-point scale (1: feeling drowsy, 2: feeling a little drowsy, 3: normal, 4: feeling a little tense/agitated, 5: feeling tense/agitated), by pressing the right-hand button.

3.3.3 Experimental tasks

The participants performed three types of tasks: a proficiency task, an obstacle on track task, and a time pressure task, which are described below. In each of these tasks, the participants performed a 10-minute trial in which they drove between four stations. In the above trials, the train always stopped for 90 seconds at the first station and the last station (Rest ①, Rest ②). The participants were instructed to drive according to the timetable and within the prescribed speed limit. In the proficiency task, seven trials were conducted to familiarize the participants with the driving operation (T1~T6 in the morning, T7 in the afternoon). Thereafter, four trials (T8, T10~T12) were conducted as task on obstacle on the railway track. The task was the same as the training task except that a car entered the railroad crossing on the way. T8 was conducted without any prior information, while T10 to T12 were conducted with prior information about the entry of the car. In between T8 and T10, trial T9 was conducted without any car entry. Next, a time pressure task (T13 to maximum T18) was conducted. In this trial, the train was driven according to a timetable with almost no spare time. If the participant was able to arrive at the last station on time, he or she was excused from the rest of the task (no more trials), but when unable to do so, continued to perform trials up to the maximum of T18. The breaks between tasks were 3 to 5 minutes depending on the participants' conditions, and a 15-minute break was taken every three tasks. A 15-minute break was taken every three tasks. A 45-minute lunch break was also taken between T6 and T7.

The number of trials of the time-pressure task varied depending on the participants' achievement level, with a minimum of 13 trials and a maximum of 18 trials. The total number of trials was 151, but 14 trials were incomplete due to blue-tooth interference between the measurement devices, and the following analysis was conducted on 137 trials.

3.3.4 Data analysis of heart rate and respiration

The main physiological indices of heart rate and respiration and their calculation methods are described below.

(1) Heart rate interval RRI: Time interval between ECG peaks (successive R wave)

(2) Heart rate variability HRV: Calculated by spline interpolation after plotting RRI at the beat midpoint (Fig. 5 upper row)

(3) Parasympathetic nerve index HF: FFT processing of HRV for 30 seconds and addition of PSD in the 0.15-0.40 Hz band

(4) Respiration length INT: Time interval at the start of inspiration of breath, Trsp (circular markers in the middle row of Fig. 5)

(5) Respiratory sinus arrhythmia RSA: HRV at Trsp time point, calculated from HRV by subtracting the linear interpolation waveform and inverting the positive and negative.

(6) Parasympathetic index RC: difference between maximum and minimum RSA per breath (Fig. 5, arrows in bottom row)

To reduce the influence of individual differences in the physiological indices, each index was standardized by a robust Z-score (the difference between the measured value and the median divided by the interquartile range IQR). The median and IQR used for standardization were obtained from the proficiency tasks T2 to T6 excluding T1. Each physiological index value was calculated for each respiratory cycle.

3.4 Experiment results

3.4.1 Validation of RC

The relationship between HF and the subjective rating scale of RC was examined. Since the subjective evaluation was performed with intermittent data on responses given every 30 seconds, the sections corresponding to the subjective evaluation scale 1~5 were cut out as 10 s intervals covering ±5 s at the time point of response and analyzed. Figure 6 shows the rate of occurrence of increase within the interval for subjective evaluation scale, where "increase" was judged when HF and RC were more than ½ (the change is more than ½ of IQR). If the increases in HF and RC reflect parasympathetic activation, they should be caused mainly by a decrease in arousal level.

In Fig. 6, for both HF and RC increase judgments, the lower the subjective evaluation scale, the higher the rate of occurrence (non-tension state), and this tendency was more pronounced in RC. This confirmed the validity of the RC as a parasympathetic index [3].

3.4.2 Dealing with the problem of individual differences in physiological changes

As mentioned above, changes in physiological indices during daily-life activities are difficult to quantify and judge due to large individual differences. However, it is necessary to quantify physiological indices and realize change judgments with high accuracy to detect inappropriate states for driving and to generate alerts. Accordingly, we studied a method for estimating the state of tension by selecting physiological indices effective for each individual [4].

To select an effective index, it is necessary to examine the changes in the index under different tension conditions. Since it is difficult to obtain subjective evaluation in actual operational situations, "situation in which the arousal level is likely to decrease (non-tension interval)" and "a situation that tends to cause strong tension (tension interval)" were used. The rest intervals (90-second stop at the first station and the last station) in the T3 ~T7 trials where
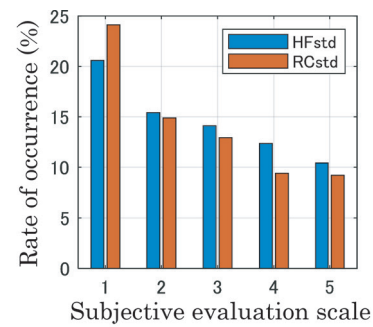
HFstd: Standardized HF   RCstd: Standardized RC

Fig. 6   Rate of occurrence of increase within the interval for subjective evaluation scale

the participants were familiar with the task, were selected as non-tension intervals. The stop operation interval (20 seconds just before the station stop) in the first T1-T2 trials and the time pressure task T13~T18 trials were selected as the tension intervals. The five candidate valid indices were heartbeat interval, respiratory interval, RC, heartbeat regularity, and respiratory regularity obtained from heartbeat and respiration data. The threshold for determining the increase/decrease of each indicator was ± IQR/2. For heartbeat regularity and respiratory regularity, when the difference between all four consecutive index values was less than IQR/2, it was judged as "constant," and when the difference was greater than IQR/2, it was judged as "variable." Table 1 shows the correspondence between the change in each index and the tension/non-tension state.

Based on this condition, valid indices were selected for each participant in the experiment (Table 2). In the same table, the physiological index selected as an effective index for each participant is indicated by ●, and its color indicates whether it was selected as a tension or non-tension index. This result shows that the effective indices differed among the participants. In particular, respiratory interval was selected as a valid index for all participants, and heartbeat variability and RC were selected as valid indices for 6 out of 10 participants, suggesting that measuring heart rate and respiration is effective for state estimation. In addition, one of the physiological indices was selected as either a tension or a non-tension indicator for all participants. This means that both tension and non-tension can be determined using the indices.

Based on the selected valid indices, we verified the estimability of the tension/non-tension state for each participant. When a change was judged to have occurred in any of the valid indices for each participant in Table 2, it was considered to be a "change," and this was considered to be the "overall judgment." The results are shown in Fig. 7. The vertical axis of the figure shows the occurrence rate of judgments in the tension and non-tension intervals, with the blue bar representing the non-tension judgments and the red bar representing the tension judgments. The results are for 10 participants, where

Table 1   Five candidate valid indices

No	Index	Significance	Non-tension	Tension
1	RRI	Heartbeat interval (s)	Increase	Decrease
2	INT	Respiratory interval (s)	Increase	Decrease
3	RC	Peak to peak of RSA	Increase	Decrease
4	RRIR	Heartbeat regularity	variation	Constant
5	INTR	Respiratory regularity	variation	Constant

Table 2 Results of valid indices selected for each participant

Participant ID	1	2	3	4	5	6	7	8	9	10
RRI	🟢		🔵	🔵	🟢			🔴		
INT	🟢	🟢	🟢	🔵	🔵	🔵	🔵	🔵	🔵	🔵
RC			🔵	🔵	🔵	🔴	🔵	🔵	🟢	🟢
RRIR				🔴			🔴		🔴	🟢
INTR			🔴		🔵	🟢	🟢		🟢	🔵

🔵 : Non-tension index　🔴 : Tension index
🟢 : Non-tension/tension index

RO:Rate of occurrence　TI: Tension interval
NTI: Non-tension interval
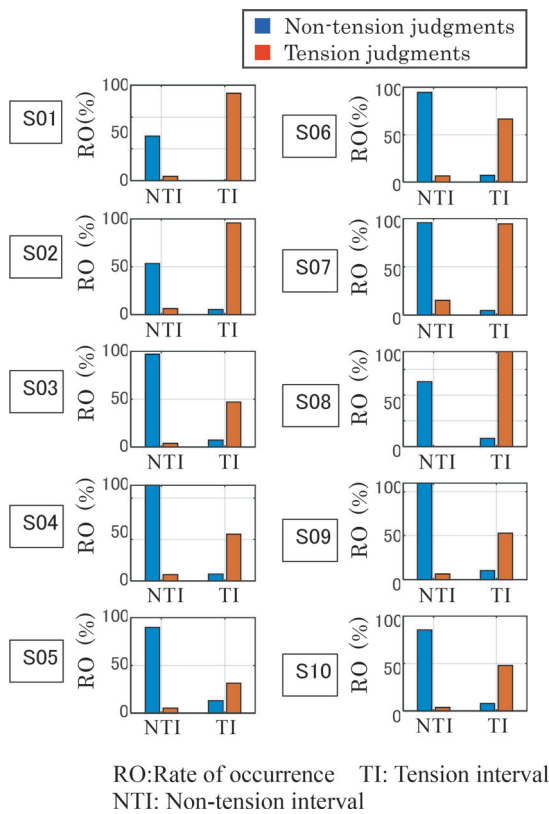
Fig. 7 Occurrence of non-tension and tension judgments by participant

many occurrences of tension judgement in the tension intervals, and of non-tension judgement in non-tension intervals were observed, and the true positive rate was more than 50% in nine out of ten participants.

On the other hand, the false positive rate was less than 15% for all participants. These results suggest that the proposed method of selecting an effective index for each individual from the five indices obtained from heart rate and respiration measurements is effective for estimating the state of tension.

4. Conclusions

To capture the physiological and psychological characteristics of psychological agitation, we investigated the relationship between physiological changes including changes in brain activity, and individual characteristics. The results showed that the group exhibiting decreased performance due to psychological agitation exhibited more characteristic changes in the prefrontal cortex, and the participants with more pronounced EEG changes showed increased heart rate and persistent pupil dilation. On the other hand, the results of the association between the answers to questionnaire on several personality traits and the performance and EEG changes showed that the resilience (ability to cope appropriately) score was weakly positively correlated with the aforementioned characteristic EEG changes. This suggest that low ability to cope with changes in circumstances likely lead to psychological agitation, but further validation is needed because of the small number of participants in the experiment.

Next, to select physiological indices with an emphasis on practicality and to solve the problem of reduced estimation accuracy due to individual differences, we proposed a method of selecting valid indices suitable for tension estimation for each individual from five indices for heart rate and respiration, which can be measured easily. In addition, when the non-tension state and the tension state were estimated by combining the valid indices, both tension states could be detected with an error rate of less than 15% (less than 11% in nine participants) in all ten participants.

In the future, we would like to propose a system to support the driver by combining simple measurement technique for physiological indices using a wearable device and the results of this study.

References

[1] Nakagawa, C., Akiho, N., et al., "Basic Study on Estimation of Driver Status Using Physiological Indicators," *RTRI Report*, Vol. 33, No. 1, pp. 5-10, 2019 (in Japanese).

[2] Watanabe, T., Nakagawa, C., Suzuki, A., "Frequency modulation of EEG and comparison of individual characteristics during psychological agitation task," *Ergonomics*, Vol. 57, Supplement No. 1, G1-02, 2021 (in Japanese).

[3] Nakagawa, C., Watanabe, T., et al., "Examination of estimation of driver's psychosomatic state utilizing simple respiratory sinus arrhythmia component estimation," *Ergonomics*, Vol. 56, Supplement, No. 2, G1-02, 2020 (in Japanese).

[4] Nakagawa, C., Suzuki, A., et al., "Estimation of Strong Tension State Using Multiple Physiological Indices Optimized for Each Individual," *Ergonomics*, Vol. 58, No. 2, pp. 84-95, 2022 (in Japanese).

[5] Shimonaka, Y., Nakazato, K., ek al., "*NEO-PI-R, NEO-FFI manual for the Japanese version*," Tokyo Psychology Co., Bunkyo, Tokyo, Japan, 1999 (in Japanese).

[6] Oritsu, M., Yokoyama, H., et al., "Reliability of a Stress Tolerance Check List (The 2nd Report)," *Japanese Society of Psychosomatic Medicine*, Vol. 39, No. 8, pp. 595-602, 1999 (in Japanese).

[7] Sato, T. and Sukemune, S., "A trial for standardization of the resilience scale: development and reliability/validity check of the S-H resilience scale (part 1)," *Japanese journal of nursing research*, Vol. 42, No. 1, pp. 45-52, 2009 (in Japanese).

[8] Yamaguchi, Y. and Yamaguchi, H., "Comparison of learning task solving process by frequency analysis of EEG," *Bulletin of the Center for Educational Practice*, Okayama University, No. 1, pp. 59-67, 2001 (in Japanese).

[9] Hioki, M., Nozawa, A. et al., "Physiological and Psychological

Evaluation of Mental Workload under Time Pressures," *IEEJ Transactions* C, Vol. 127, No. 7, pp. 1000-1006, 2007 (in Japanese).

[10] Mizuno, Y., Tanaka, Y., et al., "Quantitative analysis of EEG and pulse wave related to work environment during mental workload," *Biomedical Engineering*, Vol. 48, No. 1, pp. 11-24, 2010 (in Japanese).

[11] Akiu, N., Nakagawa, C., et al., "Basic study of pupil diameter change in psychological agitation during railway driving tasks," *Proc. of Human Interface Symposium 2016*, Tokyo, Japan, Sep., 6-9, pp. 359-362, 2016 (in Japanese).

[12] Ohsuga, M., "Introduction to Physiological Experiments (4 times) No. 4 Measurement of Autonomic Nervous System Indicators," *Journal of Human Interface Society*, Vol. 7, No. 4, pp. 285-290, 2005 (in Japanese).

[13] Saykrs, B. McA., "Analysis of Heart Rate Variability," *Ergonomics*, Vol. 16, Issue 1, pp. 17-32, 1973.

[14] J. Hayano, J., Yamada, M., et al., "Heart rate variability and autonomic function," *Biophysics*, Vol. 28, No. 4, pp. 32-36, 1988 (in Japanese).

[15] Kotani, K., Hidaka, I. et al., "Analysis of respiratory sinus arrhythmia with respect to respiratory phase," *Methods Inf. Med.*, 39, 153-156, 2000.

Authors

Chizuru NAKAGAWA, Dr. Eng.
Senior Chief Researcher, Human Science Division
Research Areas: Ergonomics, Physiological and Psychological Engineering

Takahiro WATANABE
Researcher, Ergonomics Laboratory, Human Science Division (Former)
Research Areas: Ergonomics

Naohiro AKIU
Assistant Senior Researcher, Ergonomics Laboratory, Human Science Division
Research Areas: Ergonomics, Human Interface, Safety Engineering

Takashi KOJIMA, Dr. Eng.
Assistant Senior Researcher, Vehicle Dynamics Laboratory, Vehicle Technology Division
Research Areas: Mechanical Engineering

Sachiko YOSHIE, Dr. Eng.
Senior Researcher, Comfort Science and Engineering Laboratory, Human Science Division
Research Areas: Molecular Biology, Environmental Microbiology

Ayako SUZUKI, Dr. Litt.
Assistant Senior Researcher, Ergonomics Laboratory, Human Science Division
Research Areas: Occupational Health Psychology and Ergonomics

Evaluation of Environmental Hygiene in Railway Vehicles Using Microbiome Analysis

Sachiko YOSHIE   **Masateru IKEHATA**   **Tamami KAWASAKI**
Takashi KYOTANI   **Tomoyoshi USHIOGI**
Comfort Science and Engineering Laboratory, Human Science Division

To evaluate environmental hygiene, we introduce a microbiome analysis that comprehensively and qualitatively grasps types and proportions of microbial genes on surfaces and airborne samples in railway vehicles. We monitored commuter vehicles using this analysis technology and confirmed that it was possible to grasp the difference in microbiome for each type of equipment. The result of the microbial diversity on each type of equipment showed that floors have different microbiomes, and that equipment touched directly by passengers, such as handrails and straps, have similar microbiomes. The result of estimation analysis of origin of microorganisms indicates that the proportion of human-derived microbiomes tends to be high on handrails and straps.

1. Introduction

Railways are a form of public transport used by an unspecified number of people. Consequently, maintaining and improving railway environmental hygiene is important for ensuring the safety and security of passengers and workers, as well as their comfort. Factors related to environmental hygiene including comfort in railway vehicles and stations include temperature and humidity, vibration, illuminance, chemical substances (odor components, etc.), microorganisms, etc. Among these factors, regarding temperature and humidity, vibration, and chemistry, measurement and evaluation technologies for "visualizing" these aspects in railways have already been developed [1], contributing to the improvement of environmental hygiene. On the other hand, there is little knowledge about microorganisms in the railway environment.

In recent years in particular, the spread of the SARS-CoV-2 virus since the end of 2019 has radically changed lifestyles in society as a whole, and awareness of environmental hygiene including infection prevention has increased. As a result, the environmental hygiene of public transportation has also come to be questioned. Railway companies are therefore increasingly being expected to play a certain role in dealing with environmental hygiene issues such as infectious diseases. Furthermore, as the context in which railways operate continues to evolve, changes in environmental hygiene due to an increase in inbound tourists and global warming are expected. In addition, assuming a labor shortage due to the declining birthrate and aging population in Japan, it is essential to improve the efficiency of maintenance to maintain environmental hygiene.

The purpose of this research was to "visualize" microorganisms by obtaining detailed information on microorganisms in the railway environment, in response to future changes in environmental hygiene, and to introduce efficient and effective cleaning and disinfection measures and antibacterial/antiviral materials, etc.

In recent years, gene sequencing analysis techniques have progressed and made it possible to perform evaluations easily and inexpensively to "visualize" microorganisms. Examining and formulating measures to improve the environmental hygiene of railways based on better understanding of microorganisms can lead to the introduction of effective and efficient measures, and reassure railway passengers and workers in the medium to long term.

In order to "visualize" microorganisms, in this report, we planned procedures for monitoring railway environmental hygiene by introducing microbiome [2] analysis and conducted basic monitoring in commercial vehicles.

2. Microbial detection technology for environmental hygiene monitoring

Environmental hygiene measures against microorganisms in the railways mainly involve cleaning and disinfection using chemicals and using materials such as antibacterial materials and ventilation. A prerequisite for introducing these countermeasures is prior understanding of the existing hygiene environment, such as types, characteristics and distribution, seasonal and temporal changes, etc. of microorganisms in the spaces and surface of equipment of vehicles and stations being targeted. Furthermore, it is desirable to be able to investigate changes in the state of microorganisms before and after implementation of these measures, to evaluate their effect. "Environmental hygiene monitoring" described here aims to obtain the information about microorganisms in the railway environment which is necessary for maintaining and/or improving environmental hygiene.

For example, cleaning and disinfection, which is one of the measures against infectious diseases, is carried out for the purpose of inactivating or reducing pathogens in the environment. In order to do this efficiently and accurately, for example, in the case of railway vehicles, it is effective to narrow down the points to be focused on by visualizing the microorganisms on each type of equipment and taking into account the distribution of microorganisms. Then, in order to examine the effectiveness of these countermeasures, it is necessary to capture the quantitative changes in microorganisms before and after implementation of the countermeasures.

For this reason, we are conducting research toward environmental hygiene monitoring of railways by combining qualitative and quantitative detection technologies based on microbial genes (Fig. 1). In this paper, we report the application and results of qualitative analysis (microbiome analysis) for railway vehicles.
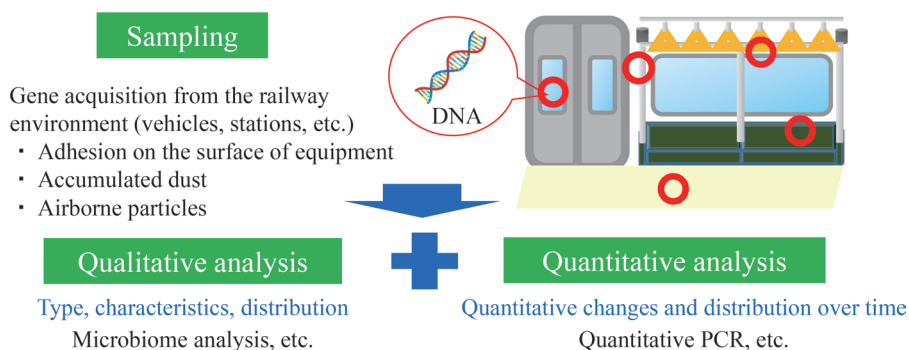
Fig. 1　Visualization of microorganisms in the railway environment

3. Examination of microbiome analysis procedure in railway environment

The procedure for microbiome analysis can be summarized in the following four steps: sampling from the railway environment (show in Section 3.1 below), DNA extraction from the collected samples (Section 3.2), gene sequencing, and analysis based on the obtained gene sequence (Section 3.3).

3.1　Sampling

Sampling is the most important step for environmental hygiene monitoring. Since timing of sampling in commercial vehicles is limited to intervals between maintenance at the depot, it is necessary to collect sufficient samples for analysis within a limited time. Therefore, sampling methods were organized to enable a team to collect sufficient sampling for microbiome analysis from each type of equipment shown in Table 1 in about 30 minutes to 1 hour. Three

Table 1　Sampling points during commuting vehicle surveys

No. in text	Method	Sampling point
(1)	Swab	Drivers' cab, windows, straps, handrails, floors
(2)	Vacuum	Dust on the seats
(3)	Direct collection	Dust collected through the air-conditioning filter

methods for collecting samples were used depending on the sample properties: (1) swabbing for deposits on the surface of equipment (4N6FLOQSwabs) in a dry state, (2) collection by a vacuum cleaner for dust accumulated on seat surfaces, and (3) collection by scraping with sterilized tweezers for dust collected in air-conditioning filters (Fig. 2). Although it is more efficient to wipe samples off with a swab dampened with physiological saline solution, time before trains were returned into service was too limited for wiping off of equipment and drying, not to mention the effect on equipment materials. Therefore, we decided to use dry swabs to secure a large sampling area. For sampling with a vacuum cleaner, in order to facilitate sample collection after sampling, a 50 ml sterile tube with a cut bottom was connected to a vacuum cleaner dust bag and attached to the suction port, and dust was collected through the tube. For commuter vehicles, the sampling area included equipment such as handrails, straps, and seats along one long seat (seating for seven people).

3.2　DNA extraction

DNA extraction was conducted using DNeasy PowerSoil Pro Kit (QIAGEN). It is known that humic and other substances contained in the soil brought in from the surrounding environment inhibit amplification by polymerase chain reaction (PCR), which amplifies gene fragments by DNA polymerase. Therefore, an extraction method including a step of removing such an inhibitor was selected.

3.3　Gene amplification and sequencing

In microbiome analysis, the types of bacteria and fungi can be identified by amplifying and analyzing a part of the rRNA gene used for phylogenetic classification of bacteria and fungi from the ex-

Wiping with a swab

Collecting dust with a vacuum cleaner

Dust collection by scraping

Fig. 2　Sampling methods

tracted DNA by PCR. In this report, in order to amplify a specific region of the 16S rRNA gene of eubacteria and archaea by PCR, the primers of 341F' [3] and 805R [4], which are DNA fragments that are the starting points for DNA replication were used. DNA fragments were amplified and purified according to the Illumina's protocol [5]. Purified samples were then sequenced using the next-generation sequencer Miseq (Illumina).

In order to identify the types of eubacteria and archaea and calculate the proportion of species for each sample, the gene sequence data obtained by Miseq was analyzed using the microbiome analysis software QIIME2-2019.07 [6, 7]. In some samples, plant-derived genes were detected, so that a step to remove these gene sequences was added to the procedure for overall analysis. In the following, eubacteria and archaea are collectively referred to as "microorganisms."

4. Trials of monitoring on commuter vehicles

4.1 Method

4.1.1 Vehicle conditions

Two types of commuter vehicle were examined (hereinafter referred to as vehicle types A and B) that travel on the same route, had the same operating mode, and differed in terms of certain types of equipment. Regarding the handrail, type A was plain and type B was pear-skin finished. In type B, antibacterial material was applied to straps and had air purifiers.

4.1.2 Sample processing

Sampling was carried out in October 2018 and October 2019. The collection was carried out in a state where the commuter vehicle after commercial operation was detained in the depot before cleaning. The procedure for analyzing the collected sample is presented in Chapter 3.

4.1.3 Vehicle conditions

The diversity of microorganisms was analyzed using the amplicon sequence variant (ASV) in which the sequence containing the error that occurred in the analysis process was removed from the obtained base sequence. For α-diversity, which indicates diversity within the sample, the Shannon index [8], which is an index of richness and evenness of species (here refers to ASVs), was calculated. For β-diversity, which indicates diversity between samples, the principal coordinate analysis (PCoA) was performed by the use of the weighted unique fraction metric (UniFrac) distance calculated using the phylogenetic distance of microorganisms and the proportion of the species. Statistical tests were performed by the Kruskal-Wallis test for the Shannon index and the PERMANOVA for the weighted UniFrac distance. If the adjusted p-value (q-value) by the Benjamini-Hochberg false discovery rate (FDR) was less than 0.05, it was considered to be statistically significant.

4.1.4 Diversity analysis

The identification of microbial species was performed from the obtained ASV using the database Greengenes [9].

4.1.5 Estimating the source of microorganisms

Since it is difficult to investigate the source of the hundreds of detected types of microorganisms from previous literature, the breakdown of the origin in the railway environment sample was estimated by referring to the microbiome data detected in various environments that have already been reported. In this report, we refer to the microbiome data registered in the Earth Microbiome Project (EMP) [10, 11]. From the sample list published on the EMP homepage (representative 2000 data), human-derived samples (skin, oral cavity, nasal cavity, feces) and environmental samples (water, soil, atmosphere) were set as the sources, and SourceTracker 2 [12] was used for analysis.

4.2 Results and discussion

4.2.1 Comparison of microbial diversity among different vehicle types [13]

Regarding vehicle types A and B, we examined the differences in the entire cabin. Figure 3 shows the α-diversity (Shannon index) in the samples for vehicle types A and B. As a result, it was found that there was no difference between vehicle types A and B.

The diversity between samples (β-diversity) is shown in Fig. 4 as the weighted UniFrac distance to vehicle type A. Similar to α-diversity, there was no statistically significant difference between vehicle types. From this, it was suggested that there is no significant difference in the diversity of microorganisms between vehicle types A and B, which travel on the same route and have similar operating modes. Regarding vehicle type B, antibacterial specifications were made for the straps, but even when comparing only the straps, a significant difference in the diversity of microorganisms was not observed between vehicle types A and B. However, this evaluation of diversity is obtained by considering the types of microorganisms and their proportions, and cannot be discussed quantitatively. In the future, as knowledge that will lead to improvement of environmental hygiene, it would be necessary to compare materials with different functions such as antibacterial/antiviral functions based on not only diversity but also quantitative distribution and changes over time.
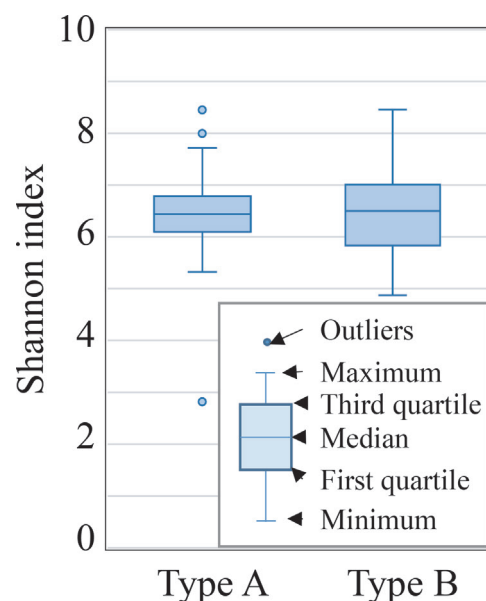
Fig. 3   α-diversity due to different vehicle types
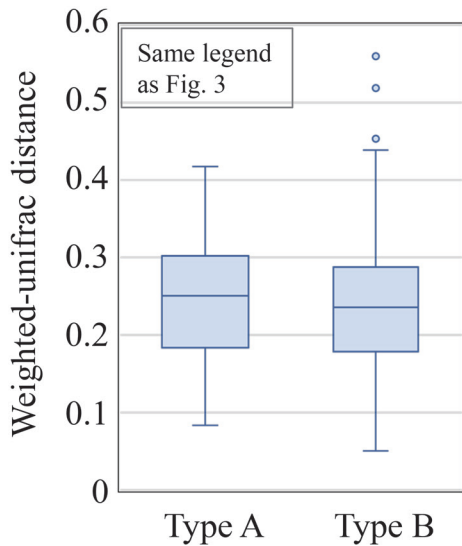
Fig. 4 β-diversity due to different vehicle types (weighted UniFrac distance to vehicle type A)

4.2.2 Comparison of microbial diversity and microbial species per type of equipment [14]

In order to examine the differences in the diversity on varying equipment, we compared the microbiomes of different types of equipment in vehicle type A and type B together. Figure 5 shows the α-diversity (Shannon index) of each facility in the cabin. The results show that the microbial diversity of the floor was highest, and it was statistically significantly different from those of the other equipment. This difference might be caused by some microorganisms brought in from the environment outside the railway such as soil. The next highest Shannon index was shown in the seat surface and dust collected by the air conditioning filter and the seat surface was significantly different from the handrails, straps, and windows, but not in the dust collected by the air conditioning filter. Since the seat surface sample and the air-conditioning dust sample included accumulated and suspended dust, respectively, it was considered that microorganisms attached to human clothes and microorganisms in the air are included. This fact leads to showing a tendency of higher Shannon index. In addition, no significant difference was found on the handrails, straps, and windows.

Following the α-diversity, Fig. 6 shows the results of the PCoA for β-diversity on each type of equipment. Taking the plot for each facility as a group, the results suggest that the microbiome corresponding to each type of equipment was distributed in the vehicle. In addition, the results showed that the plot populations overlapped greatly in the handrails, straps, and windows, which are frequently touched by passengers, and there was no statistically significant difference between them. Based on this fact, we estimate that they shared a similar microbiome. Similarities in the microbiome of equipment frequently directly touched by passengers could be due to human-derived microorganisms adhering to them. On the other hand, since floors form part of a different group of surfaces, statistically significant differences were observed when compared to other equipment, suggesting that floors have a different microbiome.

Figure 7 shows the number of microbial species for each type of equipment obtained by identifying the species with the database [9]. As a result, the total number of microbial species identified from the sample used this time was the largest at 599 species on the floor.
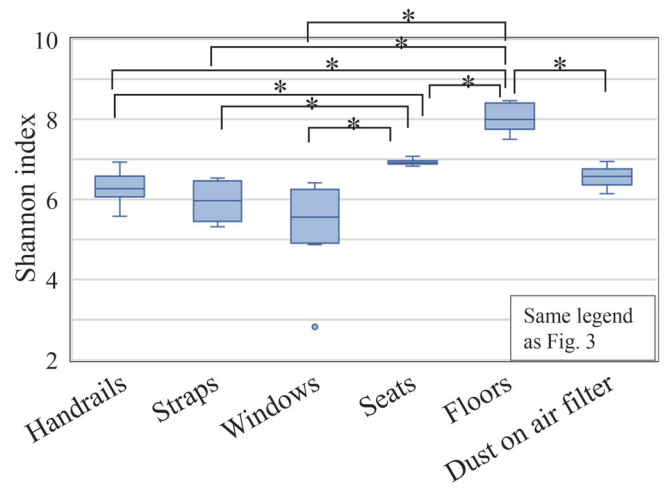
Fig. 5 α-diversity of each equipment in a cabin (* q <0.05)
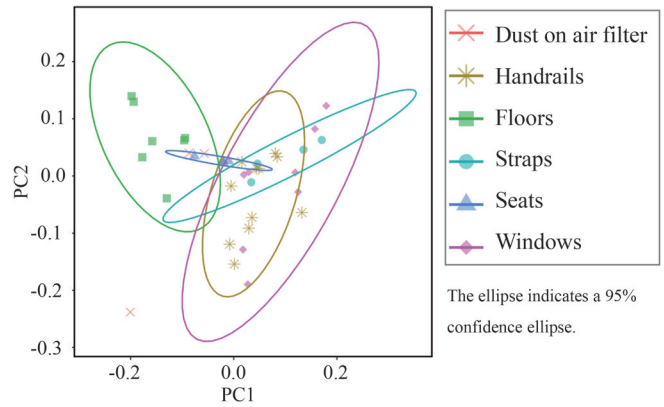
Fig. 6 PCoA of weighted UniFrac distance due to differences in equipment
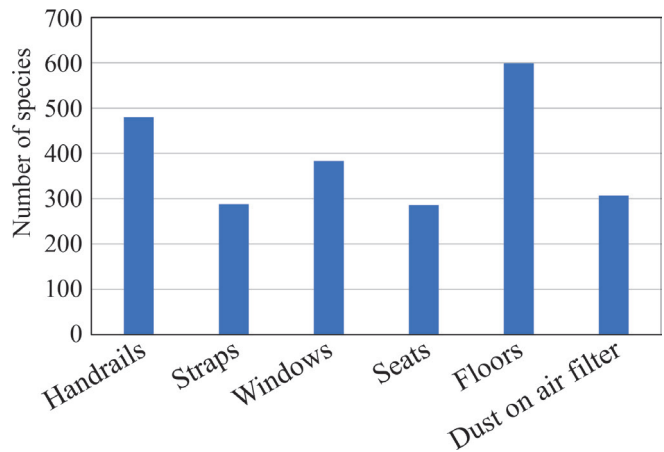
Fig. 7 Number of microbial species identified

This was followed by handrails, which had a total of 480 microbial species. From this fact, it is suggested that one of the reasons for the high α-diversity in the floor, is the large number of species.

Since we analyzed samples collected in the same season (October) in this study, we were unable to explore seasonal variations. Therefore, in the future, in order to grasp the status of changes on

the same route for each facility, it would be necessary to consider changes by collecting multiple samples for each season.

4.2.3 Estimation of the source of microorganisms

Since as indicated in Section 4.2.2, it was considered that the sources of the microbiome differed for each equipment, the source was estimated for handrails, straps and floors for the October 2018 sample (Fig. 8). As a result, the proportion of human-derived microorganisms was large on the handrails and straps. On the floor, the proportion of environment-derived microorganisms such as soil and air was higher than on handrails and straps.

Using the samples of a commuter vehicle on the same route, the features in the microbiome of equipment that people directly touch (handrails, straps and windows) were analyzed by LEfSe (Linear discriminant analysis Effect Size) [15]. We mainly extracted microorganisms belonging to the phylum Actinobacteria, including Cutibacterium acnes, a resident bacterium on human skin [16].

In future, this environmental hygiene monitoring method can be applied to provide concrete grounds for developing measures to improve the efficiency of cleaning and disinfection work and to introduce equipment with antibacterial/antiviral functions. As an example of the estimations using the analysis in this paper, we obtained an estimation result that the proportion of human-derived microorganisms is high on equipment that is directly touched by passengers. For example, these results could be used for extracting elements which should be focused on for suppressing opportunities of infection. It is assumed that an infected person releases pathogens together with the microorganisms that normally inhabit and are derived from humans. Therefore, understanding actual distribution and migration of human-derived microorganisms as an index can clarify infection routes and opportunities such as inhaling droplets containing pathogens and droplet nuclei (droplet infection, airborne infection, etc.), or touching equipment on to which droplets have adhered, which can then enter the body (contact infection).

5. Conclusions

In this report, we introduced a microbiome analysis to "visualize" microorganisms present in the railway environment. Using this analysis, we comprehensively and qualitatively grasped microbial types and compositions by detecting and analyzing genes on equipment surfaces and accumulated / floating dust samples in railway
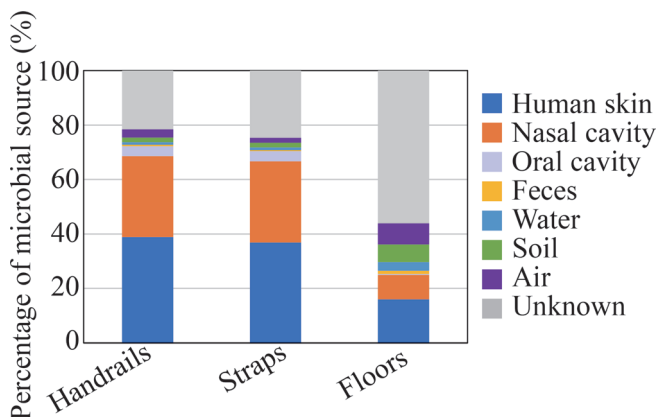
vehicles. We examined the selection and amount of sampling points that can be collected during business hours, and the conditions and procedures for detecting and analyzing microbial genes in samples.

Next, we monitored commuter vehicles using this method, and found that the number of microbial species in the samples analyzed this time was largest on floors, followed by handrails. From the viewpoint of the diversity of microorganisms on each type of equipment, the result of microbiome analysis showed that microbiomes on equipment touched directly by passengers, such as handrails and straps were similar, but differed from floors. The results for estimating the source of microorganisms on these types of equipment indicated that the proportion of human-derived microorganisms was high on handrails and straps.

In addition to these qualitative findings, it is necessary to grasp the quantitative distribution of microorganisms and their changes on the target equipment over time to "visualize" the presence of microorganism. We are also promoting the introduction of quantification technology such as digital PCR for microorganisms selected as indicators based on the results of qualitative analysis.

Progress in this work provides a response to changes in environmental hygiene conditions due to social changes surrounding the railways and environmental changes that are expected in the future, as well as emerging and re-emerging infectious diseases. We believe that it can also contribute to the construction of a railway environment that can ensure the safety and security of the railway for both passengers and workers.

References

[1] Suzuki, H. and Nakagawa, C., "Trends and Topics in Research on Passengers' Comfort," *RTRI report*, Vol. 34, No. 1, pp. 5-8, 2020 (in Japanese).

[2] Berg, G. et al.: "Microbiome definition re-visited: old concepts and new challenges," *Microbiome*, Vol. 8, No. 1, 103, 2020.

[3] Hugerth, L.W. et al.: "DegePrime, a Program for Degenerate Primer Design for Broad-taxonomic-range PCR in Microbial Ecology Studies," *Appl. Environ. Microbiol.*, Vol. 80, No. 16, pp. 5116-5123, 2014.

[4] Herlemann, D. P. et al.: "Transitions in Bacterial Communities along the 2000 km Salinity Gradient of the Baltic Sea," The *ISME J.*, Vol. 5, No. 10, pp. 1571-1579, 2011.

[5] 16S Metagenomic Sequencing Library Preparation, Preparing 16S Ribosomal RNA Gene Amplicons for the Illumina MiSeq System, http://jp.support.illumina.com/downloads/16s_metagenomic_sequencing_library_preparation.html (Reference date: July 14, 2022).

[6] Bolyen, E. et al.: "Reproducible, Interactive, Scalable and Extensible Microbiome Data Science using QIIME 2," *Nature Biotechnology*, Vol. 37, No. 8, pp. 852–857, 2019.

[7] QIIME 2, https://qiime2.org/ (Reference date: July 14, 2022).

[8] Shannon, C. E., and W. Weaver: "The Mathematical Theory of Communication," *University of Illinois Press*, 1949.

[9] DeSantis, T. Z. et al.: "Greengenes, a Chimera-Checked 16S rRNA Gene Database and Workbench Compatible with ARB," *Appl. Environ. Microbiol.*, Vol. 72, No. 7, pp. 5069-5072, 2006.

[10] Thompson, L. R. et al.: "A communal catalogue reveals Earth's multiscale microbial diversity," *Nature*, Vol. 551, pp. 457-463, 2017.

[11] Earth microbiome project, https://earthmicrobiome.org/, (Reference date: July 14, 2022).

[12] Knights, D.: "Bayesian community-wide culture-independent

Fig. 8   Estimation of source of microorganisms (October 2018 sample)

microbial source tracking," *Nat. Methods*, Vol. 8, No. 9, pp. 761-763, 2011.

[13] Yoshie, S., Kawasaki, T., Kyotani, T., Ushiogi, T. and Ikehata, M., "Microbiome analysis in commuter car," Proceeding of *2020 Annual meeting of the society of indoor environment*, Japan, p. 65-66, 2020 (in Japanese).

[14] Yoshie, S., Kawasaki, T., Kyotani, T., Ushiogi, T. and Ikehata, M., "Comparison of microbial community on each surface of facility in commuter car," Proceeding of *J-RAIL2020*, S-4-2-5, 2020 (in Japanese).

[15] Segata, N. et al.: "Metagenomic biomarker discovery and explanation," *Genome Biol.*, Vol. 12, No. 6, R60, 2011.

[16] Yoshie, S., Kawasaki, T., Kyotani, T., Ushiogi, T. and Ikehata, M., "Examination of environmental hygiene monitoring of railway vehicles by microbiome analysis -Understanding the characteristics of equipment-," The *Journal of transportation medicine*, Vol. 75, p. 45, 2021 (in Japanese).
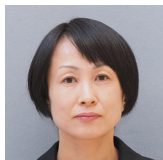
Authors

Sachiko YOSHIE, Dr. Eng.
Senior Researcher, Comfort Science and Engineering Laboratory, Human Science Division
Research Areas: Molecular Biology, Environmental Microbiology

Masateru IKEHATA, Ph. D.
Senior Chief Researcher, Head of Comfort Science and Engineering Laboratory, Human Science Division
Research Areas: Genotoxicology, Cell Biology, Microbiology

Tamami KAWASAKI, Dr. Sc.
Senior Researcher, Comfort Science and Engineering Laboratory, Human Science Division
Research Areas: Environmental Biochemistry

Takashi KYOTANI
Senior Researcher, Comfort Science and Engineering Laboratory, Human Science Division
Research Areas: Analytical Chemistry

Tomoyoshi USHIOGI
Senior Researcher, Comfort Science and Engineering Laboratory, Human Science Division
Research Areas: Chemical Engineering

Evaluation of Overall Comfort of Railways Based on Customer Experience

Fumitoshi KIKUCHI
Ergonomics Laboratory, Human Science Division

Chizuru NAKAGAWA
Human Science Division

Ayano SAITO
Ergonomics Laboratory, Human Science Division

Daisuke TATSUI
Transport Operation Systems Laboratory, Signalling and Operation Systems Technology Division

Mitsutaka ISHIZUKI
Architecture Laboratory, Structures Technology Division

Hiroaki SUZUKI
Research and Development Promotion Division

To increase overall passenger satisfaction, the comfort of railways was reconsidered from a passenger perspective. We twice conducted a web-based survey (February and November 2020) on passenger comfort during several representative travel phases (from planning to destination) and developed a draft evaluation index to estimate the overall comfort from the comfort of each travel phase. We confirm that this draft evaluation index created in the first survey shows 70 to 80% estimation accuracy against the second survey data affected by COVID-19, and that the overall comfort can be stably estimated from the comfort of each travel phase.

Key words: *evaluation of comfort, customer experience, railway passenger, COVID-19*

1. Introduction

As standards of living improve and environmental control technologies progress, there is a growing need for greater comfort and convenience in public transportation such as railways. At the same time, due to Japan's declining population, it is also important to save labor. In addition, the emergence of new variants of the coronavirus (COVID-19) has accelerated the pace of social change, making the environment surrounding railways even more challenging and spurring the need to introduce and promote digital technologies that combine labor-saving solutions and automation with a high level of service provision. In particular, comfort improvements on the railways are indispensable for providing high levels of service.

The Railway Technical Research Institute (RTRI) has been engaged in research and development related to the evaluation and improvement of comfort in three main areas.

(1) Trains (e.g., vibration, sound, heat, congestion, and seating)

(2) Stations (e.g., ease of movement, information displays, broadcasting, boarding, and alighting)

(3) General train usage environment (e.g., frequency, cost, and station access)

Most of these studies are aimed at evaluating individual comfort factors and improving comfort in a limited area. On the other hand, from the passenger's perspective (i.e., Customer experience: CX), the overall comfort of railways for passengers (hereinafter referred to as overall comfort) may be determined by the influence of the comfort of various phases of movement that are linked over time from planning and preparation for travel to arrival at a destination. Comfort during each travel phase is considered to be influenced by individual comfort factors such as trains, stations, and general train usage environment. It is necessary to clarify passenger evaluation structures that determine overall comfort to effectively improve overall comfort by controlling digitizable comfort factors.

In this study, we examined the basic relationship between the overall comfort of railways and comfort during movement phases.

2. Concept of comfort and previous studies on railways

The following section summarizes the concept of comfort in this study and previous findings from studies on railway comfort.

2.1 Concept of comfort

The concept of comfort consists of two dimensions: pleasant and neutral [1][2]. Neutral can be defined as a state in which no discomfort is felt, and pleasant as a state in which positive comfort is felt. The distinction between neutral and pleasant is not fixed, but changes as passenger expectations increase. In the past, when air-conditioned railway cars were rare, air-conditioning was a luxurious pleasant factor, but now it is a natural neutral factor. Since passenger needs for comfort tend to increase with times, it will become increasingly important to always understand their needs and provide services that exceed their expectations.

2.2 Previous research on railway comfort

The objectives of studies for comfort in railway conducted so

far by the Railway Technical Research Institute (RTRI) can be broadly classified into development of evaluation methods (indices and measures) and proposals of improvement methods, with many studies focusing on the former [2].

For train schedules, there have been studies on evaluation methods based on users' viewpoints and on estimation of train delays and congestion. An interactive ridership estimation system developed to support the generation of balanced train schedules considering congestion by quickly estimating the level of congestion at the time of schedule changes and visualizing the prediction results on diagrams

For stations, simulations of passenger flows are used to support station design, such as the location of platform stairs, width of aisles, number of ticket vending machines and ticket gates, guidance, and evacuation time calculations.

For trains, many studies have been conducted on vibration, and evaluation methods have been developed, such as ride comfort evaluation methods, motion sickness indicators, brake pattern evaluation, and car body vibration analysis methods.

As described above, quantitative comfort evaluation has become possible for specific discomfort and problematic factors such as vibration ride quality, thermal environment, noise, sound, illumination, air quality, train schedules, and passenger flow. Factors such as trains and stations that influence the overall comfort evaluation are also known to some extent. On the other hand, there are many factors that have not yet been quantitatively evaluated, such as the convenience of information, visual design, and customer service. Furthermore, the relationship between such individual improvements and overall comfort when viewed as a series of customer experience (CXs) from departure to destination is not clear.

In addition, considering recent developments in networking and control technologies, it has been pointed out that digitalization may be applied to comfort research in the near future [2]. Suzuki et al. have proposed the following four steps: (i) collect digital data on factors affecting comfort through networks (data acquisition), (ii) analyze the collected data and reproduce comfort evaluations with digital models to understand and predict the situation (analysis and prediction), (iii) formulate responses to increase comfort (decision making), and (iv) accurately control the environment (execution) [2].

3. Evaluation structure and draft evaluation index for overall railway comfort

To clarify the evaluation structure of overall comfort, we set up a representative passenger model and commuting and travel phases. We conducted a web-based survey on overall comfort, comfort during movement phases, and individual comfort factors.

3.1 Representative passenger types

Representative passenger types were set below with reference to previous studies [2] to [7] and the fact that transportation revenues are regular and non-regular revenues. Six representative passenger types were developed by combining three types of attributes (single person, family with children, and adult group), three types of travel purposes (commuting, business trip, and travel), two types of use (day trip and overnight stay), and two types of train use (conventional train, and limited express or Shinkansen) (Table 1). All passenger models assume that passengers make transfers.

3.2 Representative movement phases

Representative movement phases were set in the light of previous studies [2] to [7]. Eight representative movement phases were selected as shown in Table 2 as typical commuting and travel phases.

3.3 Overview of the web-based survey

The first web-based survey (pre-COVID-19 pandemic survey) was conducted in February 2020 on 4328 passengers (2825 males and 1503 females) living in Tokyo and three prefectures in the Kanto region where passengers were deemed to have similar travel experiences. The mean age was 46.4 years (Standard deviation: $SD = 11.2$ years). The main objective of this survey was to gather data in relation to the following two points:

(1) To understand the individual factors that influence the comfort evaluation of each movement phase.

(2) Selection of an appropriate evaluation structure model

One of major changes in social trends during the execution of this study was the arrival of the COVID-19 pandemic, which was first reported in China at the end of 2019. The environment surrounding railway has changed significantly since then due to COVID-19. Given this situation, since there was a possibility that the comfort assessment in railways may have changed because of the pandemic, a second survey (mid-pandemic survey) was conducted in November 2020. The participants of the pre-pandemic survey were recruited for the mid-pandemic survey, and the total

Table 1   Six types of representative passenger

Type No	Property	Object	Type of trip	Type of train	
				Before transfer	After transfer
T1	Alone	Commuting	Day trip	Local train	Local train
T2	Alone	Business trip	Day trip	Local train	Shinkansen
T3	Family with children	Travel	Day trip	Local train	Superior train*
T4	Adult group	Travel	Day trip	Local train	Superior train*
T5	Family with children	Travel	Overnight trip	Local train	Superior train*
T6	Adult group	Travel	Overnight trip	Local train	Superior train*

Note: *Limited express train or Shinkansen

Table 2   Eight representative movement phases

Phase No	Phase name	Content example
X1	Plan and prepare	Planning and preparing for travel, including arranging tickets, and so on.
X2	To the station ticket gate	From some person's home to the nearest station ticket gate.
X3	To the station platform	From the station ticket gate to the platform.
X4	Until getting on the train	From the station platform to get on the train.
X5	Onboard the train	Onboard the local train.
X6	Train transfer	From alighting to boarding.
X7	Onboard the train after transfer	Onboard the local train, Limited express train or shinkansen.
X8	To destination	From the alighting to destination

number of participants was 2534 (1809 males and 725 females, mean age 48.14 years (SD = 10.7 years)).

To evaluate comfort of travel experience, participants were asked to comment on their entire travel experience comprising eight movement phases, using a 7-point scale (1: very uncomfortable - 4: neither pleasant nor uncomfortable - 7: very pleasant). In addition, to understand the individual factors of each movement phase, the respondents were asked to freely describe what they felt uncomfortable about. In addition, the participants were asked to rate their experience of discomfort for a total of 132 individual factors extracted from previous studies [3] to [7] using a two-case method (0: no experience, 1: experience). The mid-COVID-19 pandemic survey included 30 additional items that were frequently experienced based on the results of free descriptions in the pre-COVID-19 pandemic survey and 8 items related to the COVID-19 pandemic (infection prevention measures, infection concerns, and so on), such as wearing masks to prevent infection and concerns about infection during transportation, based on examples of new lifestyle practices issued by the Ministry of Health, Labor and Welfare. The 8 items were newly added to the list of items (Table 3).

3.4 Results

3.4.1 Comfort evaluation of each movement phase by representative passengers

Figure 1 shows the results of the comfort evaluation for each movement phases by each representative passenger. We conducted the analysis of variance with the comfort evaluation as dependent variables, and each movement phase and representative passengers as independent variables. As a result, only the main effect of representative passengers was significant, and in each movement phase in both surveys, commuting passengers had lower comfort ratings than business trip or leisure passengers. Therefore, it was shown that

representative passengers can be reduced to commuters and business trip/leisure travelers in terms of comfort evaluation.

3.4.2 Individual factors related to comfort in each movement phase

Table 3 shows the number of items and specific examples of comfort-related individual factors organized by travel phase. These factors consist of conventional factors extracted from previous studies [3] to [7], conventional factors extracted from free descriptions based on travel experience in the pre-COVID-19 pandemic survey, and factors related to the corona disaster, and it is considered that individual factors during travel experiences of passengers were extracted comprehensively.

Table 4 shows the results of individual factors with a high percentage (20% or more) of discomfort experienced during each movement phase in the pre-COVID-19 pandemic and the mid-COVID-19 pandemic surveys. Common individual factors for all passengers were concern about train delays for movement phases during planning and preparation, and congestion for the other movement phases, suggesting that congestion at stations and in trains reduced comfort during commuting and travel.

In the mid-COVID-19 pandemic survey, wearing a mask during travel, cough etiquette of other passengers, facilities in stations and trains, and concern about infection from other passengers were commonly experienced as uncomfortable (Table 4). However, since these items were not asked in the pre-COVID-19 pandemic survey, it is highly possible that the percentage of discomfort experienced was temporarily increased by the COVID-19 pandemic. Continued research is needed to determine whether COVID-19 pandemic-related factors have a significant impact on comfort as conventional factors such as congestion.

In addition, there were individual factors that had a higher percentage of discomfort experienced by certain representative passen-

Table 3   Individual comfort factors for each movement phases, number of items and specific examples

Representative phase	X1	X2	X3	X4	X5	X6	X7	X8
	15 items	18 items	17 items	11 items	17 items	16 items	17items	21 items
Example of items extracted from previous study	Possibility of delay, fare, route search, and arranging ticket.	Other transportation, congestion, purchase ticket, and interference with movement.	Congestion, thermal environment, noise, and station facilities.	Congestion, thermal environment, noise, and station facilities.	Congestion, thermal environment, vibration, and noise.	Congestion, thermal environment, noise, and station facilities.	Congestion, thermal environment, vibration, and noise.	Congestion, thermal environment, station facilities, and other transportation.
	5 items	4 items	4 items	4 items	1 items	5 items	2 items	5 items
Example of items extracted from first investigation	Possibility of congestion and reserved seat	Manners and weather.	Manners and people flow.	Manners and waiting time.	Manners.	Manners and distance to move.	Manners and moving onboard the train.	Manners and weather.
	6 items	8 items	8 items	8 items	8 items	8 items	8 items	8 items
Example of Items related to Corona disaster	Infection control measures and fear of infection.	Infection control measures and fear of infection.	Infection control measures and fear of infection.	Infection control measures and fear of infection.	Infection control measures and fear of infection.	Infection control measures and fear of infection.	Infection control measures and fear of infection.	Infection control measures and fear of infection.

Note. X1 to X8 are the same as the representative phases of travel in Table 2.

gers. For example, the individual factors that caused more than 20% of passengers with children to experience discomfort were reduced mobility due to luggage, the small number of places for baby strollers, and crowded elevators (Table 4). It is suggested that the individual factors that reduce comfort during each movement phase may be clarified by organizing the results by passenger attribute.

3.5 Draft Evaluation Index on overall comfort in railway [8]

We examined the statistical goodness of fit of eight representative movement phases and comfort ratings of the overall travel experience, assuming several statistical models such as multiple regression model (Fig. 2) and structural equation model. As a result, the goodness-of-fit index of the multiple regression model was the

best. Therefore, a multiple regression model was adopted as the statistical model for the draft evaluation index.

A multiple regression analysis using a stepwise method was conducted with the comfort of travel experiences as the objective variable and the comfort of movement phases (X1 to X8) as the explanatory variable for each passenger for the purpose of commuting and business trip/travel (Fig. 2 and Table 5). The results showed that all standard partial regression coefficients for each movement phase were significant. The coefficient of determination R^2 ranged from 0.70 to 0.71, indicating that the comfort of each movement phase can explain about 70% of the overall comfort of the movement experience. The standardized partial regression coefficients for each movement phase were all positive, indicating that the evaluation of each phase leads to the evaluation of the movement experience. The
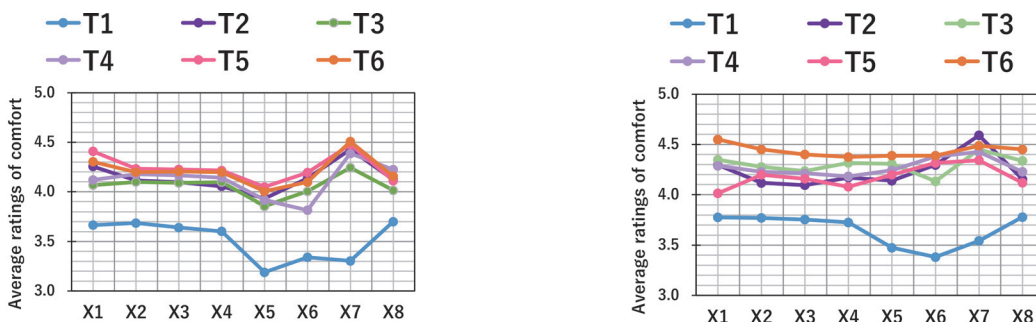
(a) Result of pre-COVID-19 pandemic survey   (b) Result of mid-COVID-19 pandemic survey

Fig. 1   Average comfort rating for each movement phases by the representative passenger

Note. T1 to T6 are the same as the representative passenger in Table1. X1 to X8 are the same as the representative phases of travel in Table 2.

Table 4   Individual comfort factors to likely to be experienced during each travel movement phases

Content	Representative movement phazes							
	X1	X2	X3	X4	X5	X6	X7	X8
Delay	All passengers: Possibility of train delays and planning for delay.			Adult group: Possibility of train delays.				
Congestion		All passengers: Congestion.	All passengers: Congestion. Family with children: Congestion of elevator.	All passengers: Congestion. Adult group: Congestion of toilet.	All passengers: Congestion and Standing on the train.	All passengers: Congestion. Family with children: Congestion of elevator.	All passengers: Congestion.	All passengers: Congestion.
Difficulty in moving		Travel passengers: reduced mobility because of luggage.	Travel passengers: reduced mobility because of luggage and narrow ticket gates.	All passengers: reduced mobility because of luggage. Family with children: Platform steps and gaps.	Family with children: Not enough space for strollers. Travel passengers: Not enough space for luggage storage.	Travel passengers: reduced mobility because of luggage.	Family with children: Not enough space for strollers. Travel passengers: Not enough space for luggage storage.	Travel passengers: reduced mobility because of luggage.

Note. X1 to X8 are the same as the representative movement phases in Table 2. All passengers are the same as T1 to T6 in Table 1. Adult group is the same as T4 and T6 in Table1. Family with children is the same as T3 and T5 in Table 1. Travel passengers are the same as T3 to T6 in Table 1. Above shows individual comfort factors with a selection rate of 20% or more.

standardized partial regression coefficients for on the train, on the train after transfer, and to the destination had large values for comfort evaluation, suggesting that these phases have a large impact on the evaluation of comfort during the journey experience. However, due to the characteristics of multiple regression analysis, the value of the standardized partial regression coefficient tends to be larger when the variation of explanatory variables is large or when the range of possible values is large. In the present data, the variation of comfort evaluation and the range of possible evaluation values are wider in the phases where the standardized partial regression coefficients were large, and it should be noted that the influence on the comfort evaluation of travel experiences may have been relatively large.

To verify the estimation accuracy of the draft evaluation indices (a) and (b) for commuting and business trip/travel shown in Table 5, we calculated the correlation coefficient and coefficient of determination between the predicted and measured values obtained by substituting the comfort ratings in the mid-corona disaster study into this multiple regression equation (Fig. 3). The results showed that commuting was predicted with $R = 0.85$ and $R^2 = 0.72$, while business trip and travel were predicted with $R = 0.88$ and $R^2 = 0.78$, indicating that they could be predicted with an accuracy of approximately 70 to 80%. Therefore, the multiple regression model adopted as a draft evaluation indicator was shown to be appropriate not only from the goodness of fit of the data to the statistical model, but also from the high prediction accuracy. However, this draft evaluation indicator is based on the representative passengers set in Table 1, and if the travel experience differs significantly from these representative passengers, a separate study will be required. In addition, since the impact of the corona disaster is accumulating since this

survey, it is necessary to continue to examine the impact of the COVID-19 pandemic on this draft evaluation indicator. In the draft evaluation index, the passenger travel experience was classified into eight movement phases, and a multiple regression model was employed in which these movement phases explain the comfort of the overall travel experience. The results of this study indicate that the overall comfort of the passenger's travel experience can be estimated with a certain degree of accuracy from the discrete but longitudinal comfort of the travel phases. Therefore, in the future, it is desirable to obtain comfort evaluation data continuously throughout passenger journey experiences and to reconstruct it as an index for evaluating overall comfort, rather than using a discrete framework of movement phases.

4. Conclusions

We reframed the concept of comfort in railways from the viewpoint of passenger travel experiences and examined the evaluation structure of passenger overall satisfaction in using railways. Six representative passenger groups were selected by attribute and purpose of use, comfort factors predicted from previous findings were identified, and a web-based survey was conducted in February 2020 before the spread of COVID-19, to gather data about the comfort of passenger journey experiences (from planning to arrival at destination). A draft set of evaluation indices was developed to explain overall comfort based on comfort in each phase of travel. As a result of the second survey conducted in November 2020, during the COVID-19 pandemic, we confirmed that the draft evaluation indices created in the first survey showed an estimation accuracy of

Fig. 2   The conceptual image on evaluation structure model (multiple regression model) of overall travel comfort and comfort each travel phases

Note. X1 to X8 are the same as the representative phases of travel in Table 2.

Table 5   Draft evaluation index on overall comfort by commuting and business trip or trave

Commuting multiple regression equation $Y= -0.01+0.10X1+0.06X2+0.12X3+0.07X4+0.28X5+0.12X6+0.14X7+0.19X8$	… (a)
Business trip or travel multiple regression equation $Y= 0.01+.014X1+0.07X2+0.11X3+0.03X4+0.19X5+0.09X6+0.19X7+0.26X8$	… (b)

Note. X1 to X8 are the same as the representative movement phases in Table 2.
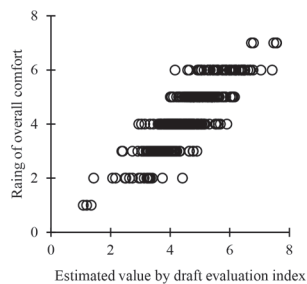
(a) Commuter travel
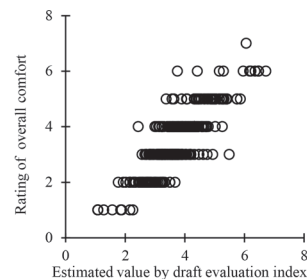
(b) Bussiness trip or leisure travel

Fig. 3   Relationship estimated overall comfort values calculate from draft evaluation index on pre-COVID-19 pandemic survey between measured values on during mid-pandemic survey

70-80% in the same survey, and that the overall comfort level could be estimated stably from the comfort level of each travel phase.

Taking measures targeting comfort factors which weigh more heavily in overall comfort can help improve passenger satisfaction in railway travel more effectively and efficiently. It will be important in future to construct a physiological-psychological human model and to conduct digitalized research on physical environment controls based on human characteristics.

References

[1] Suzuki, H., "Comfort and digitalization," *Ascent*, No. 6, pp. 5-8, 2019.

[2] Suzuki, H., Nakagawa, C., "Trends and Topics in Research on Passenger's Comfort," *RTRI Report*, Vol. 34, No. 1, pp. 5-7, 2020 (in Japanese).

[3] Murakoshi, A., Kunimatsu, T., Saito, A., "Predicting Customer Satisfaction with Train Schedules," *RTRI Report*, Vol. 22, No. 7, pp. 49-54, 2008 (in Japanese).

[4] Miyachi, Y., Saito, A., Suzuki, H., Fukazawa, N., Iino, N., "Analysis of the Factor Structure of Customer Satisfaction in Railway Service," *RTRI* Report, Vol. 17, No. 1, pp. 29-34, 2003 (in Japanese).

[5] Shinomiya, A., "Analysis of Passengers' Evaluation of Amenities Offered in Coach," *RTRI Report*, Vol. 4, No. 3, pp. 18-24, 1990 (in Japanese).

[6] Ohno, H., Suzuki, H., Shiroto, H., "Exploratory Study on Significance of Personal Services on Passenger's Comfort and Satisfaction," *RTRI Report*, Vol. 19, No. 1, pp. 11-14, 2005 (in Japanese).

[7] Suzuki, H., Shiroto, H., Omino, K., Tanaka, A., "Comfort Evaluation Index in the Passenger Room of Train," *RTRI Report*, Vol. 12, No. 6, pp. 31-36, 1998 (in Japanese).

[8] Nakagawa, C., Kikuchi, F., Saito, A., Tatsui, D., Ishizuki, M., Suzuki, H., "Evaluation of Overall Comfort in Railways Based on Customer Experience," *RTRI Report*, Vol. 36, No. 1, pp. 17-22, 2022 (in Japanese).

Authors

Fumitoshi KIKUCHI, Ph. D.
Senior Researcher, Ergonomics Laboratory, Human Science Division
Research Areas: Social Psychology, and Emotional Psychology

Chizuru NAKAGAWA, Dr. Eng.
Senior Chief Researcher, Human Science Division
Research Areas: Ergonomics, Physiological and Psychological Engineering

Ayano SAITO, Ph. D.
Senior Chief Researcher, Head of Ergonomics Laboratory, Human Science Division
Research Areas: Usability

Daisuke TATSUI
Assistant Senior Researcher, Transport Operation Systems Laboratory, Signalling and Operation Systems Technology Division
Research Areas: Transport Planning, and Passenger Flow Analysis

Mitsutaka ISHIZUKI
Assistant Senior Researcher, Architecture Laboratory, Structures Technology Division
Research Areas: Architectural Planning, and Human Behavior

Hiroaki SUZUKI, Ph. D.
Principal Researcher, Research and Development Promotion Division
Research Areas: Ergonomics, and Experimental Psychology

Summaries of Papers in RTRI REPORT (in Japanese)

Trend on Research and Development Activities Related to Railway Signalling and Telecommunication Systems

Hideki ARAI, Mitsuyoshi FUKUDA

Railway Technical Research Institute (RTRI) partially revised its organization to aim at railway system innovation with digital technology on April 1, 2022. In order to accelerate R&D for a digital railway innovation, two divisions, Signalling and Operation Systems Technology Div. and Information and Communication Technology Div. were newly established. This paper introduces the trend on R&D activities related to signalling and telecommunication systems.

Configuration and Safety Confirmation Method of Image Processing System Applicable to Signalling Devices

Akihiro GION, Takeshi ICHIKAWA, Hiroki MUKOJIMA, Nozomi NAGAMINE, Mitsuyoshi FUKUDA, Tomonori ITAGAKI

In recent years, image processing has been applied to the visual inspection of rolling stock and railroad tracks. It is also expected to be applied to abnormality detection applications at level crossings and platforms, however safety assurance is an issue for signal security applications. In this paper, we report on a method for composing an image processing system using general-purpose processing equipment that can be applied to signal security equipment and a safety confirmation method.

Circuit Scale Minimization Method for Automatic Wiring Diagram Creation of Relay Interlocking Devices

Satoshi SEKINE

In automatic generation of wiring diagrams for relay interlocking devices, we have developed a method for minimizing circuit size and a method for minimizing circuit modifications during station modifications. To minimize the circuit size, the equivalent circuit of Boolean algebra is applied to reduce the number of contacts. Then, the wiring diagrams are structured hierarchically so that the equivalent circuit can be applied at each level to deal with complex circuits. Regarding the minimization of circuit changes, we created a circuit in which the contacts before and after the construction were mixed by associating the circuits before and after the construction. Using the created circuit, we made it possible to minimize the changes by the newly devised equivalent circuit before and after the construction.

Configuration Method of Relay Input-Output System for a Safety-related Application Using General Purpose Devices

Akihiro GION, Mitsuyoshi FUKUDA, Yukihiro NAKAZAWA

In recent years, inexpensive single-board computers with input/output functions and arithmetic functions, such as Raspberry Pi, have been used for various purposes. Condition monitoring and remote control can be mentioned as one of its uses. However, it is very important to ensure safety when applying single-board computers, for example, to safety related equipment. This paper introduces a safety assurance method using pseudo-random numbers and encryption technology to configure a relay-based input/output system with a general-purpose device.

Verification of the Applicability of Fifth Generation Mobile Communication Systems to Railway Operations

Kazuki NAKAMURA, Takayasu KITANO, Kunihiro KAWASAKI, Taishi OOMI, Kenzaburo FUJISHIMA, Shun ICHIKAWA

The 5th generation mobile communication system(5G), serviced by mobile network operators(MNO), is expected to dramatically improve the three characteristics of "enhanced Mobile Broadband(eMBB)," "Ultra-Reliable and Low Latency Communications(URLLC)," and "massive Machine Type Communication(mMTC)," compared to conventional mobile communication systems. The introduction of 5G services in railways is expected to lead to the introduction of new applications that could not be realized with conventional ground-to-train communication systems. Therefore, this paper reports the outlines of our ongoing research on the introduction of public 5G services provided by MNOs to railway operations and the results obtained so far.

Estimation Method of Switching Load of Turnout for Point Machine Monitoring System

Shunsuke SHIOMI, Ken TAKASAKI, Naoyuki OKO, Kentaro TSUBAKI

A monitoring system of state of point machine is to estimate switching load of a turnout using motor current and voltage to prevent a switch malfunction of a turnout. In conventional estimation methods, the relationship between load estimation results and measured values of motor voltage and current has been pre-defined. Therefore, if installation conditions of point machine differ from those at the time of design, there will be an error in the estimated value. In order to reduce this error, we have developed a method to precisely estimate the switching load using the same measurement items as conventional methods. We also proposed a method to estimate a switching load even under severe conditions, such as when a clutch slips before a malfunction.

Lifetime Estimation of Signalling Electronic Equipment Based on Sensing Information of Usage Environment

Hiroyuki FUJITA, Kentaro TSUBAKI, Ken TAKASAKI, Naoyuki OKO

In recent years, technological development to shift from conventional time-based maintenance (TBM) to condition-based maintenance (CBM) has been progressing. In response to this trend, various efforts are being made for signaling equipment along railway tracks. However, there are issues to be solved when applying CBM to signaling electronic equipment of which indications of deterioration is difficult to be detected. Focusing on the environment in which signaling electronic equipment is installed, this paper describes the results of examining new methods for lifetime estimation of the equipment on the basis of sensing information of the usage environment.

Development of Signal Facilities Management Support System Using Camcorder Video on Train Cab

Hiroki MUKOJIMA, Nozomi NAGAMINE

Signalling facilities in railways are continuously installed in scattered locations along lines between stations. As a result, a great deal of labor has continued to be required in maintenance work for performing individual

inspections and facility management work for verifying the location and type of installation up to the day. Then, to reduce the workload in maintenance, there is a requirement for a system that can automatically recognize and inspect facility without going to the site. Therefore, we have developed a system that supports maintenance work on signalling facility with only one camcorder installed in a train cab. The proposed system recognizes signalling facilities from video obtained by camera and estimates the location of the facility to assist the maintenance work. This paper describes an outline of the proposed system and the fundamental elemental technologies used to build it.

Development of an Integrated Analysis Platform for Cross-sectional Railway Maintenance Data

Satoko RYUO, Yusuke KAWAMURA, Akio HADA, Izumi KURITA

(Vol.36, No.8, 51-56, 2022.8)

In order to achieve more efficient and labor-saving maintenance in railway systems through cross-sectional data analyses, it is necessary to share the data collected and accumulated in each railway system. However, since the format and positional representation of the data of each system, there is a problem that it is difficult to use the cross-sectional data. Therefore, we proposed an "integrated analysis platform," which possesses a database that can centrally manage data from each system and an analysis platform that performs comprehensive analysis processing. This paper introduces the network configuration and functions of the platform, and a prototype system built based on these.

Recent Studies on Railway Aerodynamics

Sanetoshi SAITO

(Vol.36, No.9, 1-4, 2022.9)

This paper presents an outline of recent studies on railway aerodynamics conducted in the Railway Technical Research Institute. Train aerodynamic effects increase significantly with the speed of train, and they cause various issues on railways. Since these issues closely affect the safety, convenience, and comfort for train, it is important to investigate the aerodynamic characteristics. The typical studies, such as the effects of cross winds, aerodynamic devices of train vehicle and the effect of flow fields around trains in open section and tunnel, are introduced in this paper.

Countermeasures against Snow Accretion Around Shinkansen Bogies Using Running Wind

Hajime TAKAMI, Yuto ARAKI, Kohei MUROTANI, Hidenori ISHII, Yasushi KAMATA

(Vol.36, No.9, 5-10, 2022.9)

In this study, we investigated a countermeasure against snow accretion on bogies of high-speed train by utilizing high-speed air flow through inlets on sides of train. The effectiveness of this method was confirmed through model experiments and numerical analysis. The results showed that this method is expected to reduce snow accumulation onto the body panel behind the bogie by about half.

Train Nose Optimization Based on Linear Acoustic Theory for Reducing Micro-pressure Waves

Tokuzo MIYACHI, Hidehiko OKUBO, Katsuhiro KIKUCHI

(Vol.36, No.9, 11-18, 2022.9)

Shapes of train noses have been optimized for reducing the peak value of a micro-pressure wave radiating from tunnel portals of high-speed railways. In this study, the shapes of multistep noses were optimized using three transfer functions based on the linear acoustic theory (W_T), experimental results (W_E), and their average (W_M). Model experiments were undertaken to measure values of the maximum pressure gradients of compression waves generated by each train nose entering a tunnel for an offset running. For optimized train noses based on W_T or W_E, the values of the maximum pressure gradient were not sufficiently reduced, and the pressure gradient waveforms were not trapezoidal shapes. Although optimized noses based on W_M well reduced the maximum pressure gradients, the values of the maximum pressure gradient were larger than those for optimized noses based on the computational fluid dynamics.

Estimation Method of Aerodynamic Load on Equipment in Tunnel Considering the Unsteady of Pressure Variation

Sanetoshi SAITO

(Vol.36, No.9, 19-24, 2022.9)

When a train travels through a tunnel at high speed, large pressure variations are generated in the tunnel. Because they act on equipment inside tunnel as aerodynamic force, it is necessary to estimate their magnitude for the design of equipment. The pressure variations mainly occur during train passage and pressure wave propagation. The pressure variations during the train passage includes high frequency components whose length is shorter than that of equipment. In this paper, a estimation method taking account of the influence of high frequency components of the pressure variations on the aerodynamic force is proposed.

Evaluation of Railway Curve Squeal Noise Using Roller Rig and Running Tests

Takeshi SUEKI, Tsugutoshi KAWAGUCHI, Yasuhiro SHIMIZU, Toshiki KITAGAWA, Hiroyuki KANEMOTO, Masahito KUZUTA

(Vol.36, No.9, 25-31, 2022.9)

Roller rig tests were performed to investigate the characteristics of curve squeal. Running tests with an actual train were also carried out to validate the results of the rig tests. Curve squeal noises and related wheel vibrations were observed in both the roller rig and the running tests. The tonal peak frequencies due to curve squeals coincided with each other in both tests. However, the magnitude of the noises and vibrations in the rig tests was much larger than those in the running tests. The vibration characteristic of the rollers of the rig may be the reason for the disagreement of the magnitude.

Identification of Aerodynamic Pressure Fluctuation Generated from Trains

Toki UDA, Yukie OGATA

(Vol.36, No.9, 33-38, 2022.9)

It is known that pressure fluctuations including infrasound are radiated from intermediate vehicles of Shinkansen trains. Previous studies have shown that infrasound consists of the aerodynamic and structure-borne components, and the aerodynamic component is originated in high-speed airflow around vehicles. The mechanism of generating the aerodynamic component, however, has been remained unclear. In this paper, a new methodology applicable to railway field tests is proposed to evaluate low-frequency aerodynamic sound less than 100 Hz. More than 100 trains were measured and ensemble-averaged, and it was shown that low-frequency aerodynamic sound was locally distributed along each whole section between two adjacent bogies and pantograph sections.

A Method to Evaluate Aeroacoustic Bogie Noise of Shinkansen High-speed Trains by Considering Acoustic Field

Nobuhiro YAMAZAKI, Masato NAKAYAMA, Takanobu NISHIURA

(Vol.36, No.9, 39-45, 2022.9)

Using a spatial distribution of the sound pressure level (SPL) obtained by a two-dimensional microphone array in a wind tunnel test, aeroacoustic bogie noise can be quantitatively estimated at measuring points. In such

cases, it is necessary to appropriately consider noise generation and sound field with respect to various acoustic properties such as ground reflection and insertion loss of a bogie side cover. In this study, the transfer function between the integrated spatial distribution of SPL and results obtained by an omnidirectional microphone is calculated by a numerical method. The SPL of aeroacoustic bogie noise of Shinkansen trains can be estimated using this transfer function and compared with the results obtained in field tests.

Evaluation of Vibration Characteristics of Viaducts and the Ground with Relation between Those Characteristics and Distribution of Ground Vibration Using Simultaneous Multipoint Measurement

Masanori NOYORI, Hidefumi YOKOYAMA, Seiji TSUNO
(Vol.36, No.9, 47-53, 2022.9)

Elucidating the mechanism of ground vibration is an important issue. In particular, there are many unsolved issues related to ground vibrations caused by trains, including interfere from multiple waves propagating through viaducts and the ground. Therefore, using simultaneous multipoint measurement data, we evaluated the vibration characteristics of the viaducts and the ground and the relation between those structural characteristics and distribution of ground vibration. The result of the evaluations of the vibration characteristics of the viaducts and the ground showed that variation of the vibration of the viaducts and the ground depends on the locations for measurement. It showed that the phase differences of the ground near pillars and the interference fringes of the ground vibration are related.

Results of Wind Tunnel Tests on Effect of Reducing Aerodynamic Forces by Wind Fences

Yuhei NOGUCHI, Minoru SUZUKI, Tatsushi OTOBE
(Vol.36, No.9, 55-60, 2022.9)

Combining trains (commuter, double-decker and freight trains) and infrastructures (double-track viaduct, single-track bridge and single-track embankment), we systematically conducted wind tunnel tests to investigate the effect of reducing aerodynamic forces by wind fences. Model scale is 1:40, and the airflow is atmospheric boundary layer flow. The specifications of wind fence are as follows: the height from rail level is 2 m, the solidity ratio is 60%, and the distance from center of train is 3 m. In this report, we summarize the results of the aerodynamic force coefficients in the cases with wind fences installed.

Research and Development Trends Related to Vehicle Technology at RTRI

Makoto ISHIGE
(Vol.36, No.10, 1-4, 2022.10)

In the organizational reform of RTRI on April 1, 2022, Vehicle Structure Technology Division and Vehicle Control Technology Division were merged to restart as Vehicle Technology Division. The aim is to respond efficiently and promptly to the increasing sophistication and diversification of needs, such as the application of digital technology in vehicle technology, response to decarbonization, and overseas expansion including international standards. Accordingly, to attain the aim of the organization reform, the new division, Vehicle Technology Division, is working on research and development by integrating mechanical and electrical systems. This paper gives an overview of the status of recent activities related to vehicle technology at RTRI.

Development of Longitudinal Excitation Suppression Devices for Reducing Elastic Vibration of Shinkansen Car-body

Ken-ichiro AIDA, Tadao TAKIGAMI, Yuki AKIYAMA, Yasunobu MAKITA
(Vol.36, No.10, 5-11, 2022.10)

This paper proposes a method to reduce the elastic vibration of Shinkan-

sen car-body caused by the longitudinal excitation via traction devices and yaw dampers. We developed two types of vibration reduction devices, which are called "displacement-dependent rubber bushes" and "mesh springs." To examine the running stability and the car-body vibration suppression performance of the developed devices, we conducted excitation tests using a Shinkansen test vehicle in a rolling stock testing plant. As a result of the tests, we confirmed that the developed devices meet the required performance for running stability, and also having the effect of reducing the elastic vibration of car-body.

Collision Analysis of a Train Set Focusing on Fracture Mode of a Coupler

Hiroyuki SATO, Tomohiro OKINO
(Vol.36, No.10, 13-18, 2022.10)

In a collision accident of a train set, if a coupler fails, it may not be possible to maintain a constant spacing between adjacent vehicles. In such cases, a collision between ends of those adjacent vehicles may occur. Therefore, it is important to understand fracture behaviors of a coupler in order to study the crashworthiness of a train set. We conducted quasi-static compressive fracture tests to obtain deformation characteristics and fracture modes for each coupler angle. Furthermore, we used Finite Element (FE) model to study improvement of the crashworthiness of a train set without requiring major changes to a carbody structure. As a result, we confirmed that reinforcing an under support plate and adopting a coupler with energy absorbing element will contribute to prevention of fracture of a coupler and improvement of the crashworthiness of a train set.

A Method for Evaluating Performance of Wheel Slide Protection Algorithm Using a Hybrid Simulator

Daisuke HIJIKATA, Yuta KIZAKI, Shin-ichi NAKAZAWA
(Vol.36, No.10, 19-24, 2022.10)

In performance evaluation of Wheel Slide Protection (WSP) system, adjustment of control algorithm by an on-track test is the most important process. However, since it is not easy to stably reproduce low adhesion condition between wheels and rails in the on-track test, the control algorithm must be adjusted under different adhesion conditions for each run. Therefore, to solve this issue, we have developed a hybrid simulator that combines a real-time computer and pneumatic brake device. The developed simulator can specify arbitrary adhesion conditions, vehicle models, and control algorithms. This paper describes a method for evaluating the performance of the control algorithm for WSP using the hybrid simulator.

Proposal for Energy-Saving Driving Method of Freight Trains Using Constant-Speed Operation

Tomoyuki OGAWA
(Vol.36, No.10, 25-32, 2022.10)

This paper presents driving methods for energy-saving of freight trains. First, we discuss a driving strategy that conserves energy considering running resistance and motor efficiency. Secondary, we confirm energy consumption and driving maneuverability, conducting running tests on several energy-saving driving methods. We also establish an energy simulation method by reproducing running tests. Finally, we verify the proposed driving method for energy-saving conducting energy simulation. This paper proposes a driving method using a constant-speed operation, which is expected to reduce energy consumption in terms of running resistance and motor efficiency.

Performance Evaluation for Traction Motor by Collaborating of Train Run Curve Preparation System and General Simulator

Toshihide YOKOUCHI, Yuki OKAMOTO, Minoru KONDO
(Vol.36, No.10, 33-38, 2022.10)

In development of traction motors for rolling stocks, it is important to evaluate power consumption and temperature rise of traction motors during operations because they are important performance metrics. In particular, when a traction motor is to be used in an operation, it is common to evaluate power consumption and temperature rise for a line and a run curve by a running simulation in advance. This study aims to adapt SPEEDY, a train run curve preparation system with long years of experience, to running simulations, linking a general-purpose simulator that creates models of traction motors. In this report, running simulations are conducted assuming a commuter train with high-efficiency induction motors. As a result, the amount of energy consumption is reduced by up to 17% by using a high-efficiency induction motor. In addition, the temperature rise is kept within the appropriate range.

A Method for Diagnosing Mounting Condition of Vehicle Parts Using a High-speed Camera

Akihito KAZATO, Takeo SHIROTORI, Haruka TAKA-HASHI, Takeshi NOMOTO

In order to improve the efficiency of railway vehicle maintenance in the future, we have developed a method for diagnosing mounting condition of vehicle parts using a high-speed camera. A system using the developed method consists of a video recording device, a program to extract acceleration of a target part from moving image, and a vibration analysis / diagnosis program. To confirm its validity of the proposed system, several tests to shoot videos of a running vehicle were conducted to understand vibration characteristics of parts mounted under floor of vehicle in the fixed and loosened conditions. The test result showed that the system, which uses a statistical method for condition diagnosis, can diagnose the condition of vehicle parts.

ANNUAL CONTENTS

QR of RTRI

November 2022 Vol. 63 No. 1 - No. 4

RTRI Researcher Received the Young Scientist Award for 2022

Dr. Munemasa Tokunaga, Senior Researcher of RTRI, received the Young Scientist Award for 2022, by the Minister of Education, Culture, Sports, Science and Technology for his outstanding research "Railway bridge structures withstanding intensified earthquake motion and increased train speeds". The result of this research is expected to improve the design of railway bridges to ensure the safety of train running in earthquakes.

On May 24, 2022, Dr. Tokunaga was handed the commendation certificate by Dr. Masao Mukaidono, Chairman of RTRI.

Dr. Watanabe, President of RTRI   Dr. Tokunaga   Dr. Mukaidono, Chairman of RTRI

QUARTERLY REPORT of RTRI

RAILWAY TECHNICAL RESEARCH INSTITUTE